

2016-01-01

Modeling And Characterization Of Piezoelectric Based Multifunctional Structures

Ricardo Martinez Hernandez

University of Texas at El Paso, rmartinez38@miners.utep.edu

Follow this and additional works at: https://digitalcommons.utep.edu/open_etd



Part of the [Mechanical Engineering Commons](#)

Recommended Citation

Martinez Hernandez, Ricardo, "Modeling And Characterization Of Piezoelectric Based Multifunctional Structures" (2016). *Open Access Theses & Dissertations*. 688.

https://digitalcommons.utep.edu/open_etd/688

This is brought to you for free and open access by DigitalCommons@UTEP. It has been accepted for inclusion in Open Access Theses & Dissertations by an authorized administrator of DigitalCommons@UTEP. For more information, please contact lweber@utep.edu.

MODELING AND CHARACTERIZATION OF PIEZOELECTRIC BASED MULTIFUNCTIONAL STRUCTURES

RICARDO MARTINEZ HERNANDEZ

Doctoral Program in Mechanical Engineering

APPROVED:

Yirong Lin, Ph.D., Chair

Norman Love, Jr., Ph.D.

David Roberson, Ph.D.

Calvin M. Stuart, Ph.D.

Charles Ambler, Ph.D.
Dean of the Graduate School

©Copyright

by

Ricardo Martinez Hernandez

2016

*Dedicated to my
family*

MODELING AND CHARACTERIZATION OF PIEZOELECTRIC
BASED MULTIFUNCTIONAL STRUCTURES

by

RICARDO MARTINEZ HERNANDEZ, M.S.

DISSERTATION

Presented to the Faculty of the Graduate School of

The University of Texas at El Paso

in Partial Fulfillment

of the Requirements

for the Degree of

DOCTOR IN PHILOSOPHY

Department of Mechanical Engineering

THE UNIVERSITY OF TEXAS AT EL PASO

December 2016

Acknowledgements

I would like to thank my mentor, Dr. Yirong Lin, for his guidance, financial support, confidence and life training that helped me achieved our goals during this doctoral research. He pushed me to be a better scholar, engineer, researcher and person.

I would like to thank the members of my committee, Dr. Norman Love, Dr. David Roberson, and Dr. Calvin Stewart, who agreed to evaluate my dissertation research. I am very grateful for their feedback, support, and input gave from time to time.

I want to thank my family for their support during my college career. Their understanding and support at an essential level held me and gave me the inspiration to give in all myself to this work.

I would like to thank the undoubted support of Dr. Ahsan Choudhuri and the Mechanical Engineering department: faculty, staff and students. I am very grateful that I always felt welcomed by all of them. In particular, my past and present members of my research team, who were with me and helped me directly to achieve my research goals: Mohammed Shuvo, Shariful Islam, Hasanul Karim, Diego Delfin, Luis Delfin, Rashedul, Luis Chavez, Emilio Tarango, Hoejin Kim, Shojib Hossain, Jose Hernandez, Rodrigo Enriquez and Jose Gonzalez, thank you guys.

Finally, to my best friend and partner in this journey, Virginia Jimenez M.S.

Abstract

Continuous monitoring of high pressure and high temperature in energy system applications has been a developing research area in today's energy sector. Multifunctional materials have the potential to provide real-time monitoring of structures where temperature and pressure sensing is critical to its performance and efficiency. In this study, multifunctional materials are studied by embedding piezoelectric materials with two ongoing technologies, woven fabric composites and additive manufacturing (AM). The AM technology allows the flexibility of embedding a sensor within the structure, all while not compromising the mechanical performance requirements. The "smart parts" are fabricated modifying the standard additive manufacturing process, using Electron Beam Melting and Selective Laser Melting, into a two stage fabrication in which a piezoelectric material is embedded in specific locations. Two case studies of "smart parts" are modeled, fabricated and analyzed in different conditions where the piezoelectric and pyroelectric response for pressure and temperature sensing are recorded. The design and performance of "smart parts" are compared to ideal conditions modeled in ABAQUS. The structural composition of smart parts showed a transition zone in the microstructure, indicating a change in mechanical behavior due to the "stop-and-go" process. Tensile results in cylindrical samples fabricated using "stop-and-go" process failed by brittle fracture near the interface where the second fabrication starts. However, the evaluation showed a voltage response that reached up to 6 V for the smart cylinders, and it generated 0.25 pA from the pyroelectric response on the smart tube. The smart parts demonstrate reliable methodologies that can be implemented as sensing components using the dielectric and pyroelectric response as temperature sensing mechanism, as well as piezoelectric response as pressure sensing mechanism. On the other side, the reinforcement with piezoelectric particles of woven fabric composites is achieved by a modified autoclave molding fabrication. The composites are fabricated with different weight percentages of PZT from 0% to 20%. These structures are analyzed in their mechanical integrity by three-point bend experiments which show a decrease in strength from 400 MPa to 250 MPa. The dispersion of particles verified the accumulation of epoxy in the depressions resulted from the intersection of the yarn and warp threads in these types of composites and was also confirmed by a

dispersion index. The electrical characterization shows a piezoelectric response up to 1.5 V, and current generation from cyclic heating and cooling up to 0.74 $\mu\text{C}/\text{m}^2$ nA.

Table of Contents

	Page
Acknowledgements	v
Abstract	vi
Table of Contents	viii
List of Tables	xi
List of Figures	xii
Chapter	
1 Introduction	1
1.1 Research Objectives	2
1.1.1 Summary of Document	3
2 Literature Background	5
2.1 Multifunctional Materials	5
2.2 Piezoelectric Materials	8
2.2.1 Applications of piezoelectric materials	11
2.3 Additive Manufacturing	13
2.4 Fiber Reinforced Polymer Composites	15
3 Methodology and Instrumentation	20
3.1 Dispersion Analysis	20
3.2 Three-point Bend Testing	22
3.3 Volume Fraction and Density Determination	23
3.4 SEM and Optical Analysis	24
3.5 LCR Meter	25
3.6 Temperature Sensing Evaluation	25
3.6.1 Dynamic pyroelectric response as sensing mechanism	26
3.6.2 Dielectric properties as temperature sensing mechanism	27
3.7 Pressure Sensing Evaluation	28
3.8 Nanoindentation	29
4 Smart Parts Development	31

4.1	Fabrication	31
4.1.1	Stop and go process	33
4.1.2	Piezoelectric ceramic	33
4.1.3	High temperature wiring	34
4.1.4	Initial design	35
4.1.5	Assessment of fabrication procedures	36
4.1.6	Protective Housing development	38
4.1.7	Modified design	42
4.2	Characterization of smart parts	46
4.2.1	Microstructure analysis	46
4.2.2	HIPping effects	49
4.2.3	Force-pressure characterization	50
4.2.4	Pyroelectric temperature sensing procedures	57
4.2.5	Capacitance and Impedance analysis	60
4.3	Performance Analysis	62
4.3.1	Smart cylinder and smart tube modeling	64
4.3.2	Apparent piezoelectric constant	72
4.3.3	Consideration of defects during fabrication	74
5	Plain Woven Fabric Composites with Piezoelectric Particle Enhancement	77
5.1	Fabrication	77
5.2	Mechanical Characterization	80
5.2.1	Density	80
5.2.2	Volume fraction	80
5.2.3	Dispersion analysis	80
5.2.4	Three-point bend results	83
5.3	Electrical Evaluation	85
5.3.1	Piezoelectric analysis	85
5.3.2	Charge generation by pyroelectricity	85
6	Conclusion and Future Work	87
6.1	Future work	88

Bibliography	90
Curriculum Vitae	97

List of Tables

2.1	Summary of main application of piezoelectric materials. Innovation field and main applications.	13
4.1	Comparison of materials suitable for electrode fabrication of smart parts. . .	35
4.2	EDS results for the alumina plates. Comparison before and after second fabrication.	38
4.3	Summary of the response on the PZT section following the model and experimental nominal properties. Force efficiency is the force transmitted to the PZT. Theoretical and simulation is presented.	74

List of Figures

2.1	Design of multifunctional materials [7].	6
2.2	Areas to explore of multifunctional materials [7]. The addition of functionality in a material forms the multifunctional structure composite.	6
2.3	Applications of smart parts [11],[12], [13].	7
2.4	Representation of piezoelectric variables.	9
2.5	Piezoelectric relations.	9
2.6	Polarization and stress hysteresis loops of tetragonal PZT. The upper right figure shows the microstructure before poling. The lower right figure indicates that any shift of 90°domain walls due to an applied electric field results in a change of polarization and deformation [18].	10
2.7	Piezoelectric coefficient of PZT (d_{33}) as a function of electric field and tem- perature during poling [19].	11
2.8	Working principles of additive manufacturing technology [24].	14
2.9	Woven fabric composites [34] and unidirectional composites comparison [35].	16
2.10	Applications of composites. Pipeline riser with composite reinforcement Boe- ing 787 and percentages of composites used in its structure.	18
2.11	Structural health monitoring. Placement of the sensing piezoelectrics pro- duces a shift in the impedance response depending on the damage applied to the structure [47].	19
3.1	Dispersion analysis.	21
3.2	Procedure schematic for three point bending experiment [49].	22
3.3	EDS and SEM performed in Hitachi S-4800 Scanning Electron Microscope. .	25
3.4	HP LCR Meter - Automated.	26
3.5	Pyroelectric testing furnace.	27
3.6	Compression compression testing.	28
4.1	EBM schematic of smart parts.	32
4.2	Stop-and-go process during EBM fabrication.	34

4.3	Fabricated 1st design. Schematic view of the assembly and the top view of the smart part with sensor components before being placed on the mask plate. The fabrication finished with misalignment of 435 μm	36
4.4	Parts included for embedding of sensor inside "smart part". Top images are as-bought before EBM fabrication, where bottom images include post EBM fabrication.	37
4.5	Design B of "smart Part".(a) Shows the bottom part with embedded sensor (b) Top view of finished part (c) Side view of finished part.	38
4.6	Modified mask plate using the bottom isolation cap to prevent powder contact with the "smart part".	39
4.7	Optimized design for a non-electrical conductive package of smart parts. . .	39
4.8	Fabrication procedure of smart parts. Alumina housing machining.	40
4.9	Alternative methods of packaging fabrication for smart parts using EBM. . .	41
4.10	Nanoindentation modulus of machinable and fired alumina used for fabrication of smart parts. No. of points analyzed: 8.	42
4.11	Test cylinder schematic.	43
4.12	Test tube schematic.	44
4.13	Succesful building using machinable alumina and EBM (2nd design).	44
4.14	Smart tube fabrication using machinable alumina package and modified design of sensor packaging.	45
4.15	Interface between the insert plate and the top section of the "smart part" at 20X.	46
4.16	Microstructure analysis of smart part, (a)Reconstruction of the interfacial region. The measurement in the grain size shows a mismatch from 1.36 μm to 0.45 μm from bottom to interfacial region. Measurements were done optically with pixel proportionality.	48
4.17	Ultimate strength, young's modulus and tensile strain of samples fabricated using "stop-and-go" process. Number of samples tested: 5	49
4.18	Setup for smart cylinder position in Low-Capacity 8800 Servohydraulic Fatigue Testing Instron machine.	51

4.19	Response of smart cylinder pressure testing.	51
4.20	Sensitivity of smart cylinder pressure testing response.	52
4.21	Force pressure in dynamic form. Stair response.	53
4.22	Cummulative voltage and force impulse from stair experiment.	53
4.23	Setup of compression-compression testing on a smart tube. A fixture was machined to ensure safety and transfer force to the smart tube. Voltage response obtained by connecting the electrodes to a DAQ system.	54
4.24	Compression-compression testing results. Each graph shows the force in kN (blue) and voltage in volts(red). Three different frequencies tested: 1 Hz (a), 10 Hz (b), and 15 Hz (c).	55
4.25	Piezoelectric effective on SLM fabricated smart cylinders.	56
4.26	Schematic of temperature variation experiment on smart tube.Parameter d was changed to variate the temperature across the smart tube.	57
4.27	Pyroelectric setup testing.Two thermocouples were attached to the inlet, and on the surface in the angular location of the piezoelectric ceramic. A picoam- meter was attached to the electrodes to record the generated current.	58
4.28	Temperature variation (a) occurred at the inlet of the tube. Different lengths increase the heat loss and produces a variation in temperature within the smart tube. A corresponding generated current (b) is recorded using a pi- coammeter.	58
4.29	Comparison between current generated and dT/dt on the thermocouple lo- cated on the surface of the smart tube. Three cases studied: 7.6 cm (a), 15.2 cm (b) and 30.5 cm (b).	59
4.30	Temperature comparison between the one calculated using the generated cur- rent (a), and the thermocouple located on the surface of the smart tube. . .	61
4.31	Smart cylinder dielectric constant and loss with respect to temperature after EBM fabrication.	62
4.32	Dielectric constant of lead oxides. Handbook of Physics and Chemistry. . . .	62
4.33	Smart cylinder temperature sensor using dielectric constant and loss after SLM fabrication.	63

4.34	Temperature sensing using SLM smart cylinders using the dielectric constant of the piezoelectric ceramic.	63
4.35	Schematic of cylinder modeling in ABAQUS for piezoelectric simulation response under different frequencies of sinusoidal loading. Alumina housing protects piezoelectric material (PZT-5A) and tungsten electrodes. Cylinder modeling simulation. Displacement contours. Generic across different contact conditions.	66
4.36	Displacement contours of cylinder modeling under compression in ABAQUS. Fabrication method: Electron Beam Melting. Metallic base of Ti-6Al-4V. . .	67
4.37	Stress contours of cylinder modeling under compression in ABAQUS. Fabrication method: Electron Beam Melting. Metallic base of Ti-6Al-4V.	68
4.38	Displacement contours of cylinder modeling under compression in ABAQUS. Fabrication method: Selective Beam Melting. Metallic base of Inconel. . . .	68
4.39	Stress contours of cylinder modeling under compression in ABAQUS. Fabrication method: Selective Beam Melting. Metallic base of Inconel.	69
4.40	Schematic of test modeling in ABAQUS for piezoelectric simulation response under single displacement.	70
4.41	Displacement contours of tube modeling under compression in ABAQUS. Fabrication method: Selective Laser Melting. Metallic base of Inconel.	71
4.42	Stress contours of tube modeling under compression in ABAQUS. Fabrication method: Selective Laser Melting. Metallic base of Inconel.	71
4.43	Approximation of cylinder piezoelectric constant.	72
4.44	Voltage contours of PZT during compression of the cylinder in ABAQUS. Fabrication method: Electron Beam Melting. Metallic base of Ti-6Al-4V. . .	73
4.45	Defects modeling for the study of piezoelectric variation. A: Single slab, B: Perimeter Slab, C: Array slab, D: Symmetric incline, E: Single Side incline. .	75
4.46	Effective piezoelectric from simulation and experiments.	76
5.1	Vacuum bag fabrication composites.	79
5.2	Modified autoclave fabrication of composites and cutting design.	79

5.3	Density (left) of woven fabric composites reinforced with piezoelectric particles. Fiber volume fraction calculation using density measurements (right). Results show the average of three samples randomly selected.	81
5.4	Optical images from the surfaces of woven fabric composites with PZT particle reinforcement: 5% (a), 10% (b), 15% (c) and 20% (d).	81
5.5	Binary images for index dispersion calculations and different concentrations of PZT: 5% (top-left), 10% (top-right), 15% (bottom-left) and 20% (bottom-right).	82
5.6	Three-point bend experiments and Young's Modulus stiffness.	83
5.7	Composites maximum strength (left) and strain at this point (right).	84
5.8	Three-point bend fracture toughness. Measured energy under the load-displacement curve.	84
5.9	Piezoelectrical characterization of woven carbon composites with PZT particles. Piezoelectric effective constant (left) and charge generated under heating-cooling cycling (right). Two samples of each denomination randomly selected and averaged.	86

Chapter 1

Introduction

The energy consumption has increased over the last decades with fossil fuel dependence of 66.8% by 2015. According to EIA, approximately 73% of U.S. coal-fired power plants will aged 35 years or older by the end of the decade. The overall efficiency in these power plants ranges from 32% to 42%, being a target for scientific research and engineering development to increase the effectiveness of the components used during this energy generation. An increase in efficiency would result in economic savings and reduction in greenhouse emissions. For this reason, one of the primary fields for engineering development is high temperature and high pressure sensing devices.

Continuous monitoring of state variables, such as pressure and temperature, is necessary to guarantee safe work environments and prevent disasters. Energy industry components (e.g., pressure tubes, air fuel pre-mixers, etc.), oil and gas industry components (e.g., drill bit, downhole piping), and civil engineering constructions (e.g., smart structure) [1] can be benefited by obtaining real-time performance feedback and continuous in-situ monitoring. Accurate temperature measurement can become technically and economically expensive. Nowadays, the applications where continuous temperature measurement is needed, the demand for use in the environment, smart homes, healthcare, agriculture and traffic surveillance, among others is increasing [2].

In general, sensors can be classified as active and passive sensors. Active power sensors require an external power supply and passive sensors are battery free. Active power sensors are limited by their electronic components and their maintenance can become expensive depending on the application. Contrarily, passive sensors eliminate the need for onboard power, their elements can withstand harsh environments and higher temperatures. Piezoelectric ceramics are used as both passive and active sensor components.

Additionally, the environmental energy harvesting to power low-energy consumption systems is becoming a growing topic for the large deployment of wireless sensor networks and increase of integration and functional density of electronics. Among the existing mechanisms for energy harvesting methods include vibrations (piezoelectric, electromagnetic induction,

electrostatic method), thermoelectric materials (Seebecks effect), pyroelectrics (thermal energy variation), and photovoltaic effect (solar cells) [3]. Among these mechanisms, pyroelectricity has revealed useful in sensing applications for a long and useful source of energy. Although pyroelectrics have been displayed low efficiencies, studies have shown that pyroelectric cells can produce currents in the order of 10^{-7} A, and charges in the order of 10^{-5} °C for temperature fluctuations from 300 K to 360K [4].

For this research, multifunctional structures are fabricated by additive manufacturing technology and traditional methods for fiber reinforced polymer fabrication. During the fabrication, piezoelectric ceramics are embedded and they function as sensor devices for continuous monitoring of temperature and pressure. Functional capabilities are enhanced and aggregated in the ultimate behavior of these smart structures.

The multifunctional structures, fabricated by additive manufacturing, or "smart parts" are designed, fabricated and characterized for energy systems that will be exposed to harsh conditions. Commercially available software is used for the design and estimation of the sensor response under different conditions, as well as an understanding of the fabrication quality. The software includes ABAQUS for the structural analysis and coding algorithms of shell scripting and python to implement and optimize the parametric studies of the smart parts. Backward calculations and numerical analysis on the main properties of the smart parts are used for calibration and practical usage of the smart parts. Additionally, the enhanced composites with particulates of piezoelectric PZT, are characterized mechanically and electrically.

1.1 Research Objectives

The goal of this work is to produce multifunctional structures with sensing capabilities embedding in its structure through the use of piezoelectric ceramics. Traditionally, passive sensing devices are mounted on the surface or require complex coupling to be adapted, severely modifying the design and the original structure of the component. By combining the additive manufacturing technology and piezoelectric ceramics as sensing materials, a "smart part" will be capable of minimizing the changes of the original structure's design and adding monitoring capabilities of temperature and pressure. The additive manufacturing

technology allows strategic placement of the sensor following the areas of interest depending on the application that ultimately would help to increase the efficiency of the power plants and allowing health and fatigue monitoring of the energy system components. In contrast, the fabric composites with particulate reinforcement, have been developed for enhancing the sensing capabilities and applied for structural health monitoring. The objectives of this work are:

1. The fabrication of energy system related components with embedded sensors. The fabrication of the smart parts was done by EBM and SLM technology. The fabrication is modified in a multistep "stop-and-go" process to allow the embedding of the piezoelectric ceramic.
2. Mechanical and sensing evaluation of the components. Piezoelectric, pyroelectric and dielectric sensing is tested and reported. The sensing capabilities of the "smart parts" including pressure and temperature will be demonstrated.
3. Assess the quality and performance of the fabrication of the smart parts. FEA software is used to analyze ideal conditions and comparison with actual behavior.
4. Fabricate and design fiber reinforced polymer composites with piezoelectric particulate reinforcement.
5. Mechanical and electrical characterization of the composites structures. The piezoelectric response after poling the composite and charge generation using cyclic heat will be determined.

1.1.1 Summary of Document

This document is divided into five chapters. Chapter 1 addresses the impact and objectives for developing multifunctional structures that will allow the implementation of sensing components within inert structures used in energy system applications.

Chapter 2 includes the literature background of multifunctional materials, following the explanation of the core elements to create these: piezoelectricity and additive manufacturing.

Chapter 3 is composed of the experimental methods and procedures for testing and characterize the multifunctional materials.

Chapter 4 presents the developed of "smart parts". It includes the fabrication methods, the manufacturing designs, the sensing evaluation and the performance analysis using FEA software.

Chapter 5 presents the fabrication and characterization of the fabric woven composites with piezoelectric particulate composites. Mechanical characterization, dispersion analysis, and piezoelectrical analysis are presented.

Finally, Chapter 6 summarizes the conclusions and suggests future work for further development of smart composites.

Chapter 2

Literature Background

2.1 Multifunctional Materials

Multifunctional materials can be defined as those designed for specific requirements in the area of electronics, magnetic, optical, thermal, mechanical or other to satisfy previously unattainable performance. These materials are unique composites in which constituents combine the functionality of their constituents.

Nature provides the ultimate multifunctional materials. In reality, every biological material system provides a combination of actuation, sensing, and self-healing capabilities. [5]. Thus, the multifunctionality of a material follows the nature design from micro to macroscales.

The development of these materials has evolved in the last two decades. Although the glass and carbon composites materials are reliable and modern replacements for lightweight and strength applications, these can only achieve limited combination of properties. New engineering challenging applications and mixtures are being developed to include self-healing characteristics, electromagnetic shielding, sensing capabilities of state variables such as pressure and temperature, among others. Figure 2.1 shows the synthesis of multifunctional composites structures and the future trend to mimicking the evolved design of nature. The remarkable advancements in material science and manufacturing process have enabled the fabrication of multifunctional composites materials. The rapid increase in the number of research in this topic is a clear indication of the increasing demand for this kind of materials [6].

The method for designing these materials involve the incorporation of sensors for monitoring its situation (self-damage detection and assessment). Typically, the damage is determined by using non-destructive techniques such as radiography or ultrasonic testing that cannot provide continuous monitoring during service. The inclusion of non-structural elements such as piezoelectric materials or optical fibers allows to overcome the need for periodic assessment and convert out structures into a self-continuous monitoring system. The func-

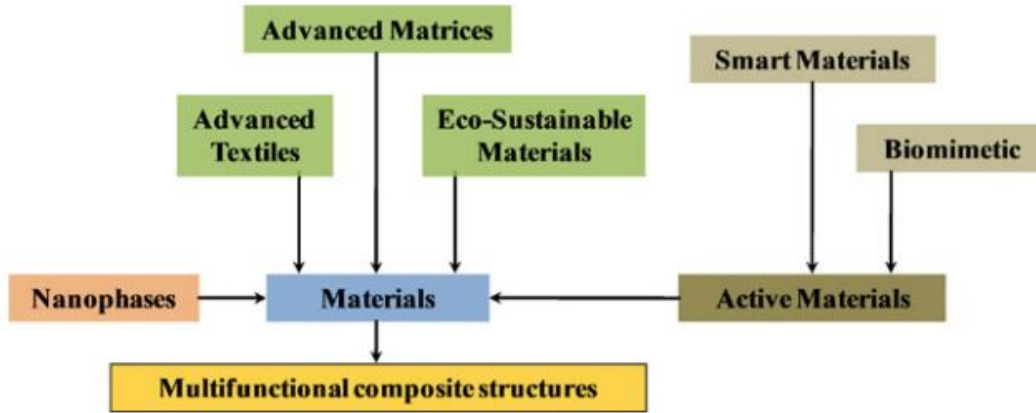


Figure 2.1: Design of multifunctional materials [7].

tionality that can be embedded within the structure is simplified in Figure 2.1. Depending

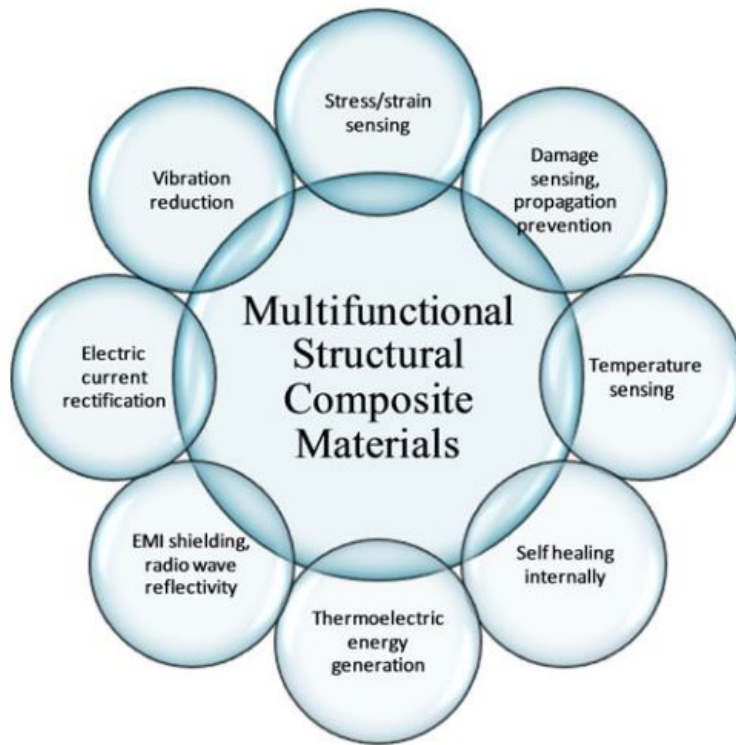


Figure 2.2: Areas to explore of multifunctional materials [7]. The addition of functionality in a material forms the multifunctional structure composite.

on the designing requirements, materials with specific functionality are combined to create

multifunctional materials. Continuous monitoring of strain is valuable for vibration control. These have been achieved in carbon fiber reinforced epoxy composites since the impedance through the thickness or in the longitudinal direction changes reversible with the deformation of fiber misalignment. Additionally, these composites have been proven to work as thermistors and thermocouples, since the interface between the lamina changes its electrical resistivity with temperature changes [8]. Alternatively, Fiber Bragg Grating (FBG) sensors have been used for internal and surface monitors of strain [9]. Besides, the FBG sensors and optical fibers provide continuous monitoring during production and over the lifetime of the structure [10]. Self-healing composites have been developed to provide emergency assessment

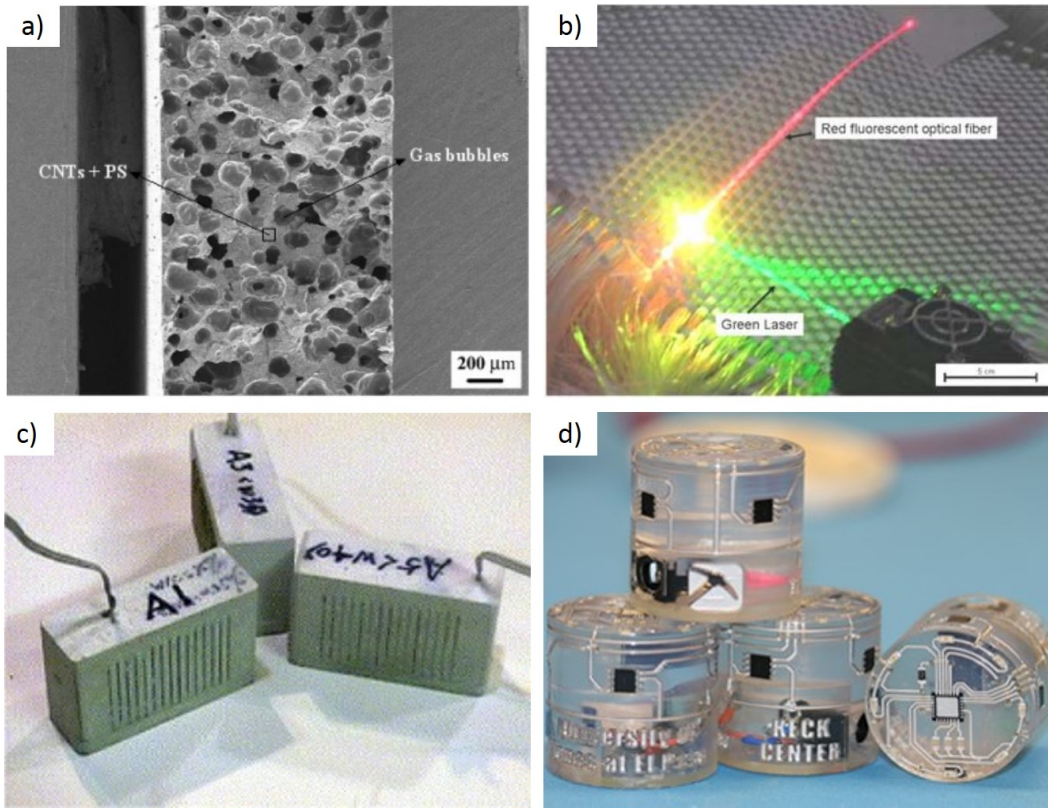


Figure 2.3: Applications of smart parts [11],[12], [13].

and temporary solutions to catastrophic failure of composites in service. These composites arrest the crack propagation and preserve the structural integrity. Two categories exist: self-healing without and with healing agents [14]. Composites without healing agents rely on the highly cross-linked polymeric material with multi-furan and multi-maleimide via Diels-

Alde reaction. When the temperature reaches a critical point, the "intermonomer" linkages disconnect, reconnecting however upon cooling. This process is reversible and can be used to restore fracture parts of polymeric structures. The use of healing agents in composites, contains a liquid encapsulated and embedded into the composites matrix. As soon as the crack destroys the capsules, the liquid fills the cracks due to the capillary effect. These techniques have been implemented in fiber reinforced polymers using micro-capsulated healing agents and a solid chemical catalyst dispersed within the matrix [15]. When the crack propagates, and microcapsules are broken, the polymerization of the healing agent is triggered by contact with the catalyst, bonding the crack phases and achieving 90% recovery of the virgin fracture toughness.

Other smart structures developments include constructing an integrated optical network embedded into carbon fiber composites. In principle, this embedding of transponders and sensor networks into structures could significantly reduce the vehicle manufacturing and design costs. Composites of carbon nanotube reinforced polystyrene foam composites have been shown to effectively shielding against electromagnetic interference. These composites have shown to be very effective and lightweight [12]. Dong and Li [13] developed cement with piezoelectric particles to create actuation within the composites.

Similarly, the piezoelectric materials are widespread used for shape control and vibration attenuation. For microelectromechanical systems (MEMS), a challenge in processing structures is to create a thin film with the desired properties and structure. [16]. This processing is achieved by physical and chemical vapor deposition and solution deposition. In the following section, piezoelectric materials principles are reviewed.

2.2 Piezoelectric Materials

Piezoelectricity is the phenomena that model the electromechanical interaction between the mechanical and electrical state in crystals without a center of symmetry. Out of the increasing number of piezoelectric materials only a restricted number have been proven suitable for transduction elements in piezoelectric sensors, these include natural and synthetic single crystals, piezoelectric ceramics, textures and thin films [17]. Regarding engineering design, ideally, a piezoelectric material must have high piezoelectric sensitivity, high mechanical

strength and rigidity, a stable and very high impedance at high temperatures, and minimal hysteresis, among others.

The physical behavior of piezoelectric ceramics involves heat, mechanical and electrical effects. The best representation of these variables is simplified in the Heckman diagram (see Figure 2.4). In this figure, electrical field (E), temperature (Φ), and stress (T) are interrelated with charge flux (D), entropy (σ), and strain (S). From the interaction among these variables the piezoelectric, pyroelectric, and thermomechanical effects are represented.

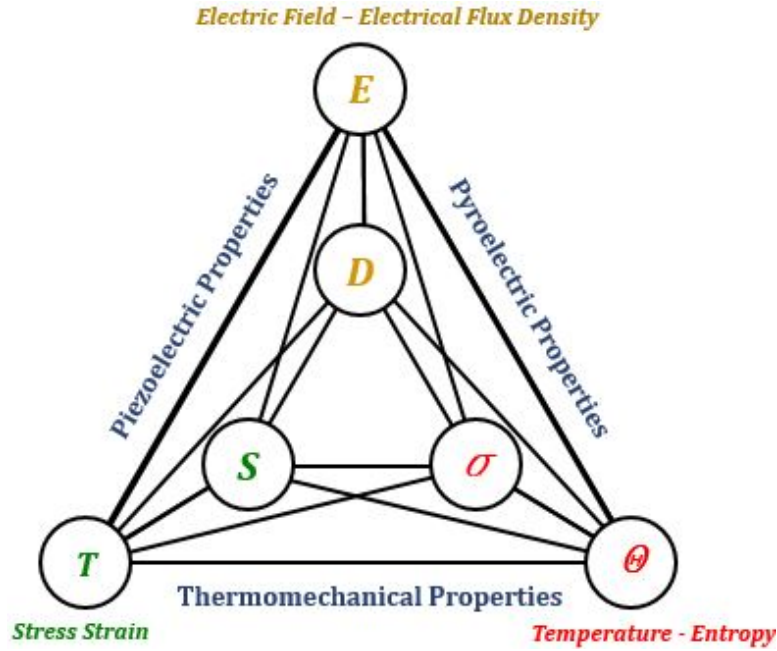


Figure 2.4: Representation of piezoelectric variables.

The matrix form of the piezoelectric constant is shown in Figure 2.5.

$$\begin{bmatrix} \Delta\sigma \\ D_i \\ S_\lambda \end{bmatrix} = \begin{bmatrix} \frac{\rho c^{E,T}}{\Theta} & p_j^T & \alpha_\mu^E \\ p_i^T & \epsilon_{ij}^{\Theta,T} & d_{i\mu}^\Theta \\ \alpha_\lambda^E & d_{j\mu}^\Theta & s_{\lambda\mu}^{\Theta,E} \end{bmatrix} \begin{bmatrix} \Delta\Theta \\ E_j \\ T_\mu \end{bmatrix}$$

p_i^T : Pyroelectric
 $\epsilon_{ij}^{\Theta,T}$: Dielectric
 $d_{i\mu}^\Theta$: Piezoelectric
 α_λ^E : Thermal expansion
 $s_{\lambda\mu}^{\Theta,E}$: Compliance

Figure 2.5: Piezoelectric relations.

The Curie temperature of a piezoelectric/piezoceramic material is the temperature at which the polarization of the material breaks down, thus losing its piezo/pyro-electric properties. In ferroelectric materials, the asymmetry in the structure that allows the piezo-electric response, usually does not exist except below its Curie temperature. However, a poly-crystalline structure can minimize the response if the ferroelectric domains are not aligned into a single direction. In most cases, a poling procedure is required to imprint the macroscopic asymmetry by proper orientation of these domains.

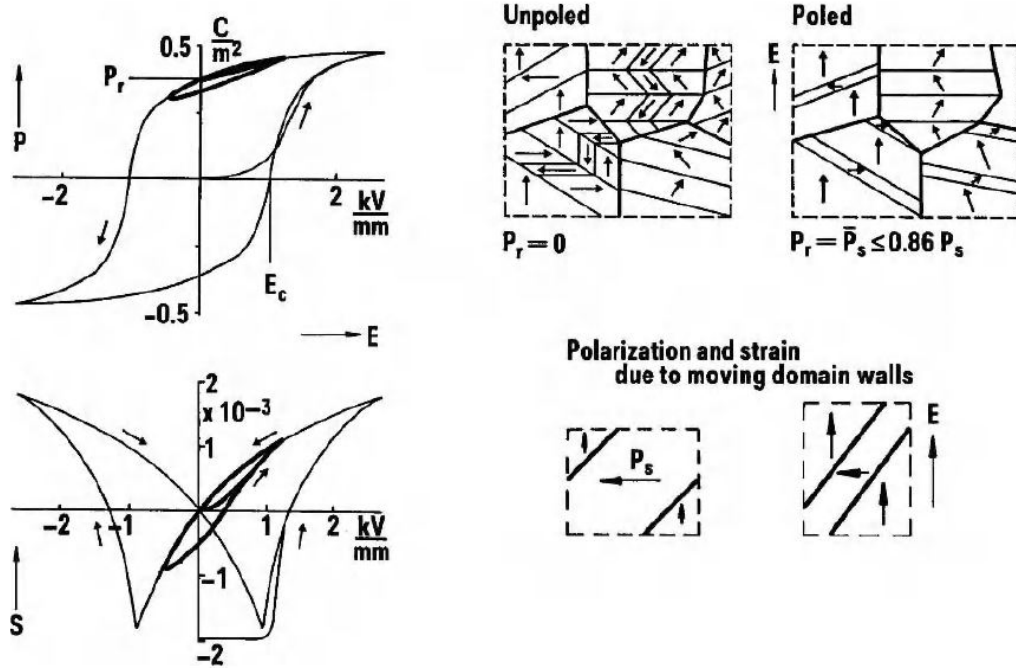


Figure 2.6: Polarization and stress hysteresis loops of tetragonal PZT. The upper right figure shows the microstructure before poling. The lower right figure indicates that any shift of 90° domain walls due to an applied electric field results in a change of polarization and deformation [18].

Ferroelectric piezoelectric response is formed from two effects:

1. The atomic displacement within the individual unit cells of the material. It will dominate as long as the domain configuration remains unaffected by the applied electrical field or mechanical stress (*intrinsic response*).
2. Results from the non-180° domain wall movements driven by the application of an

external electric field or a high enough mechanical stress (*extrinsic response*).

The response becomes increasingly nonlinear associated with a considerable hysteretic behavior .

Poling of piezoelectric PZT can be done under different circumstances of temperature and electric field. A study investigating the influence of poling temperature and electric field amplitude was done by Prewitt [19]. The study analyzes the piezoelectric constant under temperature range between 25°C and 175 °C, and electric field ranging between 0 kV/mm and 2 kV/mm. At room temperature, the piezoelectric constant can be recovered 93% at 2 kV/mm. The summary of the study is shown in Figure 2.7.

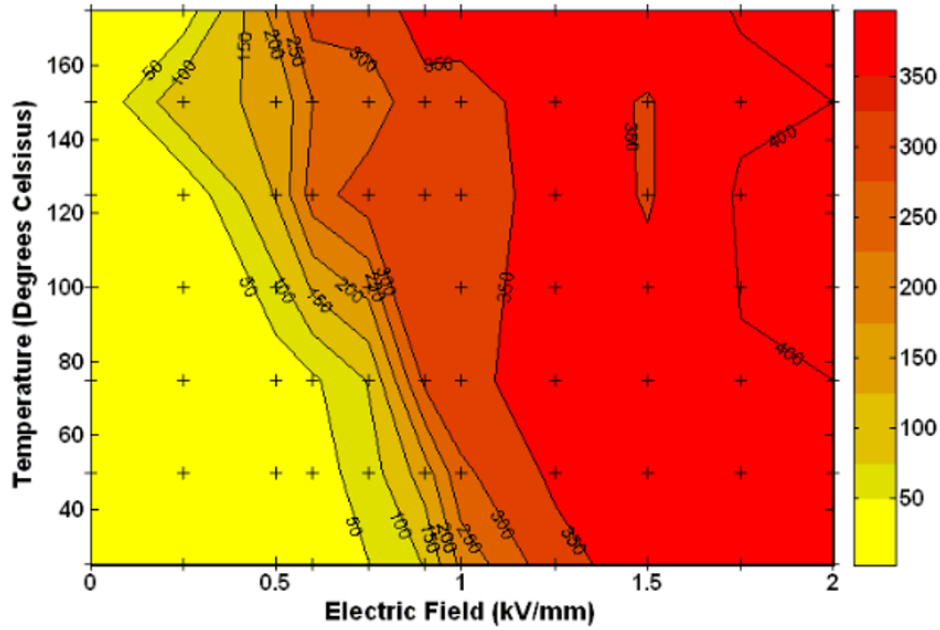


Figure 2.7: Piezoelectric coefficient of PZT (d_{33}) as a function of electric field and temperature during poling [19].

2.2.1 Applications of piezoelectric materials

Piezoelectric sensors require external energy to obtain an output signal. In these materials, the sensing and transduction element are the same. The applications of the piezoelectric

materials range and explore the different implementations and commercial application for the sensing or actuation mode.

Piezoelectric ceramics allows the development of both passive sensing and active sensing (external power from battery required). Passive sensing research is based on radio-frequency signals that are transmitted to the piezoelectric and bounce back to a reading antenna. The change in temperature or pressure within the material affects the velocity at which the wave travels from one end to the other. These devices are known surface and bulk acoustic wave devices (SAW and BAW sensors). Additionally, these devices provide accurate frequency control and signal processing.

As active sensing, the piezoelectric can be used for actuators and motors (actuation mode) or as sensors for pressure, or mass flow for automotive and medical applications. A summary of today's technology where piezoelectric materials are used is presented in Table 2.1.

Table 2.1: Summary of main application of piezoelectric materials. Innovation field and main applications.

Category	Innovation Field	Main Application
Frequency control and signal processing	Frequency-/time standards, Mechanical frequency filters, SAW and BAW devices	Precise and inexpensive frequency control and filtering. Passive signal processing for wireless communications, identification, sensing, etc.
Sound and ultrasound	Buzzer, microphones and speakers, ultrasound imaging, hydrophonics, high power transducers, shock wave generation, atomizer, and air ultrasound	Sonic alerts, alarms, telephone, blood pressure, medical diagnostics, sound detectors for sound, machining, US cleaning, oil atomizer, humidifiers, aerosols
Actuators and motors	Printers, motors and transformers and bimorph actuators	Needle drives and ink jet, miniaturized, compact motors and transformers, pneumatics, micropumps, braille for the blind
Sensors	Acceleration sensors, pressure and shock-wave sensors , flow sensors, and mass sensitive sensors	Automotive, automation, medical
Ignition Adaptronics	Ignition, Adaptive devices	Gas and fuel ignition Active noise and vibration cancellation, adaptive control, airtail filter control

2.3 Additive Manufacturing

Additive manufacturing (AM) technology, is state-of-art fabrication which consists of building components using a layer by layer process. Over the past three decades, research community has developed novel AM processes and applied them in the aerospace [20], automotive [21], biomedical [22], and other fields. The fields that AM covers includes processing, material development, software, equipment innovation and rapid tooling applications. Currently, the direct fabrication of functional end-use products has become the main trend of AM technology.

The ASTM F42 Committee [23] classifies the AM processes into seven areas. However, Guo [24] made a classification according to the starting material used: liquid, filament/paste,

powder, and solid sheet. The working principles of AM technology are summarized in Figure 2.8. The technology used in this research is powder based AM. The machines used to

State of starting material	Process	Material preparation	Layer creation technique	Phase change	Typical materials	Applications
Liquid	SLA	Liquid resin in a vat	Laser scanning/light projection	Photopoly-merization	UV curable resin, ceramic suspension	Prototypes, casting patterns, soft tooling
	MJM	Liquid polymer in jet	Ink-jet printing	Cooling & photopoly-merization	UV curable acrylic plastic, wax	Prototypes, casting patterns
	RFP	Liquid droplet in nozzle	On-demand droplet deposition	Solidification by freezing	Water	Prototypes, casting patterns
Filament/Paste	FDM	Filament melted in nozzle	Continuous extrusion and deposition	Solidification by cooling	Thermoplastics, waxes	Prototypes, casting patterns
	Robocasting	Paste in nozzle	Continuous extrusion	–	Ceramic paste	Functional parts
	FEF	Paste in nozzle	Continuous extrusion	Solidification by freezing	Ceramic paste	Functional parts
Powder	SLS	Powder in bed	Laser scanning	Partial melting	Thermoplastics, waxes, metal powder, ceramic powder	Prototypes, casting patterns, metal and ceramic preforms (to be sintered and infiltrated)
	SLM	Powder in bed	Laser scanning	Full melting	Metal	Tooling, functional parts
	EBM	Powder in bed	Electron beam scanning	Full melting	Metal	Tooling, functional parts
	LMD	Powder injection through nozzle	On-demand powder injection and melted by laser	Full melting	Metal	Tooling, metal part repair, functional parts
	3DP	Powder in bed	Drop-on-demand binder printing	–	Polymer, Metal, ceramic, other powders	Prototypes, casting shells, tooling
Solid sheet	LOM	Laser cutting	Feeding and binding of sheets with adhesives	–	Paper, plastic, metal	Prototypes, casting models

Figure 2.8: Working principles of additive manufacturing technology [24].

develop the smart parts were Selective Laser Melting (SLM) and Electron Beam Melting. The selective laser melting (SLM) completely melts the powder with a high power laser beam to form a metallic part almost entirely dense. The technique reduces the residual stresses, and these parts do not require post-processing for direct implementation. The mechanical integrity of these parts is comparable or better than those of rolled metal sheets. The SLM process is more difficult to control due to the large energy input to melt metal particles which causes problems such as balling, residual stress development, and part deformation [25].

In contrast, the electron beam melting (EBM), uses an electron beam rather than a laser beam as its energy source. The operation is under high vacuum chamber. The fabricated parts are almost fully dense, free of voids, and extremely strong. Compared to SLM, EBM has superior build rate because of its higher energy density and higher scanning speed;

however, the surface roughness is not as good as machined counterparts. The development of AM offers a great potential for customization and fabrication of very complex geometries. Applications in aerospace, automobile, biomedical and energy fields have been increasing the demand of using AM as cost-effective fabrication process.

Additionally, AM can be used to embed sensors while not compromising the parts complex geometries. Historically, AM is well appreciated in the field of biomedical, automotive, and aerospace industries due to various material options, material properties, ability to fabricate complex shape parts. Currently, energy system components mostly use surface mounted sensors which may experience high pressure and temperature and corrosive exposure that would decrease sensor lifetime and accuracy [26]. Shape alteration is not desirable in applications such as the wind turbine, where a change in wind flow may alter its aerodynamic performance. Also, the outside wall sensor may not provide desired information regarding the interior of the parts. For example, for a pressure tube, a surface sensor may not show the internal pressure created by the fluid. Hence, EBM fabricated smart part with embedded piezoelectric ceramic material at the desired location is a potential solution to alleviate this issue. Previously, different sensors including fiber grating sensors, and thermo-mechanical sensors were used in smart parts fabrication [27, 28, 29, 30, 31], though the core materials were not suitable for high temperature applications.

2.4 Fiber Reinforced Polymer Composites

In the last two decades, the use of composite materials in structural applications ranging from aircraft and space structures to automotive and biomedical as well as ballistic armor applications has been growing interest [32]. These polymer based composites are being used due to their higher stiffness and strength per unit weight in comparison with aluminum and titanium alloys.

The classification of polymer matrix composites can be divided into two main categories: particulate reinforcement or fiber reinforcement [33]. The fiber reinforcement can be short or long fiber to create single or multilayer (angle-ply) composites, and orientation may vary from random to perfectly aligned. A combination of long fiber composites and multi-directions are the crossply (plain fabric composite shown in Figure 2.4) or the

multidirectional fiber composites.

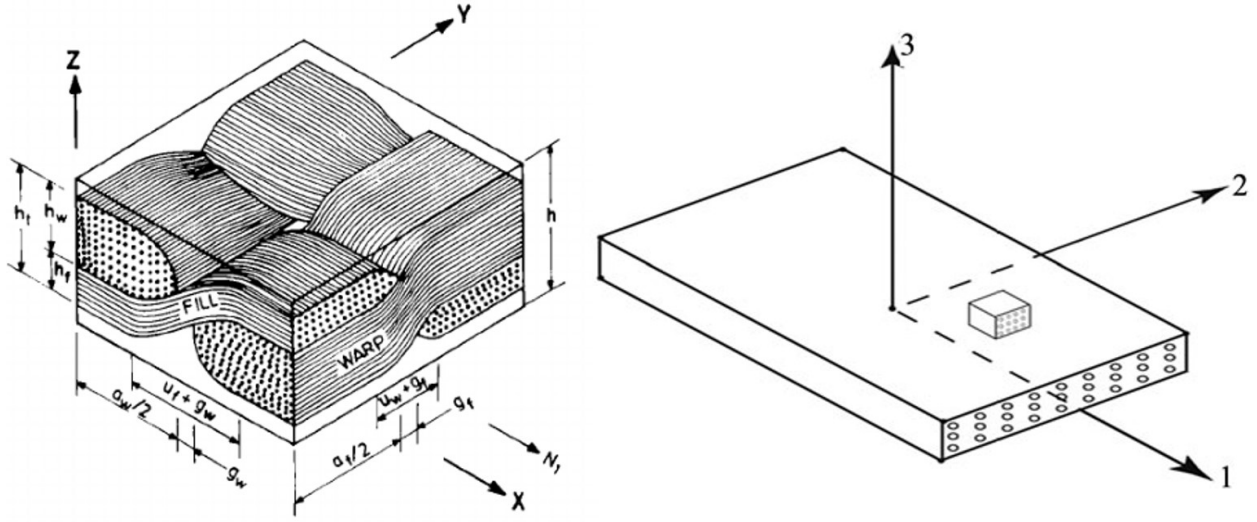


Figure 2.9: Woven fabric composites [34] and unidirectional composites comparison [35].

The characterization of polymer matrix composites involved the consideration of the anisotropy that affects the determination of properties such as stiffness, Poisson's ratio, strength, thermal expansion, moisture expansion, thermal and electrical conductivity, among others. In particular, the woven fabric and multidirectional composites, provides structural stability in both directions of the plane, and reducing the shear developed between the lamina for laminates with $[0/90]_n$ configuration.

The woven fabric composites consist of orthogonal interlaced threads, known as the warp and fill or weft threads [36]. The threading of the woven fabric composites is done by repeating a pattern in every direction. For a pattern that is interlaced every other yarn, it is called *plain* (for every third yarn it is called *twill*).

To understand the mechanics of the woven fabric composites, assumptions for the degree of anisotropy have helped researchers to simplify the equations governing properties such as stiffness, strength, and Poisson's ration [37, 38]. Orthotropic assumption, although not completely accurate, has been a very good approximation when studying plain woven fabric composites. Experimental results from carbon and glass woven fabric has shown a difference between the longitudinal and transverse direction of less than 3% [39]. Generalized model to study the effects of parameters of the fabric geometry has been done by Naik and

Shembekar [35]; and a homogenized micromechanics has been done by [40]. The theoretical basis of these studies is the classical laminated plate theory [41, 42]. The constitutive equations are given by:

$$\begin{pmatrix} N_i \\ M_i \end{pmatrix} = \begin{bmatrix} A_{ij} & B_{ij} \\ B_{ij} & D_{ij} \end{bmatrix} \begin{pmatrix} \epsilon_j^o \\ \kappa_j \end{pmatrix} \quad (2.1)$$

where

$$(A_{ij}, B_{ij}, D_{ij}) = \sum_{m=1}^4 \sum_{h_{m-1}}^{h_m} (1, z, z^2) Q_{ij} dZ \quad (2.2)$$

where A_{ij} , B_{ij} , and D_{ij} are the stiffness matrices for laminates and

$$Q_{ij} = \begin{bmatrix} \frac{E_x}{1-\nu_{yx}\nu_{xy}} & \frac{\nu_{xy}E_x}{1-\nu_{yx}\nu_{xy}} & 0 \\ \frac{\nu_{yx}E_y}{1-\nu_{yx}\nu_{xy}} & \frac{\nu_{xy}E_y}{1-\nu_{yx}\nu_{xy}} & 0 \\ 0 & 0 & G_{xy} \end{bmatrix} \quad (2.3)$$

In Eq. 2.2 the Q_{ij} is evaluated based upon the corresponding stiffness properties within the layer defined by h_m (ondulation of the fill thread) and h_{m-1} (ondulation of the warp thread). Also, N_i is membrane stress resultant, M_i is the membrane moment resultant, ϵ_j^o is the strain, and κ_j is the curvature of the laminate geometrical mid-plane.

The high strength, high stiffness, and low density characteristics make composites desirable in primary and secondary structures in many fields of industry. The Boeing 787 contains 50% of weight from composite materials. A breakdown of composites used in aerospace industry is shown in Figure 2.10. In actuality, small aircraft are fabricated with their primary structural component being composites sandwich with glass fabric/epoxy skins and PVC foam core [43]. The stealth characteristics are highly desirable for military aircraft, such that of the B-2 bomber [44].

As composites are becoming essential to our modern life, research and technology have been oriented towards the development of multifunctional matrix reinforced composites. The functionality such as transducing and sensing capabilities would allow the improvement of thermal, mechanical, optical and electrical properties within the overall structure.

The inclusion of pyroelectrics and piezoelectrics in woven fabric composites would allow low-energy harvesting in different applications such as the construction, aircraft, and

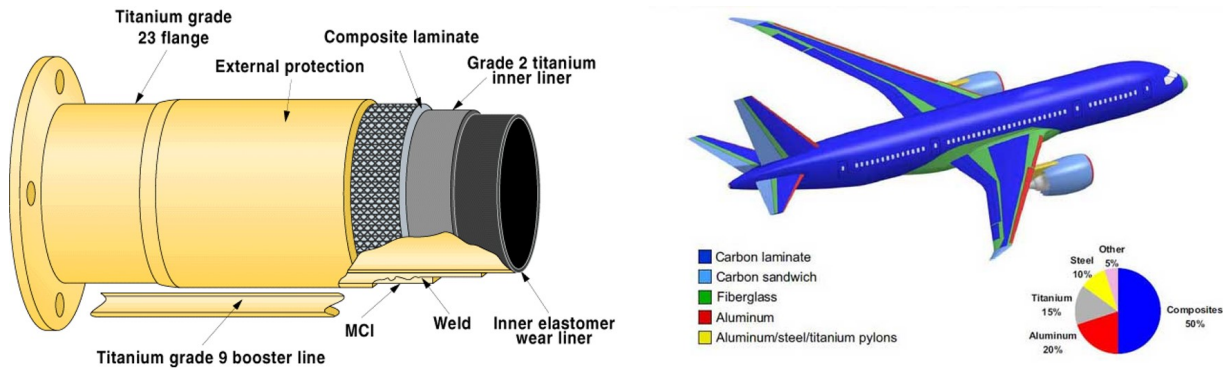


Figure 2.10: Applications of composites. Pipeline riser with composite reinforcement Boeing 787 and percentages of composites used in its structure.

[45].

automobile industry. This energy would allow the development of more intelligent systems since low-power sensors would be implemented in areas where maintenance and location are not cost-effective for extended periods of time. These inclusions have been attempted by artificially position ceramics within the composites [46] or by spreading PZT powder in the interface between prepreg layers. The enhancement of the sensitivity of piezoelectric particles has been used in the active sensing for structural health. Figure 2.11 shows an example on how the structural monitoring by placement of sensors near a damaged area can indicate a critical damage and differentiate from damage in which the structure still survives [47].

The following chapter addresses the methodology for the characterization of the smart structures. Details on procedures and machines used for this investigation are provided.

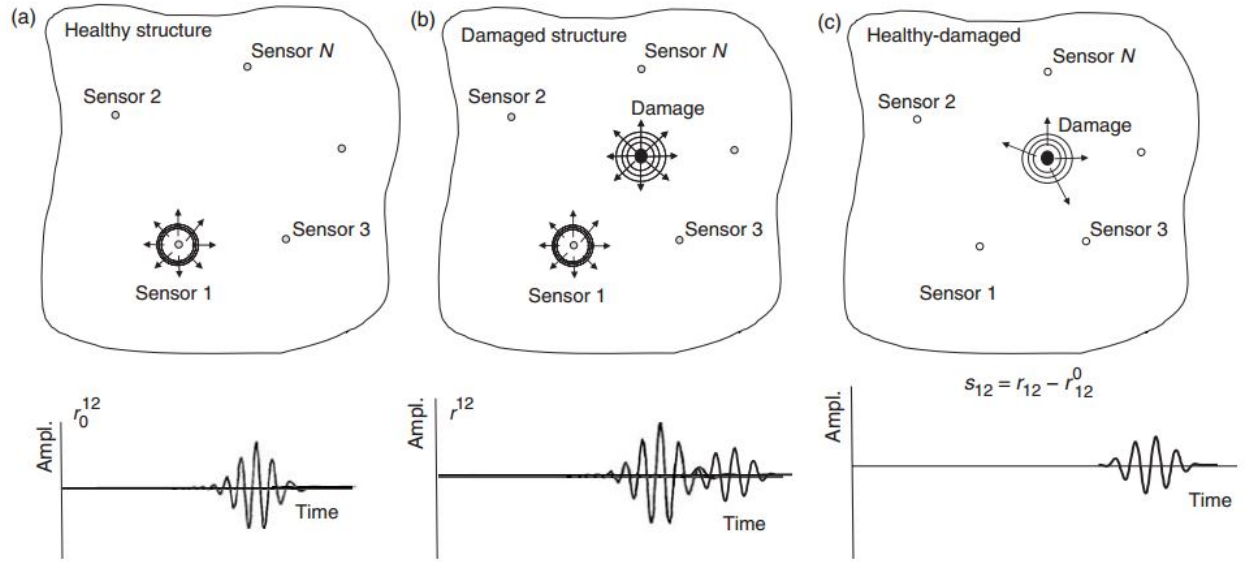


Figure 2.11: Structural health monitoring. Placement of the sensing piezoelectrics produces a shift in the impedance response depending on the damage applied to the structure [47].

Chapter 3

Methodology and Instrumentation

The characterization of the multifunctional structures was performed using different techniques. For this work, mechanical, electrical, material composition, and sensor performance were the main interest to determine from the smart structures. The methodology includes:

1. **Mechanical:** Strength and stiffness were measured using three-point bend experiments. Nanoindentation was used for those materials unsuitable for mounting on tensile/fatigue machines. ASTM standards were followed to measure density and volume fractions of composites.
2. **Electrical:** LCR meter was used to measure impedance and capacitance. Temperature dependence is shown depending on the application.
3. **Material composition:** Microscopy procedures such as SEM and optical microscopy was used to study the dispersion and visual quality of the materials. EDS determines the material composition of the analyzed surfaces.
4. **Sensor performance:** A synchronization of mechanical and electrical procedures with the use of DAQ systems allow the monitoring of the piezoelectric, pyroelectric and dielectric response of the smart structures.

In the following pages, details of the methodology and overview of the experimental procedures are explained.

3.1 Dispersion Analysis

Dispersion is one of the key parameters for the fabrication of particle reinforced polymers. Some of the techniques to achieve dispersion, most commonly used, of reinforced polymers are mechanical stirring and sonication (vibrational energy by sound waves). The measurement has been developed in the last two decades. Traditionally, optical methods

are used to evaluate the quality of dispersion. Kim et. al [48] investigated and measure the particle distribution of carbon nanotubes reinforced composites by the use of differential scanning calorimetry (DSC). This technique measured the obstacles to the cross-linking reaction of the polymeric matrix. Apart from these methods, a mathematical study of particle dispersion was presented by Yourdkhani and Hubert [48]. A simplification of their study can be observed in Figure 3.1. This figure simplifies the clustering and ideal dispersion by determining a dispersion parameter (DI). The clustered dispersion results in higher values than unity.

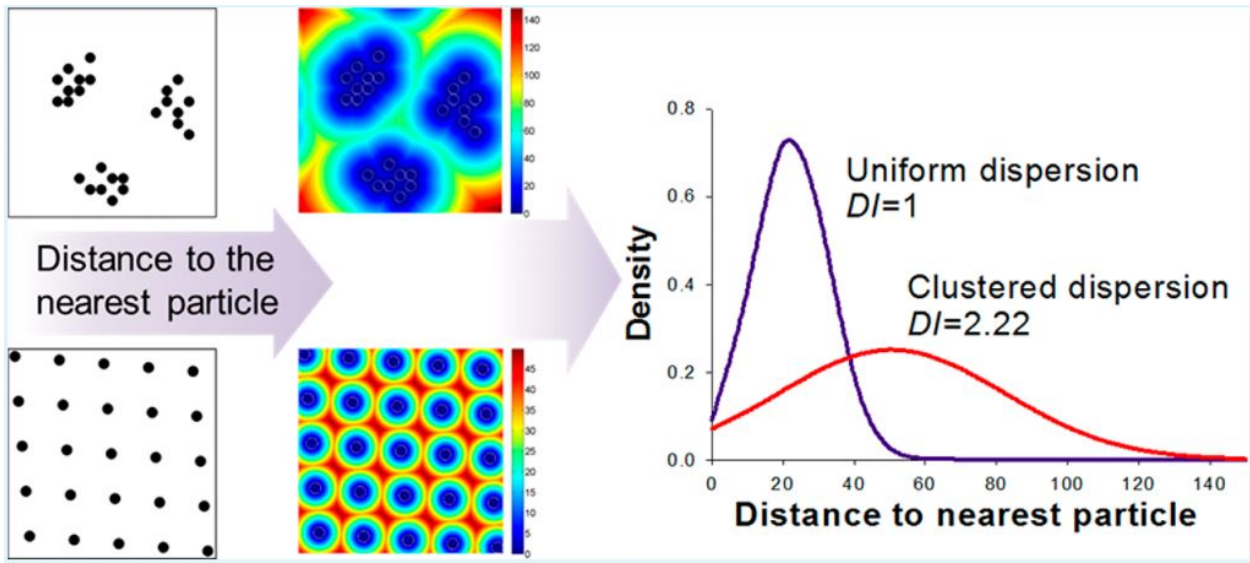


Figure 3.1: Dispersion analysis.

The algorithm to find the dispersion index DI involves to image processing. The steps of the study are summarized as follow:

1. Image processing to black/white to quantify particle count.
2. Calculate all neighboring distances d_i of each particle and obtain the mean μ_d . Assume periodic boundary conditions for elements on the edge of the micrograph.

$$\mu_d = \frac{\sum_{i=1}^{N_m} d_i}{N_m} \quad (3.1)$$

where N_m is the number of matrix elements,

3. Calculate an idealized mean μ_I where the number of particles are perfectly arranged in the given area of the micrograph.

$$\mu_I = \frac{\sum_{i=1}^{N_m} d_{i,I}}{N_m} \quad (3.2)$$

4. Calculate the dispersion index DI

$$DI = \frac{\mu}{\mu_m} \quad (3.3)$$

This technique allows a mathematical estimation to determine dispersion. Nonetheless, this technique assumes particle uniformity on their size. To address the particle size, an estimation of uniformity is done to perform the analysis, since clustering are very well represented in the DI results. This work presents optical dispersion analysis and it implements the algorithm to compare dispersion of piezoelectric particles.

3.2 Three-point Bend Testing

An approximate measure of the strength, bending modulus, and fracture toughness on flexural conditions can be found following ASTM standard. For fiber reinforced plastic composites, the span-to-thickness ratio is 32:1, and head velocity of 1 mm/min. The bar rests on two supports and is loaded by means of a loading nose midway between the supports as shown in Figure 3.2[49]. An Instron 8801 Fatigue System was selected for the tests. The

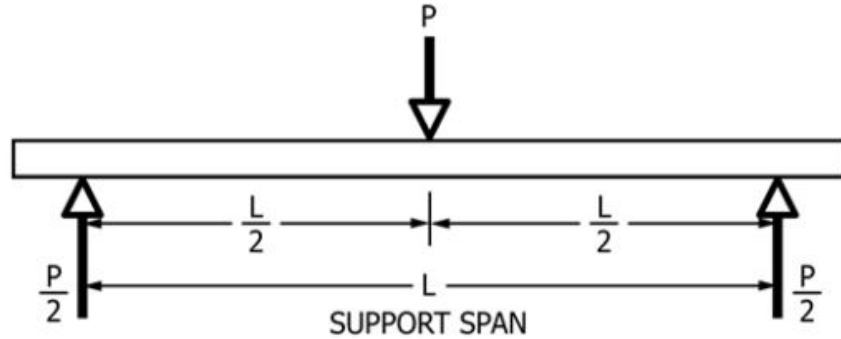


Figure 3.2: Procedure schematic for three point bending experiment [49].

flexural modulus of elasticity is the ratio of stress to corresponding strain at any given point on the stress-strain curve. For highly orthotropic composites, the equation is

$$E_f^{secant} = \frac{L^3 m}{4bh^3} \quad (3.4)$$

where E_f is the flexural secant modulus of elasticity, L is the support span, b is the width of the beam, h is the thickness of the beam, and m is the slope of the secant of the force-deflection curve.

The stress of any point on the load-deflection curve, is obtained by:

$$\sigma_{3pt} = \frac{3PL}{2bh^2} \quad (3.5)$$

where P is the applied force, and σ_{3pt} is the stress at the outer surface in the load span region. The maximum strain at the outer surface also occurs at mid span, and it may be calculated by:

$$\epsilon_{3pt} = \frac{6\delta h}{L^2} \quad (3.6)$$

where ϵ_{3pt} is the maximum strain at the outer surface, and δ is the mid-span deflection. The fracture toughness is calculated by integrating the area under the load deflection curve per volume and thickness.

$$Energy = \int_0^{\delta_f} \frac{P \cdot d\delta}{bh^2L} \quad (3.7)$$

3.3 Volume Fraction and Density Determination

The volume fraction and density determination for fiber reinforced polymer composites followed ASTM standards D792-00 (density [50]), and D2584-02 (fiber volume ratio [51]).

The procedure for the density determination of composite materials consists of the following steps:

1. Weigh the specimen in dry conditions.
2. Attach the specimen to a wire, and slightly fully submerged the sample attached to the wire. The liquid is distilled water.

3. Weigh the wire alone, partially immersed to the same point as the previous step.

Once the measurements are done, the density is determined as follow:

$$\rho = \frac{a}{a + w - b}(0.9975) \quad (3.8)$$

where a is the dry weight, b is the combined apparent wet weight, and w is the apparent weight of the wire. The density of distilled water is 0.9975 gr/cm^3 at 23°C .

Several methods exist for the determination of the fiber volume, optical analysis of the cross section and burnout method [39] are used in this work.

For composites with less than 1% porosity, the volume ratio can be obtained directly from the constituents and the gravimetric relation:

$$V_f = \frac{\rho_c - \rho_m}{\rho_f - \rho_m} \quad (3.9)$$

where the subscripts c , m , and m correspond to composite, matrix and fiber respectively.

An alternate approach is the burnout method performed at a temperature where carbon vaporizes, usually higher than 400°C . This method performs for inorganic fibers reinforcing organic fibers, such as glass/epoxy. A sample of the composite is oven dried, weighed, and then heated in the crucible until the matrix is completely burnt. The residue is washed off the ashes dried, and weighed. The volume fraction for this method is obtained by:

$$V_f = \frac{W_f/\rho_f}{W_c/\rho_c} \quad (3.10)$$

where W_F , and W_c , are the weight of the composite and fibers, respectively.

An alternative approach for woven fabric composites is to calculate a "tow volume fraction", where a micrograph is digitalized, and the pixels corresponding to the fiber section are counted and divided by the portion of the matrix.

3.4 SEM and Optical Analysis

Hitachi S-4800 Scanning Electron Microscope was used to characterize the samples. Optical analysis was also performed using an Leica Reichert MEF4 a/m optical microscope

along the cross section of the smart structures. The SEM facility can be observed in Figure 3.4.



Figure 3.3: EDS and SEM performed in Hitachi S-4800 Scanning Electron Microscope.

3.5 LCR Meter

An HP 4284A LCR meter at 1 V_{rms} with parallel equivalent circuit setup that has a frequency range from 100 Hz to 1 MHz. The LCR meter is connected to a LabView application that allows the automation of recording data for the different configurations of the system. Figure 3.5 shows the LCR meter located at the mechanical engineering facilities.

The programs used to record impedance and capacitance involved: real time at one determined frequency level (1 kHz), and point measurement with varying frequency with steps restricted to no less than 10 Hz.

3.6 Temperature Sensing Evaluation

The piezoelectric ceramics used for the fabrication of the smart structures allows having two different mechanisms of temperature effects: dielectric variation and current generated from the pyroelectric phenomena. Both techniques were used in this work.



Figure 3.4: HP LCR Meter - Automated.

3.6.1 Dynamic pyroelectric response as sensing mechanism

The pyroelectric effect is responsible for generating current under changes in temperature over time across the sample. Wireless and wired sensors have been developed using the pyroelectricity principle of these materials [52, 53]. The pyroelectric effect is responsible for generating current under changes in temperature over time across the sample. To study and get the signal from the "smart part", a picoammeter is connected to the poles of the pyroelectric ceramic. The sample is heated in furnaces or hot plates, and a thermocouple is attached to compare the response. For very precise and controlled heating, a tube furnace (Figure 3.5) is used as a heating source.

The generated current (I) through an homogenous pyroelectric material with temperature (T) at any time (t) is presented in Eq. 3.11:

$$I = \frac{dQ}{dt} = -pA \frac{dT}{dt} \quad (3.11)$$

where Q is generated charge due to temperature change, p is pyroelectric coefficient of the material, A is the surface area of the electrodes and $\frac{dT}{dt}$ is the rate of temperature change of the material with respect to time. Equation 3.11 can be rewrite into 3.12 to calculate the temperature of pyroelectric material at any time considering the initial temperature as room

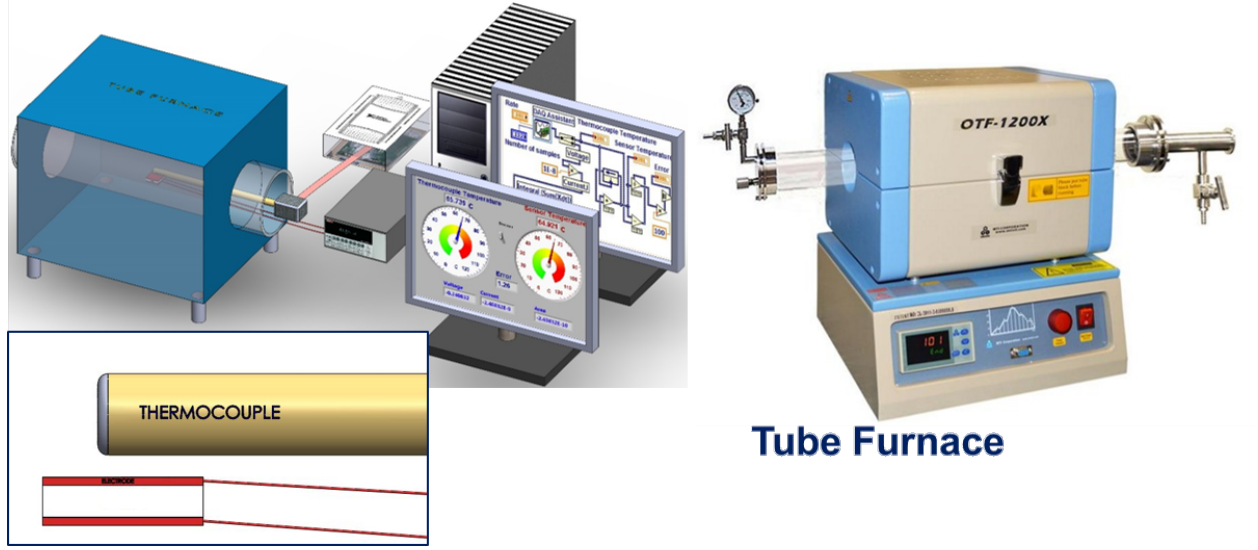


Figure 3.5: Pyroelectric testing furnace.

temperature.

$$T_f = -\frac{1}{pA} \int_{t_i}^{t_f} I dt + T_i \quad (3.12)$$

Here, T_i is the initial temperature of the pyroelectric ceramic material at time t_i , which is considered as room temperature. T_f is final temperature of the material at any time t_f . By measuring the room temperature (T_i), pyroelectric coefficient (p), electrode area (A), and the total amount of current (I) generated by the material within a certain period of time (t_i to t_f), the final temperature (T_f) can be calculated at any time (t_i).

3.6.2 Dielectric properties as temperature sensing mechanism

The second temperature sensing mechanism for dielectric components is to calibrate the response with temperature variation using the dielectric change with temperature. Many wireless [54, 55] sensing mechanisms used the variation of dielectric properties with respect to temperature to obtain a shift in the interrogation signal that shows resonance peaks.

For this study, the dielectric permittivity can be calculated directly from the wires attached to the smart structure and the capacitance using the LCR meter. The measuring of capacitance and dielectric loss is done by connecting the LCR meter and programming a LabView routine to easily stored the measuring data. A calibration of the material is desired before the

development of the "smart part".

3.7 Pressure Sensing Evaluation

The "smart parts" were tested in a Low-Capacity 8800 Servohydraulic Fatigue Testing Instron machine (see Figure 3.6). Preliminary testing was done to find the relationship between load and displacement. Displacement control was selected to define the testing parameters. The experiments methodology included a single step displacement control method, compression-compression test, at different frequencies (0.5 Hz, 1 Hz, 5 Hz, 10 Hz, 15 Hz, 20 Hz, and 25 Hz) for 100 s. To record the voltage response, a clamp was connected to electrodes of the piezoelectric material. A DAQ system from LabView or instuNet was used for recording the voltage response.

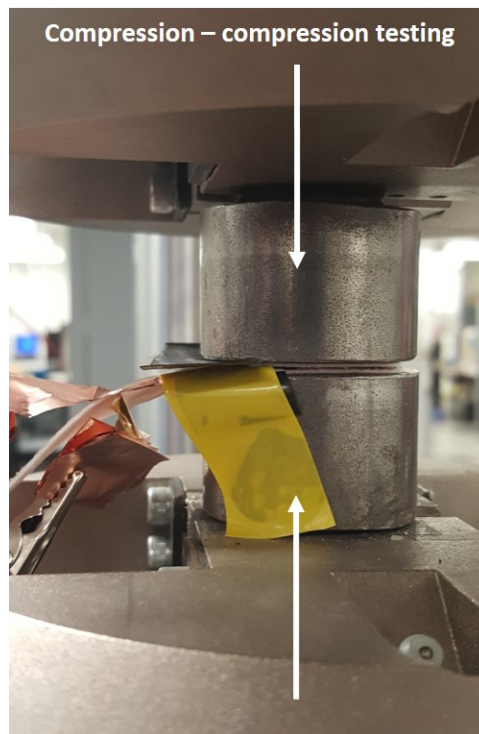


Figure 3.6: Compression compression testing.

The force range depended on the materials that are present in the "smart parts". Higher stiffness and strong materials, required a higher force to obtain a response from the piezoelectric ceramic. The parameter that characterizes the response and the effectiveness

of the design is:

$$|d_{33}|_{design} = \frac{\Delta V \cdot C}{\Delta F} \quad (3.13)$$

in which ΔV is the voltage range response of the compression-compression testing, ΔF is the force range response, and C is the capacitance measured in Farads. This equation follows the piezoelectric principle showing in Figure 2.5:

$$D_i = d_{i\mu} \cdot T_\mu \quad (3.14)$$

where D_i is charge density (CV/Area), $d_{i\mu}$ is the piezoelectric coefficient matrix, and T_μ is the stress tensor.

3.8 Nanoindentation

Nanoindentation experiments were performed on polished samples to obtain Young's modulus estimation following the procedure of Oliver and Pharr [56]. The standard procedures were followed for the setup and calibrations outlined in the user manual of Nanoindenter TI 750 Ubi User Manual. The setup for nanoindentation includes a definition of the contact area, loading condition, and location of indentation. Details are given in the following paragraphs.

- **Experimental Setup**

The contact area definition was empirically obtained from calibration procedures of nanoindenter using a sample of fused quartz or polycarbonate for softer samples. The area is fitted using:

$$A(h_C) = C_0 h_C^2 + C_1 h_C + C_2 h_C^{1/2} + C_4 h_C^{1/4} + \dots + C_8 h_C^{1/128} \quad (3.15)$$

where C_0 is defined for the indenter head. For Berkovich head, this value is 24.5.

The *load function* includes loading, holding and unloading. The maximum load was 150-200 μN to avoid breakage on ceramic materials. For very stiff metals and ceramic, the deformation does not exceed 500 nm.

A rectangular mesh pattern is selected for indentation locations. The distance between adjacent indentations is $50\text{ }\mu\text{m}$ to ensure that no plastic deformation invades the stress concentration of the neighbor points. A mesh size of 3x3 or 5x5 is selected accordingly to the quality of the surface.

- **Analysis of Indentation:** The analysis of indentation follows the procedure outlined by Oliver and Pharr [56]. The unloading slope is calculated considering 10% of total unloading displacement to perform the regression analysis. After calculating the contact area from unloading slope and the projected intersection with the x-axis, E_r is determined using Eq. 3.16

$$\frac{dP}{dh} = \frac{2}{\sqrt{\pi}} \sqrt{A_c} E_r \quad (3.16)$$

In order to decoupled the effect of the indenter from the stiffness measurements, the Eq. 3.17

$$\frac{1}{E_r} = \frac{1 - \nu_i^2}{E_i} + \frac{1 - \nu^2}{E} \quad (3.17)$$

is used with diamond properties $E_i = 1140\text{ GPa}$, $\nu_i = 0.07$.

Chapter 4

Smart Parts Development

The first work for developing smart structures is the embedding of piezoelectric ceramic in metal components using additive manufacturing for energy system applications. This chapter includes the design, fabrication, sensing demonstration and sensing performance for the smart structures developed for this research.

The chapter starts with the design and fabrication methods, addressing the initial challenge to fabricate "smart parts" successfully. It continues with the mechanical characterization and sensing evaluation, in which detail of procedures can be found in the Methodology section. Finally, performance evaluation of the sensing capabilities is presented where FEA software becomes a tool for future designs and improvement.

4.1 Fabrication

The fabrication of smart parts was done using Electron Beam Melting (EBM) machine and Selective Laser Melting (SLM). Powder of Ti-6Al-4V and Inconel was used as base materials for the fabrication. These techniques were selected because of the reduced residual stress, and the reduction time for annealing after the part is finished.

Ti-6Al-4V powder obtained from Arcam AB was used to fabricate the initial batch of smart parts. The EBM (see Figure 4.1) is a powder bed fusion technology that has the capability of fabricating metal parts from precursor powder in a layer by layer fashion. The process is done in vacuum under pressures as low as 10 nbar, this pressure minimizes any reactions of melted powder with the surrounding environment [57]. The building start with a preheating stage of the powder bed to half point of the melting point of the material used. After that, the building process starts by depositing a layer of metal powder and the electron beam selectively melting the desired positions. After the melting process, the build platform moves down to the height of the layer thickness (50 μm). A raking system spreads a new layer of powder from the powder hopper on top of the previous layer. This process continues until entire part is done. The first process of fabrication builds the base that contains the

cavity. The system stops to insert the sensor and package components within the cavity.

If needed, a mask plate is used to hold the part in the powder bed while maintaining a planar surface for the continuation of the fabrication. Alternatively, Selective laser melting

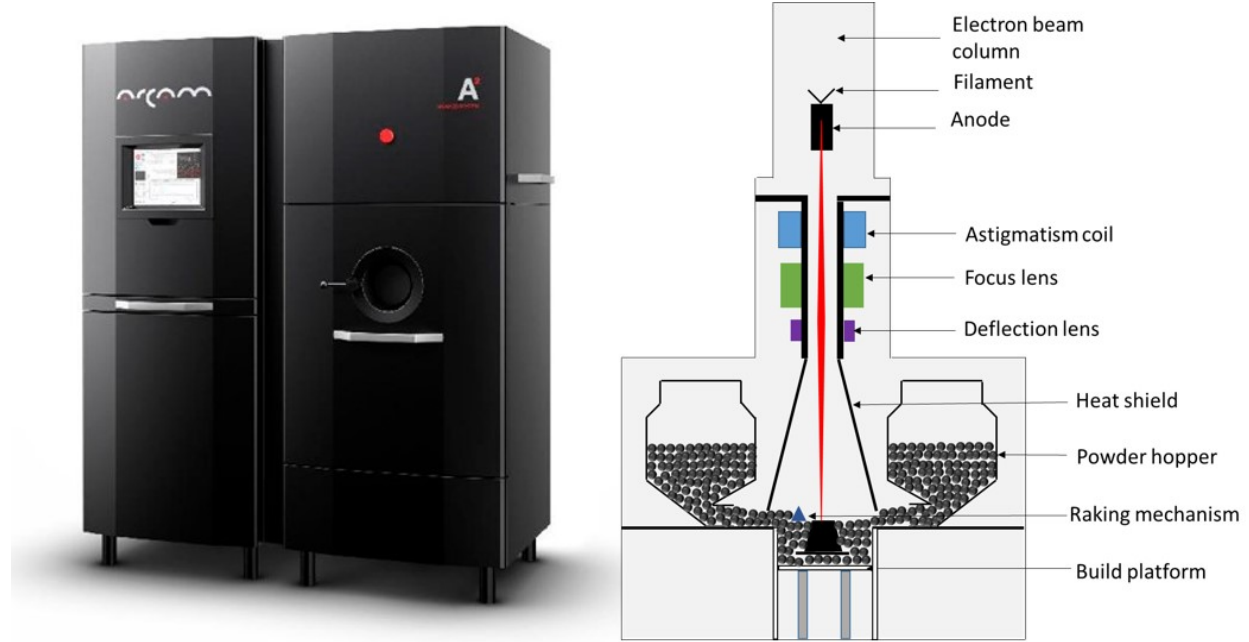


Figure 4.1: EBM schematic of smart parts.

(SLM) was used to fabricate the injector and regain usability of the first design of sensor packaging. The SLM does not operate under low pressures but in an inert atmosphere. This technology has been recognized due to its flexibility in feedstocks and shapes [58]. The process is also layer by layer fashion and the material used was Inconel. The maximum build capacity of this machine is 5 x 5 x 3 in.

The residual stresses for these techniques vary depending on the direction of analysis. For EBM parts, research has shown that residual stresses range from 0 to 180 MPa (20% of the yield strength) in compression mode for both planes X-Y and Z-axis. In contrast, SLM showed both tensile and compressive stress in the Z-plane and X-plane respectively. In average, the EBM showed lower residual stresses ranging from 40-120 MPa compared to SLM range 70-210 MPa in the X-plane directions [59]. For both techniques, "stop and go" process was implemented to insert the sensor components in the designed cavity.

4.1.1 Stop and go process

The fabrication of "smart parts" is a multi-step process, which is achieved by interrupting the EBM/SLM fabrication after the desired position is sufficient to embed the piezoelectric ceramic. Once the sensor components are embedded in the designed cavity, the process continues to finish the fabrication by building the top part of the structure. This entire fabrication process is referred as "stop and go" process and it consists of six steps (see Figure 4.2) :

1. Fabrication of the first or bottom part (with a cavity) using EBM system.
2. Cutting off the "insert part" from Ti-6Al-4V bar.
3. Interruption of the fabrication and embedding of the piezoceramic sensor.
4. Machining of the mask plate using CNC Mini Mill 2 (HAAS Automatic Inc. USA) machine.
5. Press fitting of the bottom part in the mask plate and aligning of the top surface.
6. Fabrication of the rest of the part (on top of the bottom part).
7. Cleaning of the finished smart part.

4.1.2 Piezoelectric ceramic

The piezoceramic chosen for this application is Lithium Niobate (LiNbO_3) due to its high Curie-temperature (1100°C) and PZT-5A due to its high piezoelectric coefficient, although its Curie temperature is 350°C , it is widely used for piezoelectric applications and ideal for low temperature applications. The PZT and LiNbO_3 was commercially purchased from Piezo Systems Inc. [60].

The ceramics contained a conductive surface to make a direct connection to the intended application. For the EBM procedure, the conductive surface was removed by etching the pieces of the ceramic in nitric acid. The removal of the conductive surface avoids oxidation and vaporization of the metallic surface. For the SLM technique, the fabricated results

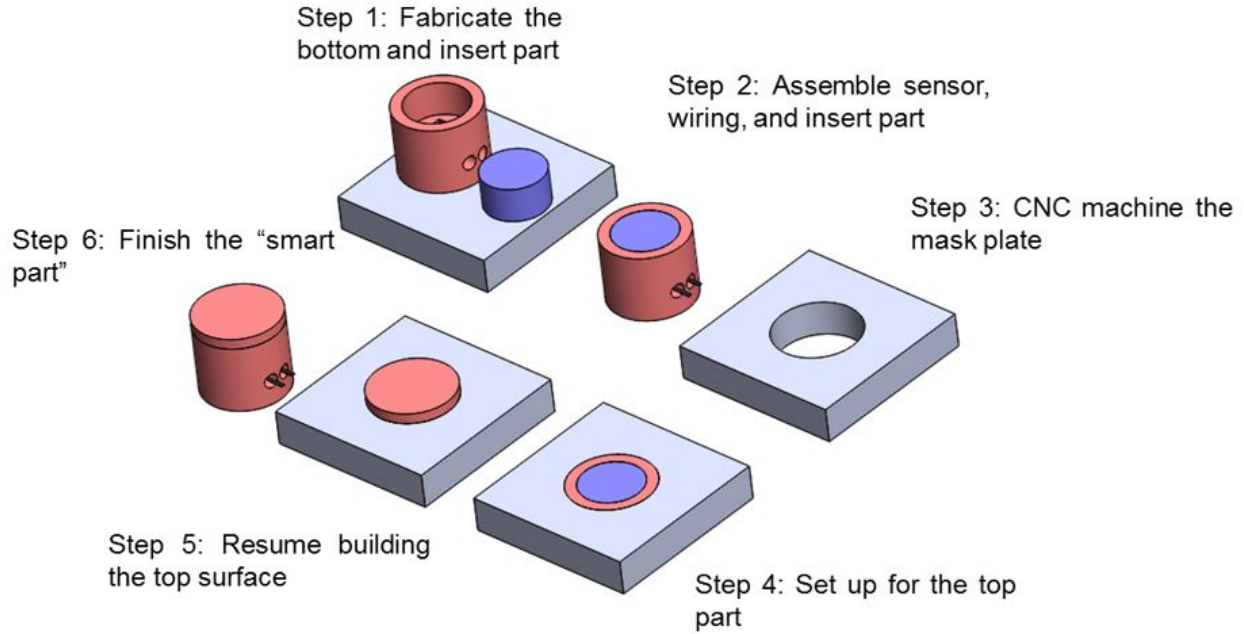


Figure 4.2: Stop-and-go process during EBM fabrication.

showed that the temperature and pressure does not cause the vaporization of the conductive surfaces.

4.1.3 High temperature wiring

The purpose of high-temperature wiring is to get a sensing signal out from the piezoceramic sensor at high-temperatures. The wiring needed for this type of application needs to meet special demands. The wiring must be able to resist high-temperatures and harsh-environments. Thus a metal with a high-melting point which is corrosion and oxidation resistant is preferable. The wiring must also offer adequate electrical conductivity (low electrical resistivity to better transmit and reduce noise of the sensing signal out from the piezoceramic sensor). One popular wiring material that meets these requirements is Platinum: a chemically stable metal at high-temperatures and harsh-environments with good electrical conductivity. Titanium also has a high-melting point and is corrosion resistant; it is also chemically similar to the building material used to manufacture the sensor structure, and thus should not pose a powder contamination problem during the EBM build phase. The electrical conductivity of Titanium is not as good as Platinum, but it is considerably

Table 4.1: Comparison of materials suitable for electrode fabrication of smart parts.

<i>Wiring Material</i>	<i>Melting Point</i>	<i>Electrical Resistivity (20 °C)</i>
Platinum	1768.3 °C	105 nΩ·m
Titanium	1668 °C	420 nΩ·m
Stainless Steel	1440 °C	690 nΩ·m
Tungsten	3370 °C	56.5 nΩ·m

more inexpensive. Titanium will be considered to prove the concept that a sensing signal can be transmitted out of the piezoceramic sensor. Tungsten provides highest melting temperature and stability during fabrication inside the EBM. In contrast, stainless steel foil is more flexible and durable compared to tungsten and titanium foils. Once parameters for the manufacturing and parts fitting of the whole sensor structure have been refined, Platinum will be used as the wiring material of choice. Melting point, and electrical resistivity values are given in Table 4.1.

4.1.4 Initial design

The circular shape "smart part" was fabricated in oppose to the rectangular one to avoid registration issue during fabrication of the top part. The diameter of the circular shape "smart part" was 24.35 mm and overall height was 15.15 mm. Because of the shrinkage and some un-sintered powder left in the hole, the diameter of the cavity reduced by 12.8%. The "smart cylinder" was fabricated using the "stop and go" process (shown Figure 4.3). The process allows the insertion of piezoceramic sensor in the designed cavity. The sensor components are protected by positioned an insert part that allows the leveling for the second fabrication. Finally, a mask plate is used to secure the sensor structure to continue the fabrication. The top part continues to build onto the bottom part. Misalignment between the top and the bottom part was found after the fabrication due to the misalignment of the electron beam. The fabrication process confirms the multiple step fabrication using electron beam melting (EBM) system and the advantage of embedding smart components compared to traditional methods of machining. Different materials were used to withstand the harsh conditions during the second fabrication. Alumina clothing was used to protect the interior.

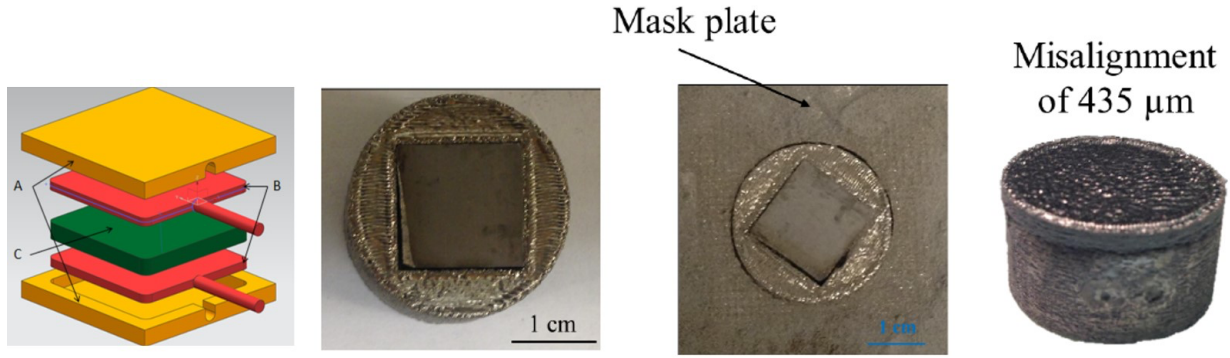


Figure 4.3: Fabricated 1st design. Schematic view of the assembly and the top view of the smart part with sensor components before being placed on the mask plate. The fabrication finished with misalignment of 435 μm .

Similarly, wires and foil of titanium and stainless steel were used in different occasions and configurations. This simple design showed a systematic shortage of the piezoelectric ceramic due to metallization within the cavity in the EBM machine. Such metallization did not occur in the SLM machine.

This arrangement of sensor components was used for the fabrication of "smart injector" and "smart cylinders" using Selective Laser Melting (SLM). This fabrication method uses inconel powder instead of Ti-6Al-4V, operates under lower temperature conditions and it was confirmed that metallization does not occur within the piezoelectric thickness, nor diffusion from metallic electrodes to its neighboring contact surfaces.

4.1.5 Assessment of fabrication procedures

To investigate the cause of sensing electrical shorting after the fabrication, the completed parts were sectioned from the top to access the sensor and components and observe its condition. The parts exposed to the EBM were compared to the original parts, and a visible dark coating was present in all parts as shown in Figure 4.4. The conductive coating appears to be as metal coating that occurred during the second fabrication, when the powder and the bed was heated to temperatures close to the melting point of the metal. The characterization of the metallization was analyzed by conducting SEM and EDS. Two samples

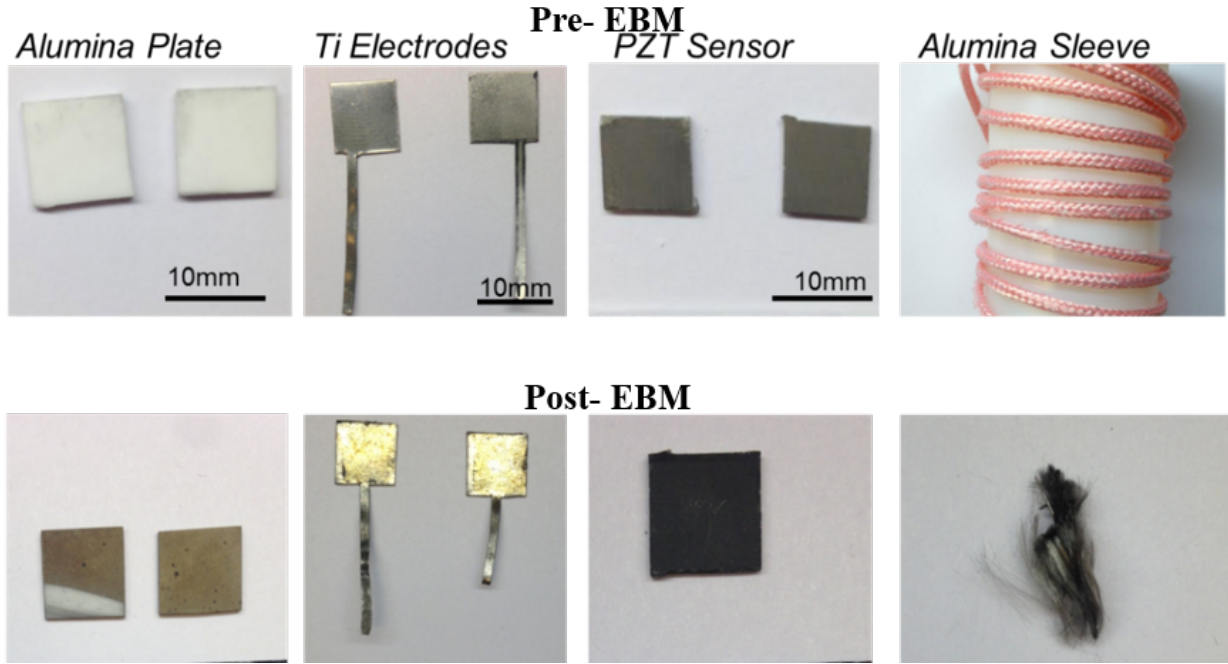


Figure 4.4: Parts included for embedding of sensor inside "smart part". Top images are as-bought before EBM fabrication, where bottom images include post EBM fabrication.

of alumina plate, as-bought and post-EBM were analyzed and compared under the SEM. Figure 4.5(a) shows the SEM image of alumina plate as bought, where Figure 4.5(b) shows the SEM image of alumina after the EBM second fabrication. Table 4.2 shows the difference in composition that is present for both as pre-EBM and post-EBM samples considering only the surface of the alumina. The post-EBM sample has additional titanium that was present, which may be the metal coating that is present on surface. One of the main issues in metallization is assumed to be caused by metal vapor created during fabrication. As the Ti-6Al-4V powder consists of three different components which have different vaporization temperature, diffusion from metal vapor-to-solid and metal powder-solid were thought to be the cause. The vaporization temperature is even low due to the vacuum fabrication process. In consequence, any components of the Ti-6Al-4V fabricated parts may metalize the sensor assembly. As a result, insulating components becomes conductive, and shortage of electrical current occurs.

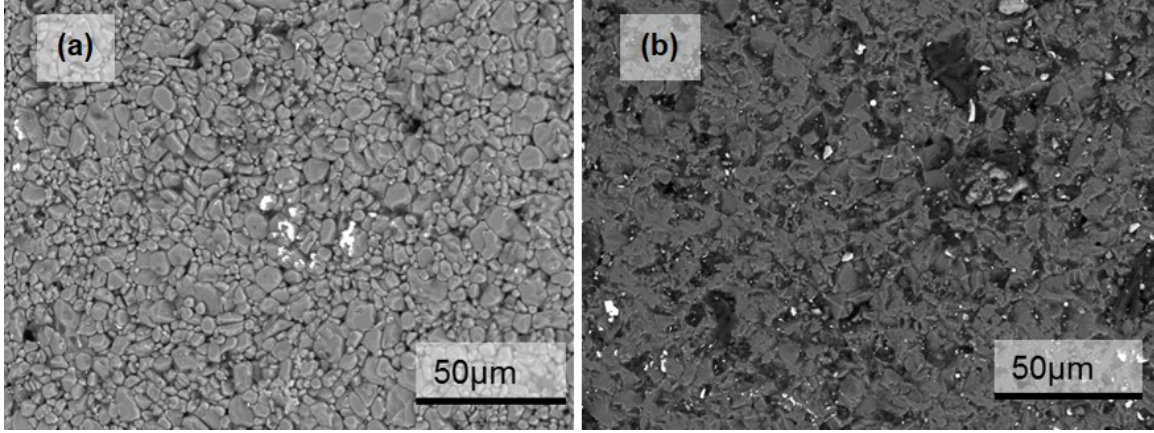


Figure 4.5: Design B of "smart Part".(a) Shows the bottom part with embedded sensor (b) Top view of finished part (c) Side view of finished part.

Table 4.2: EDS results for the alumina plates. Comparison before and after second fabrication.

Element	<i>Pre-EBM</i>	<i>Post-EBM</i>
Aluminum	98.5%	89.3 %
Silicon	1.5%	3.6 %
Titanium	0%	4.2 %

4.1.6 Protective Housing development

New packaging procedures were developed to protect sensing parts from powder and vapor diffusion. To minimize powder exposure, an isolation cap was designed and attached to the mask plate. The fabricated isolation cap is shown in Figure 4.6. The mask plate was machined to improve the sealing with the isolation cap to minimize metal powder and vapor. Additionally, a development of an electrical insulation package was designed and machined that acted as a barrier from contact with evaporated metals during the EBM fabrication. Several designs were proposed to address ease of fabrication, maneuverability, and efficiency. Three designs were developed using manual and computer numerical control (CNC) milling machines. An optimized design addressed all the issues and time of fabrication was minimized. The final design is shown in 4.7. The machining process for such small

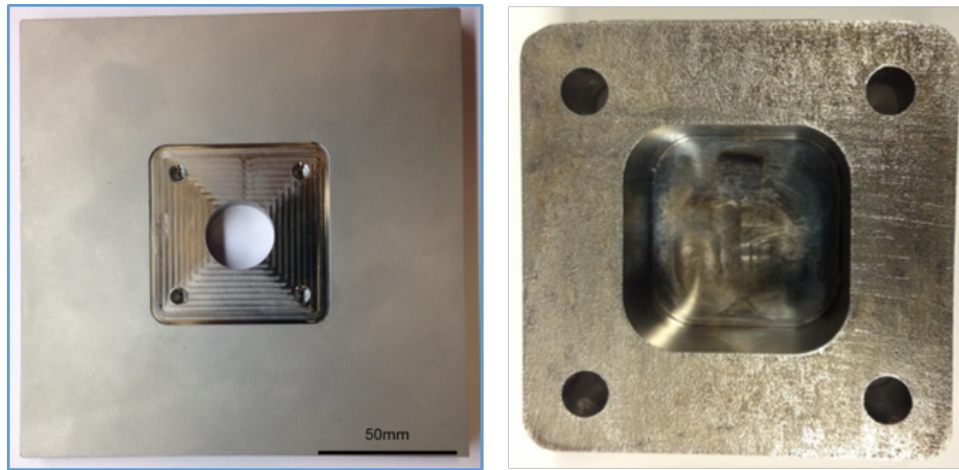


Figure 4.6: Modified mask plate using the bottom isolation cap to prevent powder contact with the "smart part".

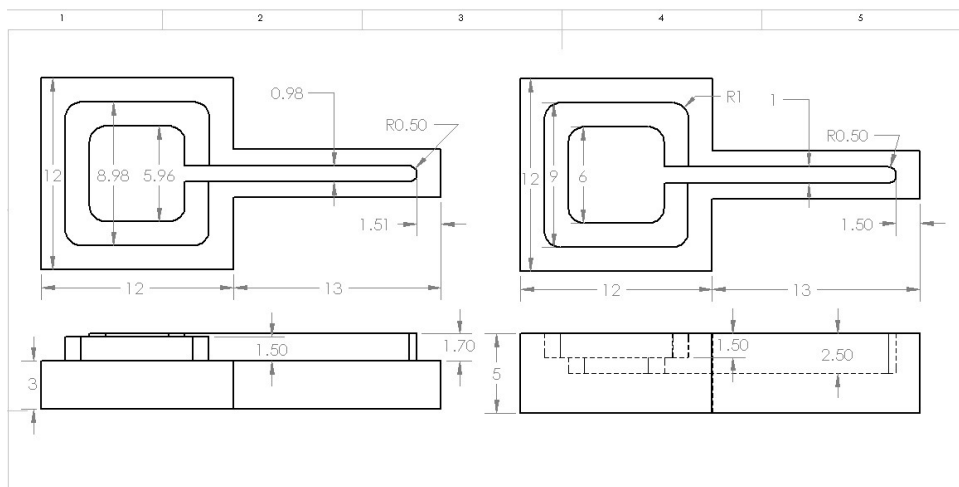


Figure 4.7: Optimized design for a non-electrical conductive package of smart parts.

components of alumina involved the following:

1. Cutting block of alumina using cut-off wheels to get strips of approximate final size.
2. Attach the strips of alumina into an aluminum block that serves as base and holder for milling machines, by using cyanoacrylates adhesive (superglue).
3. Attachment on the top surface allows the proper facing in the height, length and width for the final design.

4. CNC milling machine is programmed and provides the final pieces.
5. After fabrication, the aluminum base, and the package is submerged in acetone to remove the adhesive. Final and detail imperfections are sanded using sanding disks or by hand.

Once the package is ready to handle, the sensor is build up inside the cavity (see Figure 4.8). The package was assembled and was ready to be inserted in the cavity of the bottom



Figure 4.8: Fabrication procedure of smart parts. Alumina housing machining.

part of the smart structure.

Exploring alternative methods of package fabrication was fundamental to explore optimal designs for easier manufacturing. Techniques such as injection molding of paste alumina, 3D printing of alumina package, and protective electrical ceramic spray on metal based package were developed. The porosity of the alumina paste and the 3D printing ceramic was not an effective barrier against diffusion. The voids within these materials worked as interstitial positions and metallization were generalized throughout the part. In contrast, the metal based package is immune to the diffusion, but the adhesive on the interface between the protective coating and the metallic surface was not strong enough to withstand handling at room temperatures. These alternatives are shown in Figure 4.9. The use of machinable alumina instead of fired alumina decreases its overall strength. To make up for the machinable alumina, doubling the thickness is needed to withstand pressure and handling during fabrication of the EBM. As a comparison, Figure 4.10 shows the nanoindentation modu-

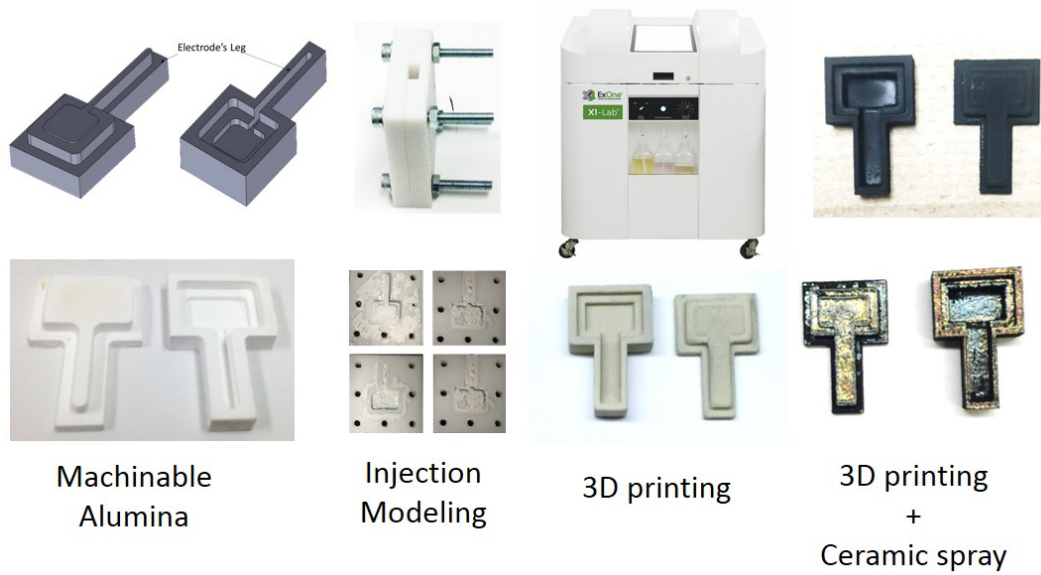


Figure 4.9: Alternative methods of packaging fabrication for smart parts using EBM.

lus of machinable and fired alumina. The stiffness is reduced by half when the machinable counterpart is selected.

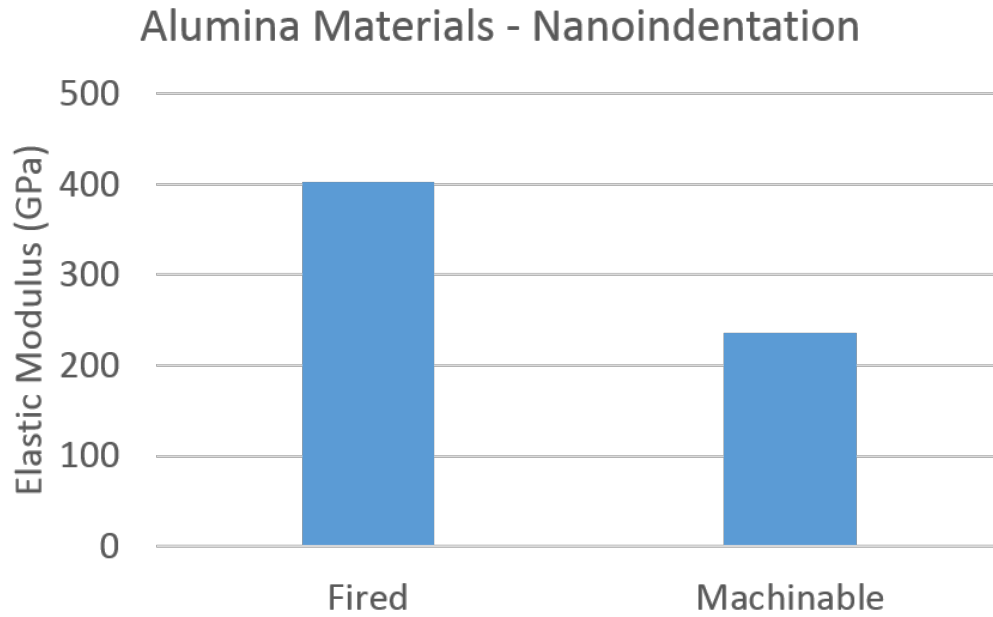


Figure 4.10: Nanoindentation modulus of machinable and fired alumina used for fabrication of smart parts. No. of points analyzed: 8.

4.1.7 Modified design

The need of a sensor package modified the geometry of the metallic components. The bottom part, the cavity, and insert part were modified accordingly. The final smart cylinder was designed to 24 mm in diameter and 28 mm in height. The schematic view of the assembly process is shown in Figure 4.11. The schematic shows the assembly before the second fabrication of the smart parts. The sensor is placed between the tungsten electrodes and they are protected by the sensor housing. The cylinder is designed to act on the Z-direction or building direction, therefore the stacking direction follows the same pattern. Once the insert part is placed, the top face of the cylinder is leveled to continue on the second fabrication. The building and fabrication of smart cylinder can be observed in Figure 4.13. Figure 4.13 indicates the insertion of the alumina package that contains the electrodes and the piezoelectric ceramic, and the insert part to close and level the cavity for the second fabrication. Figure 4.13b, shows the completion of the smart cylinder after the second fabrication. As it can be seen, the alumina package was contaminated with metallic components and its

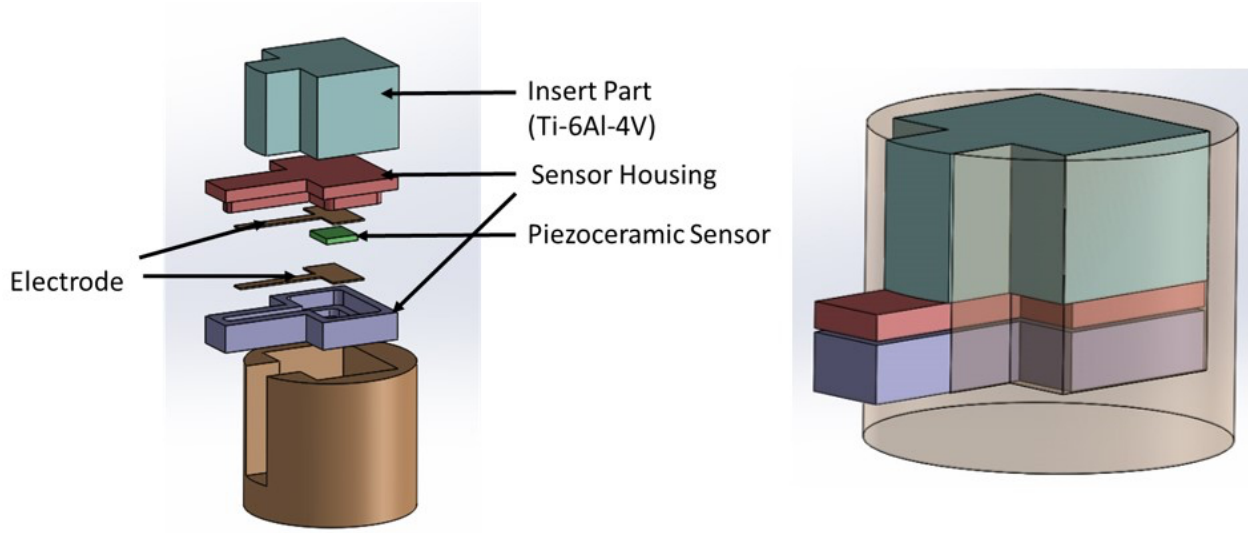


Figure 4.11: Test cylinder schematic.

surface turn to a gray color. Once separated from the mask plate, the legs of the sensor package are broken, and the electrodes are exposed to be connected to a DAQ system and obtain the sensing signal (see Figure 4.13c).

Similarly, the smart tube was adapted to have a cavity suitable for the housing and sensor components. The fabrication process, the base, and the insert part were changed to built a tube with an embedding sensor. A schematic view of the test tube is shown in 4.1.7. The assembly direction of the sensor components is changed to the radial direction with respect to the centerline of the tube. The stacking direction is perpendicular to the building direction, and the insert part is modified to address the change of geometry of the cavity. Similarly, as the the test cylinder, the insert part leveled the face in which the second fabrication will continue on top of the test tube.

For the smart tube, a modified fabrication direction was selected to address the geometry of the hollow tube. The fabrication of the smart tube is shown in Figure 4.14. The assembly of the bottom and insert part of the tube is observed in Figure 4.14. The completed test tube shows the same contamination of the alumina package in Figure 4.14. Similar procedure after fabrication was followed to evaluate the smart tube performance.

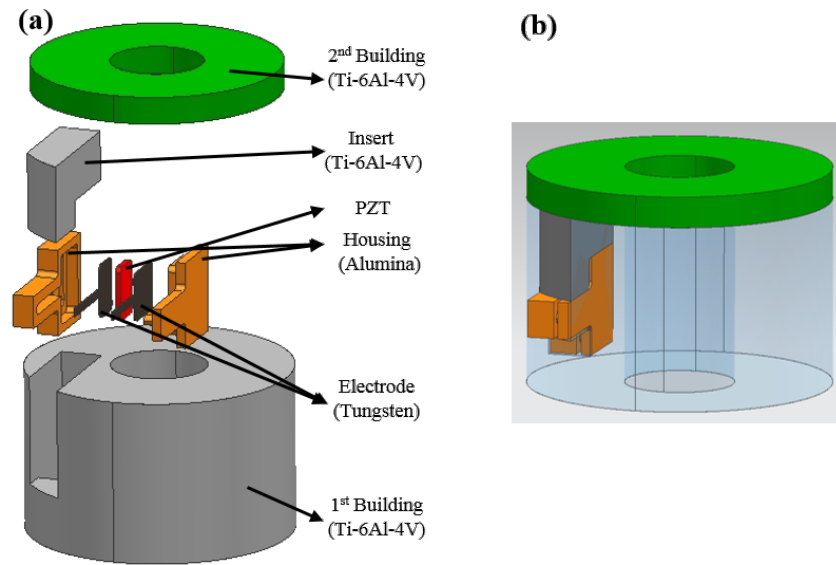


Figure 4.12: Test tube schematic.

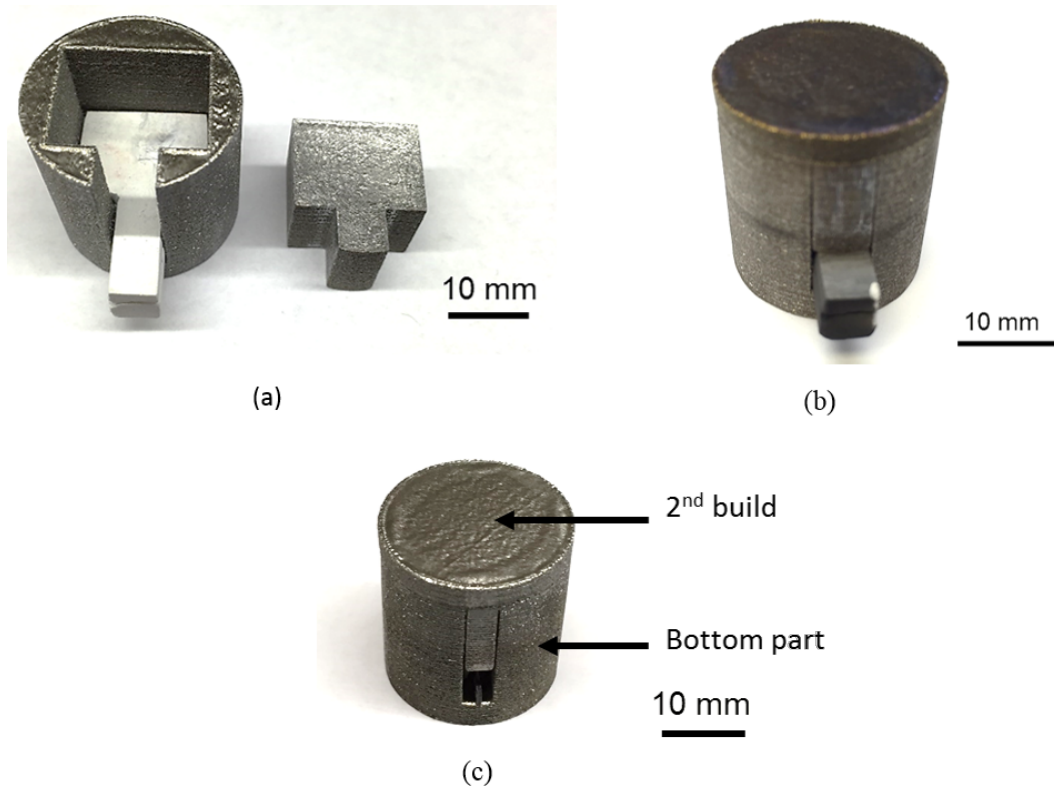


Figure 4.13: Successful building using machinable alumina and EBM (2nd design).

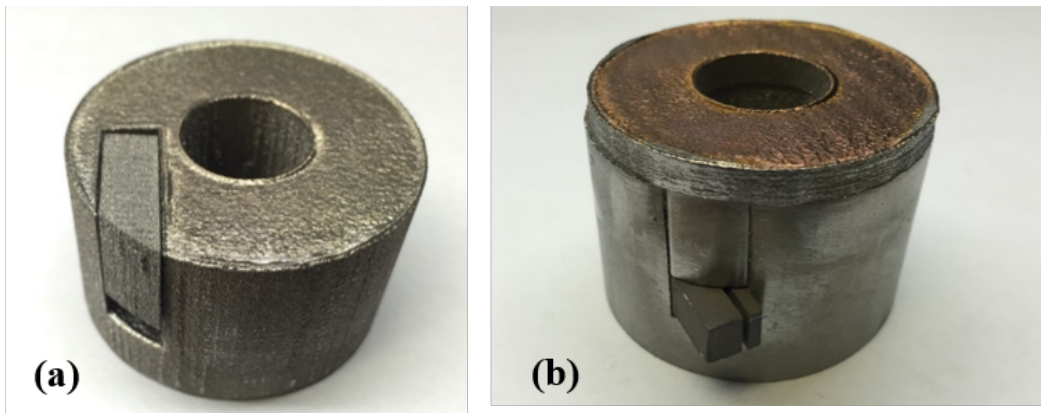


Figure 4.14: Smart tube fabrication using machinable alumina package and modified design of sensor packaging.

4.2 Characterization of smart parts

The characterization of smart parts followed microstructure analysis of the stop-and-go process and metal composition. To improve interface bonding, among different techniques, hipping was selected to its proven effectiveness in increasing density and reducing voids. The results showed the improvements and drawbacks of the technique. The sensing is characterized by analyzing the piezoelectric response, the pyroelectric response as a dynamic method for temperature sensing, and capacitance analysis.

4.2.1 Microstructure analysis

After a successful fabrication using the EBM with the "stop-and-go" process, the part was cross-sectioned for nanoindentation and microstructure analysis. The first design was sectioned using the Buehler Isomet 4000 Linear Precision Saw. The sectioned part was then polished and etched using Kroll's Reagent. After etching, the part was looked under the microscope. Figure 4.15 shows the top and bottom sections microstructures. Both sections have a similar Widmanstatten or Lamellar-like microstructure with alternating α and β phases. The insert plate showed a more equiaxed α and β mixture microstructure, which may have better isotropic properties when compared to the bottom and top sections. The discontinuity at the interface affects the mechanical properties of the "smart parts". For

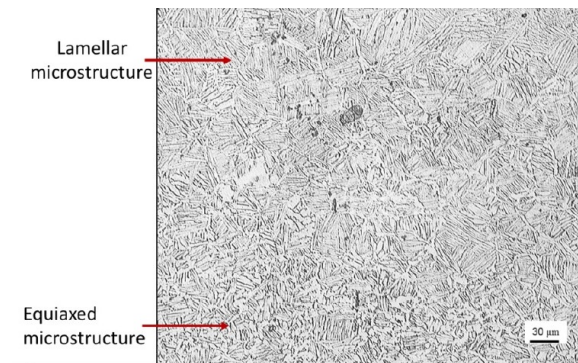


Figure 4.15: Interface between the insert plate and the top section of the "smart part" at 20X.

validation of mechanical stiffness of the fabricated parts, nanoindentation was performed on a

piece of Ti64 after fabrication. The testing was done in a Hysitron TI 750 Ubi Triboindenter. The results included 38 points with varying force ranging between 100 μN and 10 mN. The results showed a samples strain Youngs modulus of 142.66 ± 15.47 GPa with minimum and maximum value yielding in 107.5 GPa and 183.5 GPa respectively. These results fall within the range of reported Ti64 (annealed) and from the tensile test performed in parts fabricated for this project. Similarly, the hardness averaged 6.70 ± 1.773 GPa. Hardness calculation underestimates the true value since the contact area is much less than the final impression after the test ends. Measurement of the final impression of indentation requires higher capabilities of the machine.

Finally, after the successful building of the modified design for the smart cylinder, a cross section was analyzed using optical microscopy. Figure 4.16 (a), and (b) shows the microstructure of the bottom and the top part, which are within 1 mm from the first build, and interface position, respectively. Since the bottom and top part followed the same fabrication patterns, it was expected from both to have similar microstructure. The lamellar-like microstructure, alternating α and β phases were observed in both the bottom and top section. The grain size of the bottom section is longer than the top, which attributes to the time of sintering during the first fabrication compared to the second fabrication. To fully understand this behavior a full evaluation considering the thermal variation is needed. Figure 4.16 (c) shows the interface resulted from the "stop-and-go" process. The image shows a discontinuity between the bottom and top sections. At the interface, the bottom part shows relatively larger grain growth when compared to the top part. This difference is caused due to the extra preheating and heating during the second fabrication process. The structural integrity is clearly affected at the interface of the smart structure.

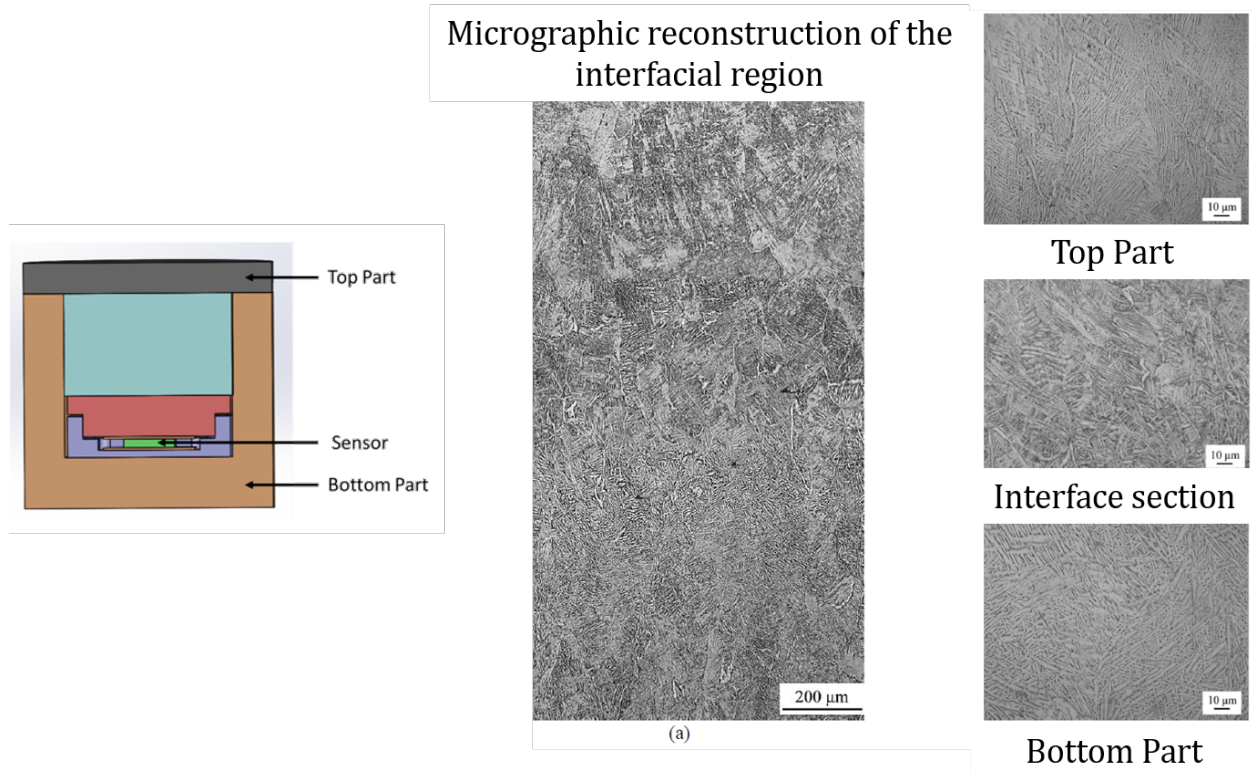


Figure 4.16: Microstructure analysis of smart part, (a) Reconstruction of the interfacial region. The measurement in the grain size shows a mismatch from $1.36\ \mu\text{m}$ to $0.45\ \mu\text{m}$ from bottom to interfacial region. Measurements were done optically with pixel proportionality.

4.2.2 HIPping effects

The interface resulted from the "stop-and-go" process caused a brittle like behavior in metal samples. This brittle behavior occurs at the interface by sudden separation. To address the weak boundary, techniques such double and triple melting during fabrication, as well as Hot Isostatic Pressing (HIPping) technology were studied in cylindrically shaped samples under tensile testing. Double and triple melting were selected to increase the heating and sintering of the powder. Contrarily, HIPping technology has been proven to minimize or eliminate pores [61]. The HIPping process is done under high pressures (up to 207 MPa) and high temperatures (up to 1400 °C) in an inert atmosphere (argon) [62]. The process consists in applying uniform "isostatic" pressure in all directions. No shear or failure occurs during this process, but the surfaces of the voids diffusion bond together to effectively reduce the defects. Mechanical properties are enhanced, and density increases.

After subjecting the smart parts to this process, tensile strain showed not a significant improvement in the mechanical properties. Tensile strength improved by 20%, and Young's Modulus and ultimate strength enhanced by 8.2%. Results show that although density and strength increase, the toughness parameter was not significantly improved. Failure mode was very similar to fabricated parts. Figure 4.17 shows the results from the tensile testing results as fabricated using the "stop-an-go" process.

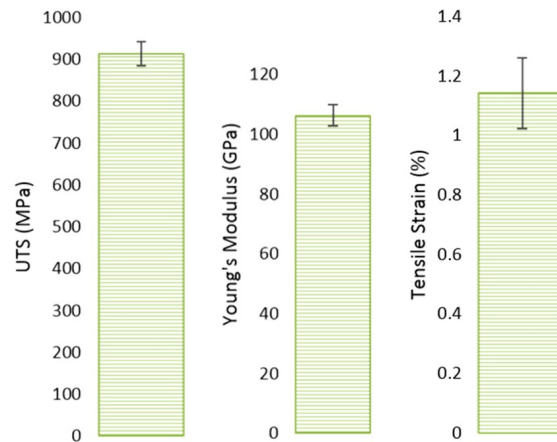


Figure 4.17: Ultimate strength, young's modulus and tensile strain of samples fabricated using "stop-and-go" process. Number of samples tested: 5

4.2.3 Force-pressure characterization

The evaluation of the smart parts involved an initial assessment of the electrical components, a re-poling of the piezoelectric material and a study of the piezoelectric response under different loading conditions. The evaluation of the electrical components is performed by measuring the open circuit condition of the piezoelectric ceramic among the electrodes. The electrodes are exposed by carefully breaking the alumina protection that covers them (legs in Figure 4.13), and adding a dielectric between the electrodes to avoid contact during the experiment. The resistance is measured using a clamp and a multimeter; an open loop condition provides the verification to continue the evaluation on the smart part.

Secondly, a re-poling of the piezoelectric material is necessary for those materials exceeding the Curie temperature during fabrication (PZT, Curie temperature is 350°C [60]). The re-poling is done by applying a constant electric field using a power supply and increasing the temperature of the smart part to reduce the overall time. It has been shown that electric fields as low as 1.3 kV/mm can almost entirely recover the piezoelectric coefficient (d_{33}) of the PZT at room temperature or by any other combination of heat and time during re-poling [19]. For this case, the smart part was heated at 120°C and the electric field of 1.4 kV/mm during 4 hrs.

The smart part was loaded in the Instron machine (see Methodology for details) to test its signal response. Because of the testing setup, a predefined stress was needed on the sensor before testing. This stress was defined by choosing a safe value for the piezoelectric ceramic, for this case 1 MPa allowed to a maximum force of 40 kN . A setup of the test in the smart parts is in Figure 4.18.

The results obtained from the experiments showed good agreement in the frequency and very low noise for the Instron machine outputs. Human error and noise levels were presented in the voltage readings. The shifting caused by the human synchronization of the DAQ was reduced by correcting the time axis of the voltage with the first peak of the force output. Additionally, a smooth process and FFT signal cleaning were done in the voltage signal to preserve true peaks heights and widths. Figure 4.19 shows the response of the smart cylinder under different force frequencies. The agreement is accurate and

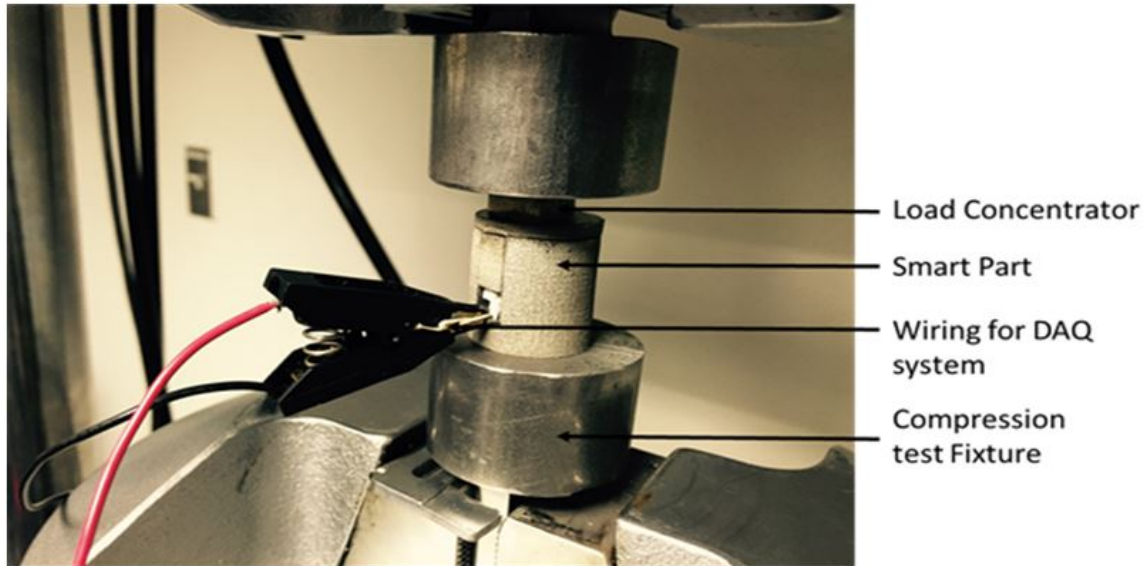


Figure 4.18: Setup for smart cylinder position in Low-Capacity 8800 Servohydraulic Fatigue Testing Instron machine.

the trend support documented frequency dependent response on the piezoelectric materials. Furthermore, a combined analysis is focused on studying the ratio between amplitude of force to voltage. The results from the smart part on considering different values of frequency are summarized in Figure 4.20. The ratio of voltage-to-force was calculated in order to compare different sensitivities among the tested frequencies. Results showed that there was a clear trend between the amplitude of the voltage generated and the frequency of the force. The sensitivity can be converted in an effective piezoelectric response using Eq. 3.13. By multiplying the sensitivity by its capacitance, the effective piezoelectric response of this cylinder becomes 0.3563 pC/N, 0.2858 pC/N, 0.2953 pC/N, and 0.2782 pC/N for 10 Hz, 15 Hz, 20 Hz, and 25 Hz, respectively.

An analysis for static pressure sensor was studied by subjecting a smart cylinder to a stair force input. This excitation force builds up the stress within the cylinder, and the voltage is generated when the machined increase by impulse the force within the cylinder (see Figure 4.21). When the cumulative voltage is calculated, it can be observed a proportional trace of the voltage with respect to the force (see Figure 4.22). This method of sensing pressure is dependent on two conditions:

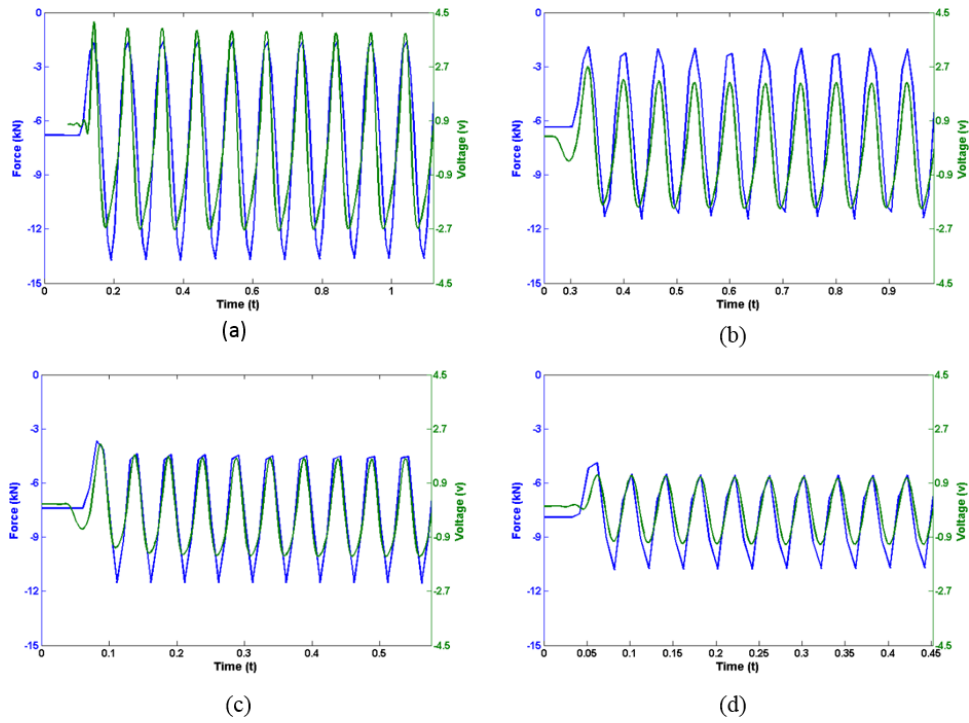


Figure 4.19: Response of smart cylinder pressure testing.

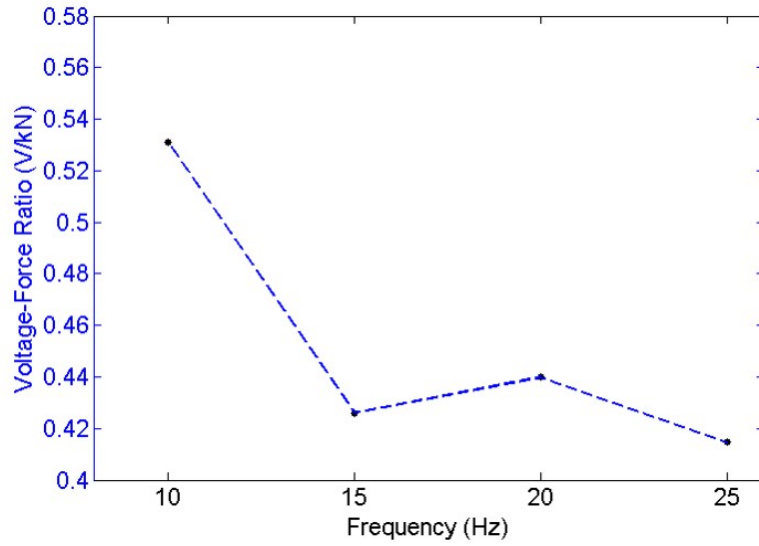


Figure 4.20: Sensitivity of smart cylinder pressure testing response.

1. The piezoelectric ceramic can be modeled as LCR circuit. Since this material is ideal for dynamic response, under quasi-static response the energy dissipation is significant. For a pressure sensing device, the deformation rate on the piezoelectric has to exceed

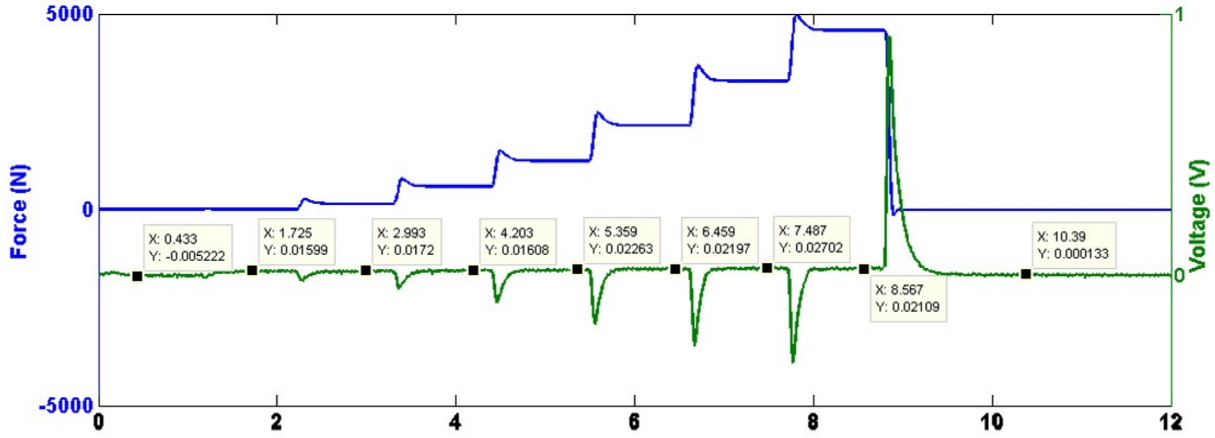


Figure 4.21: Force pressure in dynamic form. Stair response.

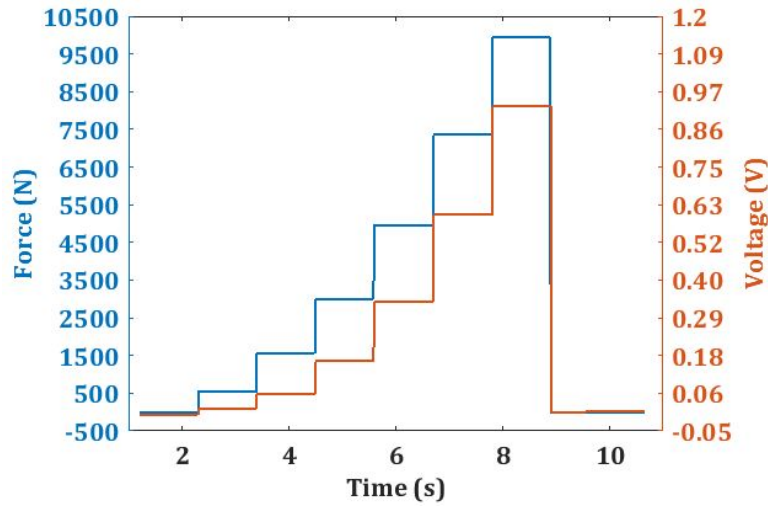


Figure 4.22: Cumulative voltage and force impulse from stair experiment.

the dissipation energy within the piezoelectric. For a pressure that builds up slowly within the piezoelectric, other pressure sensing mechanisms must be considered.

2. The piezoelectric constant is dependent on the average stress. Proper calibration of the back calculated pressure must be considered the change of piezoelectric constant with respect to average pressure.

In similar fashion, the sensing of the "smart tube" was measured under similar conditions. For this test, special fixtures were machined to adapt the curvature of the "smart

tube” (see Figure 4.23). In this experiment, the ”smart tube” was compressed at about 0.3 mm, which can be referred as the average compression. Then, the part was compressed under a cyclic displacement of 0.1 mm at different frequencies of 1 Hz, 10 Hz, and 15 Hz. The DAQ system was used to record the voltage response. The voltage and force responses are

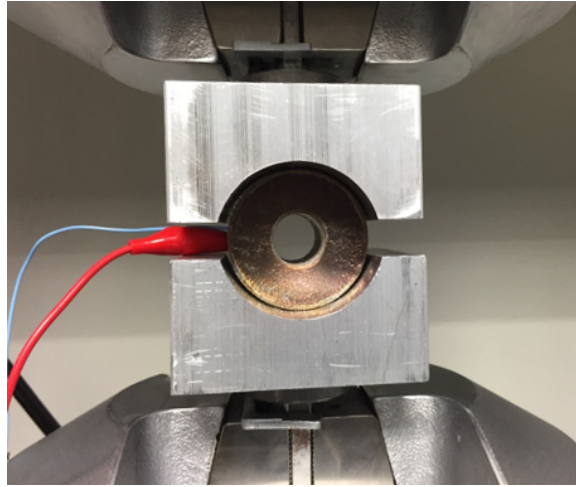


Figure 4.23: Setup of compression-compression testing on a smart tube. A fixture was machined to ensure safety and transfer force to the smart tube. Voltage response obtained by connecting the electrodes to a DAQ system.

shown in Figure 4.24. The average sensitivities lowered in comparison to the smart cylinder. These sensitivities are 46.1 mV/kN, 10.10 mV/kN and 6.36 mV/kN for 1 Hz, 10 Hz, and 15 Hz. The trend is similar as previously tested. For the effective piezoelectric coefficient, these values are 0.03 pC/N, 0.0068 pC/N and 0.0043 pC/N. These results can be explained by:

- Force transfer for this sensor design.
- Unexpected clearances during the assembly of the ”smart tube”. Any imperfection that lowers perfect contact between the electrodes and the piezoelectric ceramic results in a reduced signal sensibility.

Finally, the ”smart cylinders” fabricated using Laser Selective Melting (SLM) were tested in similar conditions. The material used in this fabrication was inconel which has almost double stiffness than Ti-6Al-4V. It is distinguishable heavier, but the misalignment

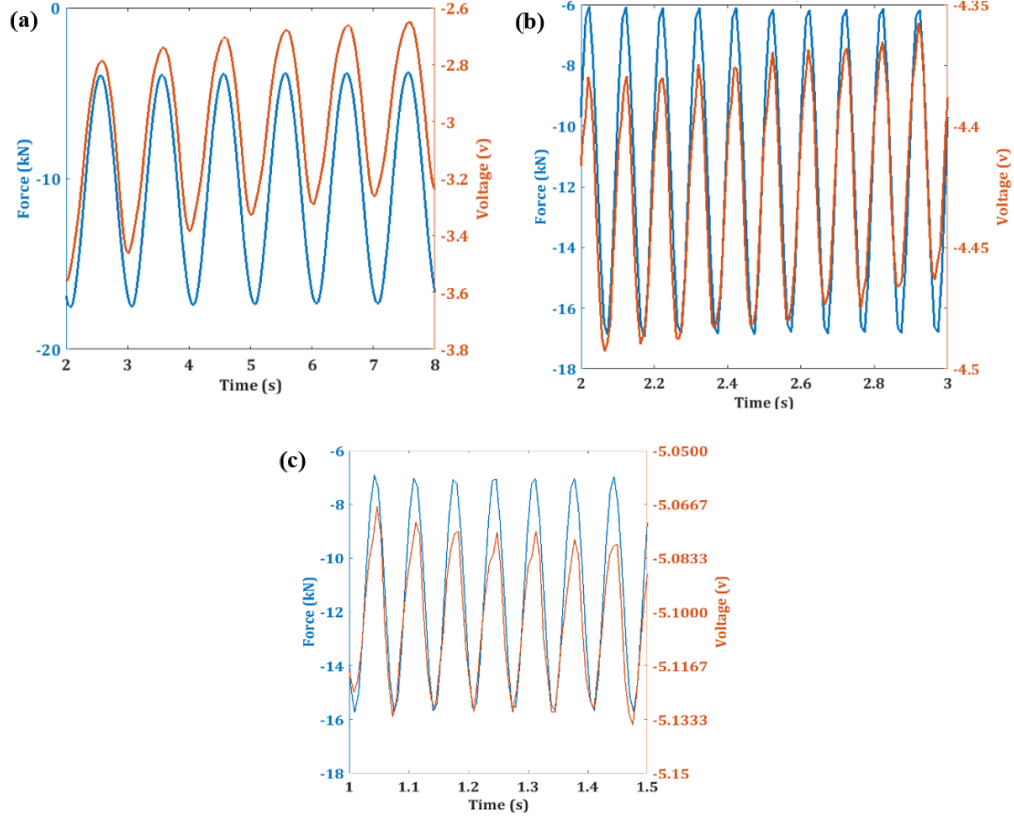


Figure 4.24: Compression-compression testing results. Each graph shows the force in kN (blue) and voltage in volts (red). Three different frequencies tested: 1 Hz (a), 10 Hz (b), and 15 Hz (c).

and lower fabrication temperatures allow the piezoelectric to survive without metallization risks. Four cylinders were simultaneously fabricated with misalignment less than 500 μm . The effective piezoelectric constant for this design and material reaches a maximum of 33.77 fC/N. These results are 1% from the achievable piezoelectric effectiveness under rough contact conditions using FEA software. The following section analyzes the performance with simulation aid for the smart structure piezoelectric effective constants.

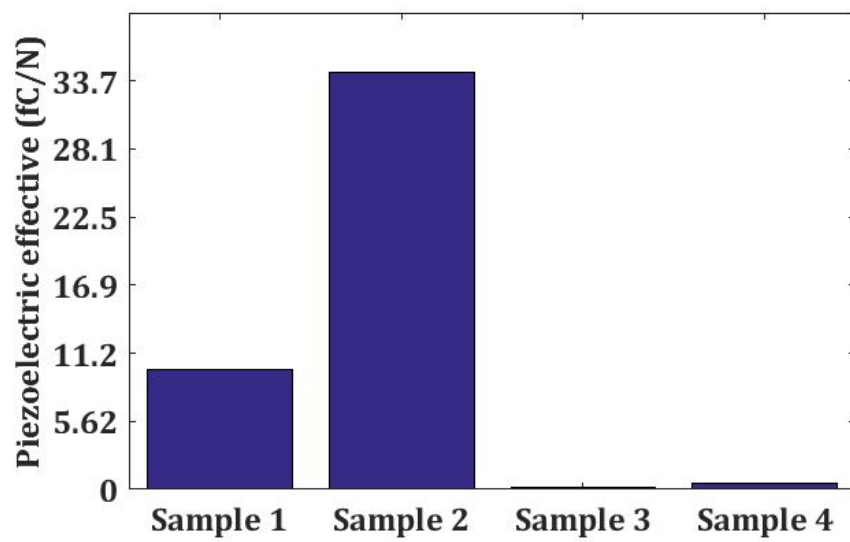


Figure 4.25: Piezoelectric effective on SLM fabricated smart cylinders.

4.2.4 Pyroelectric temperature sensing procedures

To study a temperature variation, the smart tube was exposed to heated air flowing through the tube at different temperatures. A Keithley 6485 picoammeter (Tektronix) connected to the exposed electrodes of the smart tube measured the generated current. In general, the experiment was done in two stages: heating for 6 minutes and cooling for 12 minutes. The variation of the temperature was obtained by extending the travel of the hot air. This was done by changing the length of the tube from 7.6 cm, 15.2, cm and 30.5 cm. The schematic and experimental setup is shown in Figure 4.26 and Figure 4.27.

For our samples, the contact area of the PZT is expected to be less than 39 mm^2 . The pyroelectric coefficient reported from the company [60] was $400 \text{ } \mu\text{C}/(\text{m}^2 \text{ } ^\circ\text{C})$, although in literature there are reports of $600 \text{ } \mu\text{C}/(\text{m}^2 \text{ } ^\circ\text{C})$. The choice of contact area and pyroelectric coefficient must be calibrated for the calculation of temperature. Repoling of the piezoelectric ceramic and complete contact on the surface of the piezoelectric ceramic is not completely verifiable without invading the component.

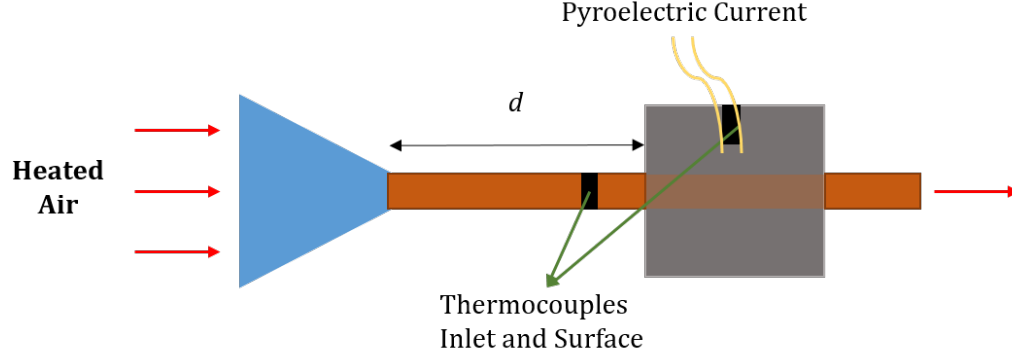


Figure 4.26: Schematic of temperature variation experiment on smart tube. Parameter d was changed to vary the temperature across the smart tube.

In Figure 4.28a, the temperature at the entrance varies accordingly to the extension used in the experiment. Maximum temperatures during the heating stage, after six minutes, are $198 \text{ } ^\circ\text{C}$, $178 \text{ } ^\circ\text{C}$, and $150 \text{ } ^\circ\text{C}$ for 7.6 cm, 15.2 cm and 30.5 cm, respectively. A corresponding variation occurs in the current generation with maximum values of 0.281 pA , 0.237 pA , and



Figure 4.27: Pyroelectric setup testing. Two thermocouples were attached to the inlet, and on the surface in the angular location of the piezoelectric ceramic. A picoammeter was attached to the electrodes to record the generated current.

0.204 pA (Figure 4.28b), respectively. A verification of the current generated is compared

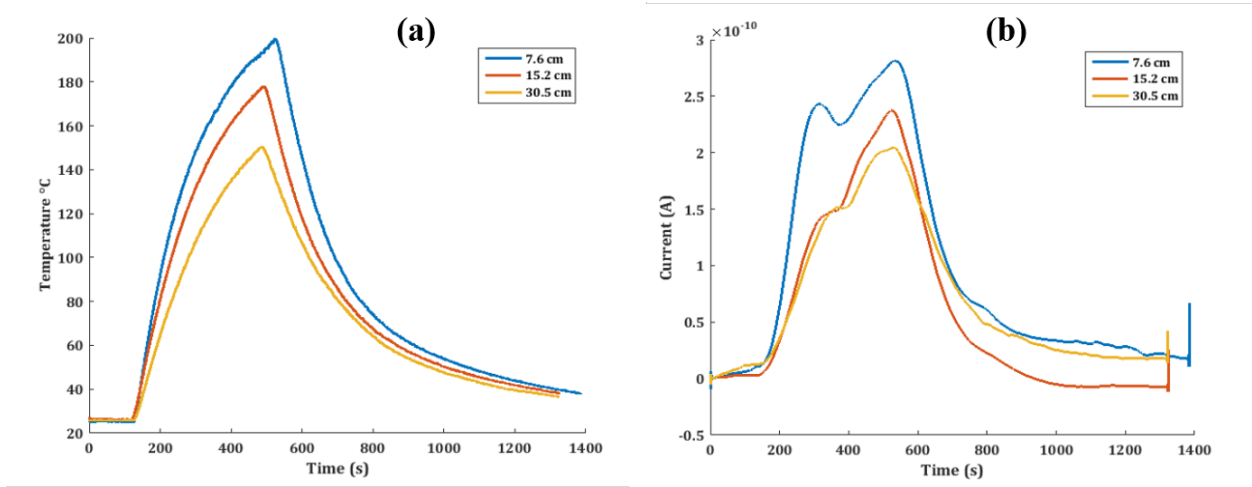


Figure 4.28: Temperature variation (a) occurred at the inlet of the tube. Different lengths increase the heat loss and produces a variation in temperature within the smart tube. A corresponding generated current (b) is recorded using a picoammeter.

using Eq. 3.11, where the generated current is proportional to the dT/dt of the correspondent thermocouple. In this case, the thermocouple cannot be placed in close proximity to the piezoelectric ceramic. Therefore, the thermocouple that is used for future comparisons is the one located on the surface of the smart tube, which is at the same angular position as the

piezoelectric ceramic embed in the smart tube. By processing the surface temperature at this location, a differentiation and comparison are shown in Figure 4.29 for the three cases (7.6 cm, 15.2 cm, and 30.5 cm).

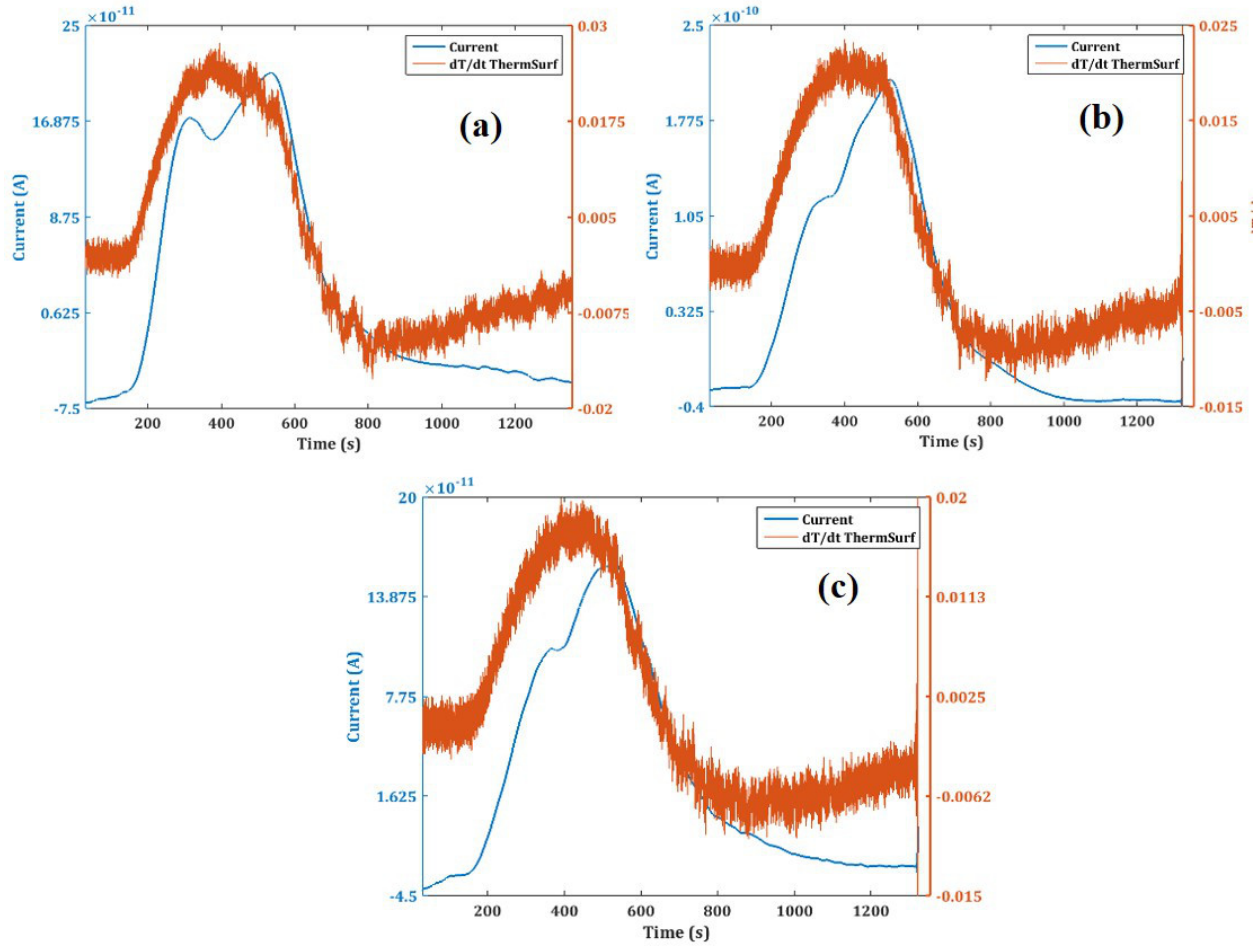


Figure 4.29: Comparison between current generated and dT/dt on the thermocouple located on the surface of the smart tube. Three cases studied: 7.6 cm (a), 15.2 cm (b) and 30.5 cm (c).

The comparisons presented in Figure 4.29, show a shoulder in the current signal at 350 seconds. This change in current (bump) does not occur in the dT/dt of the surface thermocouple. This behavior was observed during the verification of the response by repeating the experiments under same conditions. This change can be explained due to a coexistence of different phases of the PZT that cause sudden slight variations of its piezo-

electric and the pyroelectric coefficients. Sabat et al. showed that a change in piezoelectric coefficients occurred between 125-150 °C. Research has shown that although not clearly defined yet, tetragonal, rhombohedral, and monoclinic symmetries have been proven to exist in the ferroelectric phase of PZT at different temperature regimes [63], resulting in changes in piezoelectric constants for the PZT.

The generated current was integrated and adjusted according to Eq. 3.12. Using a calibrated coefficient for PA, Eq. 3.12 gives us a sensing behavior for temperature using a piezoelectric component. The estimated coefficient PA was 750 pC/(m² °C). This value shows that the theoretical contact area and pyroelectric coefficient is lower than actually intended. The value was expected since the contact area was not completely achieved during assembly of the sensor. Human error during assemblage affects mainly this parameter.

Figure 4.30a shows the temperature calculated using Eq. 3.12. Figure 4.30b shows a comparison coming from the surface thermocouple located in the same angular position as the cavity where the piezoelectric is located. The variation occurred in the current generation, results in a changing calculated temperature. Although the driving heat load during the heating stage is larger compared to the heat loss during the cooling stage, the current changes polarity (numerical sign changes from positive to negative), allowing to transform this current in a temperature sensing instrument.

4.2.5 Capacitance and Impedance analysis

An alternative method of sensing temperature is the dielectric variation with temperature of piezoelectric materials up to the Curie temperature, where the material becomes paraelectric. For this test, the LCR meter was connected to the terminals of the smart parts. Samples fabricated with EBM, showed a decrease of dielectric constant when tested under temperature variation. Figure 4.32 shows the dielectric constant calculated from the smart cylinder. These results were similar for all the samples fabricated with the EBM procedures.

The decrease on dielectric constant is explained by the partial formation on the surfaces of the piezoelectric ceramics. Oxidation at such high temperatures cannot be fully stopped. A capacitance in series reduces the overall capacitance of the structure. These results confirmed formation of lead oxide (see Figure 4.33). In contrast, the low temperature fabrication of

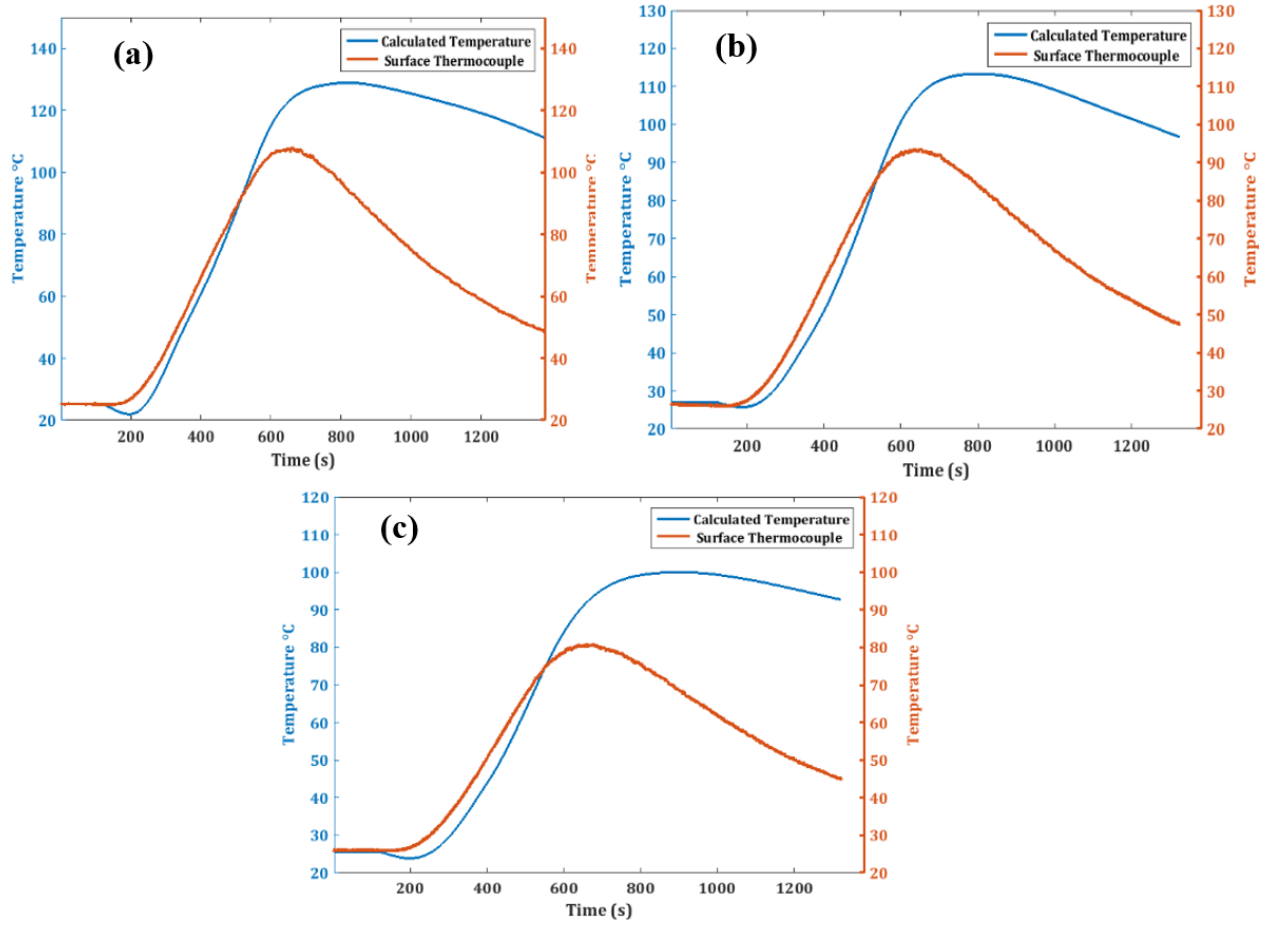


Figure 4.30: Temperature comparison between the one calculated using the generated current (a), and the thermocouple located on the surface of the smart tube.

the SLM, and the inert atmosphere during the procedure, does not alter the composition of the piezoelectric ceramic on the surfaces. These smart cylinders (from SLM), compared to EMB counterparts, are suitable for temperature sensing using the dielectric permittivity as well as the pyroelectric principle.

The experiment consisted in subjecting the cylinder to temperature variation using a hot plate set at 150 °C. A thermocouple was attached to the top surface of the cylinder, and LCR meter connected to the electrodes. Figure 4.34 shows the dielectric permittivity in comparison with the change of thermocouple reading.

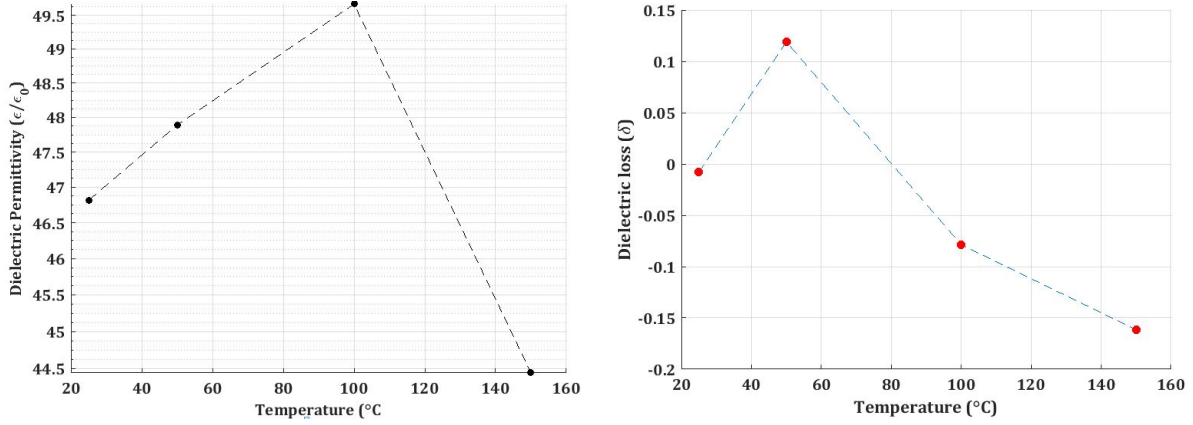


Figure 4.31: Smart cylinder dielectric constant and loss with respect to temperature after EBM fabrication.

Value	Sample	Method of Measurement	Temperature (°K)
25.9	PbO	at 10^8 cps	298
25.9	PbO	Calc. from ion polarizability (117.8 Å)	298
	<u>Pressed powder discs</u>		
35	yellow PbO sintered at 700°C	100 c to 10 kc	300
15	Pb ₂ O ₃	100 c to 10 kc	300
20	Pb ₃ O ₄	100 c to 10 kc	300
32	red PbO	100 c to 10 kc	300

Figure 4.32: Dielectric constant of lead oxides. Handbook of Physics and Chemistry.

4.3 Performance Analysis

FEA software helped to understand the performance of the fabricated smart structures. By changing the design, the simulation can provide effective limits for pressure range that the structure can operate in real applications. Ideally, the perfect contact on the assembly is not achieved, and unexpected conditions can lower the piezoelectric response of the whole structure.

The analysis includes:

1. **Modeling of smart cylinder:** Frictionless and rough contact between the surfaces.

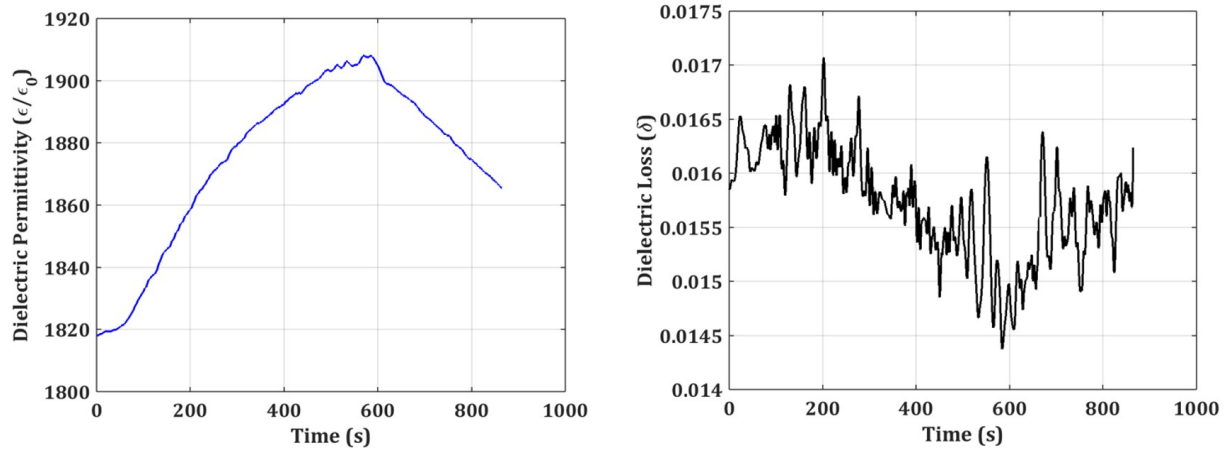


Figure 4.33: Smart cylinder temperature sensor using dielectric constant and loss after SLM fabrication.

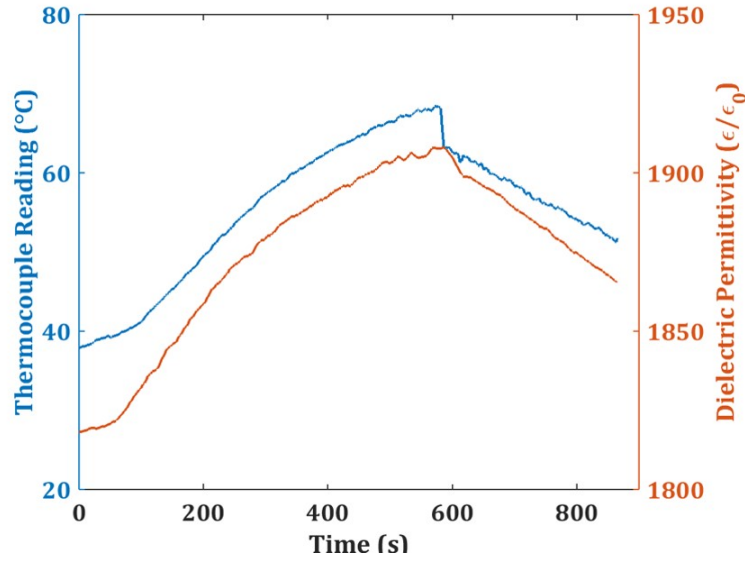


Figure 4.34: Temperature sensing using SLM smart cylinders using the dielectric constant of the piezoelectric ceramic.

Frictionless provides the ideal case of fabrication. Rough approximates the conditions of the wall of the alumina housing.

2. **Modeling of smart tube:** Similarly the smart tube and the testing conditions, are different from the cylinder. Voltage response and the effective piezoelectric coefficient

are determined.

3. **Modeling of defects:** Defects on the quality of the fabrication were observed during assembly. These defects affect the force transfer, and therefore the voltage response of the piezoelectric ceramic.

4.3.1 Smart cylinder and smart tube modeling

The cylinder was modeled following the schematic from Figure 4.35. The commercial software ABAQUS 6.14 model the electrical response of a piezoelectric to be

$$q_i = e_{ijk}^{\phi} \epsilon_{jk} + D_{ij}^{\phi(e)} E_j \quad (4.1)$$

where q_i is the charge flux vector, ϕ is the electrical potential, ϵ_{ijk}^{ϕ} is the piezoelectric stress coupling, ϵ_{ijk} is the small-strain component, $D_{ij}^{\phi(e)}$ is the dielectric matrix for fully constrained material, E_j is the electric field (negative gradient of electrical potential) [64]. The metallic parts, first fabrication, insert and second fabrication, were modeled with 10-node quadratic tetrahedron (C3D10), global size 3.2 mm, properties from Ti6Al4V grade 5 annealed [65] for $\rho=4430 \text{ kg/m}^3$, and isotropic properties $E=113.8 \text{ GPa}$, $\nu=0.342$. Ceramic housing, male and female parts, were modeled using C3D10, global size 1 mm, properties from alumina (Al_2O_3), $\rho=3000 \text{ kg/m}^3$, and isotropic properties $E=300 \text{ GPa}$, $\nu=0.21$ [65, 66]. Electrodes, top and bottom, were modeled using a 20-node quadratic brick. reduced integration (C3D20R), global size 1.2 mm, properties from tungsten, $\rho=19270 \text{ kg/m}^3$, and isotropic properties $E=400 \text{ GPa}$, $\nu=0.28$ [65]. The piezoelectric component, modeled using a 20-node quadratic piezoelectric brick, reduced integration (C3D20RE), global size 0.8 mm, using the following

properties, $\rho=7800 \text{ kg/m}^3$, the compliance matrix:

$$S_E = \begin{bmatrix} 16.4 & -5.74 & -7.22 & 0 & 0 & 0 \\ -5.74 & 16.4 & -7.22 & 0 & 0 & 0 \\ -7.22 & -7.22 & 18.8 & 0 & 0 & 0 \\ 0 & 0 & 0 & 47.5 & 0 & 0 \\ 0 & 0 & 0 & 0 & 47.5 & 0 \\ 0 & 0 & 0 & 0 & 0 & 44.3 \end{bmatrix} 10^{-12} \frac{m^2}{N} \quad (4.2)$$

piezoelectric coupling:

$$d = \begin{bmatrix} 0 & 0 & 0 & 0 & 584 & 0 \\ 0 & 0 & 0 & 584 & 0 & 0 \\ -190 & -190 & 390 & 0 & 0 & 0 \end{bmatrix} 10^{-12} \frac{C}{N} \quad (4.3)$$

and relative permittivity:

$$\epsilon_T = \begin{bmatrix} 1730 & 0 & 0 \\ 0 & 1730 & 0 \\ 0 & 0 & 1700 \end{bmatrix} \cdot 8.854 \cdot 10^{-12} \frac{F}{m} \quad (4.4)$$

The analysis consisted of a general piezoelectric step, assembling the parts with frictionless contact. A preload and a sinusoidal load of an amplitude of 1 Hz were used for comparison purposes with experimental results. The magnitude of the forces was taken from the experimental measurements of force (see Figure 4.35).

The deformation through the cylinder cross sectional area is continuous through the components of the assembly. Contours of displacement and stress of the cylinder fabricated in EBM are shown in Figure 4.36 and Figure 4.37. Similarly, SLM cylinders of Inconel are shown in Figure 4.38 and Figure 4.39.

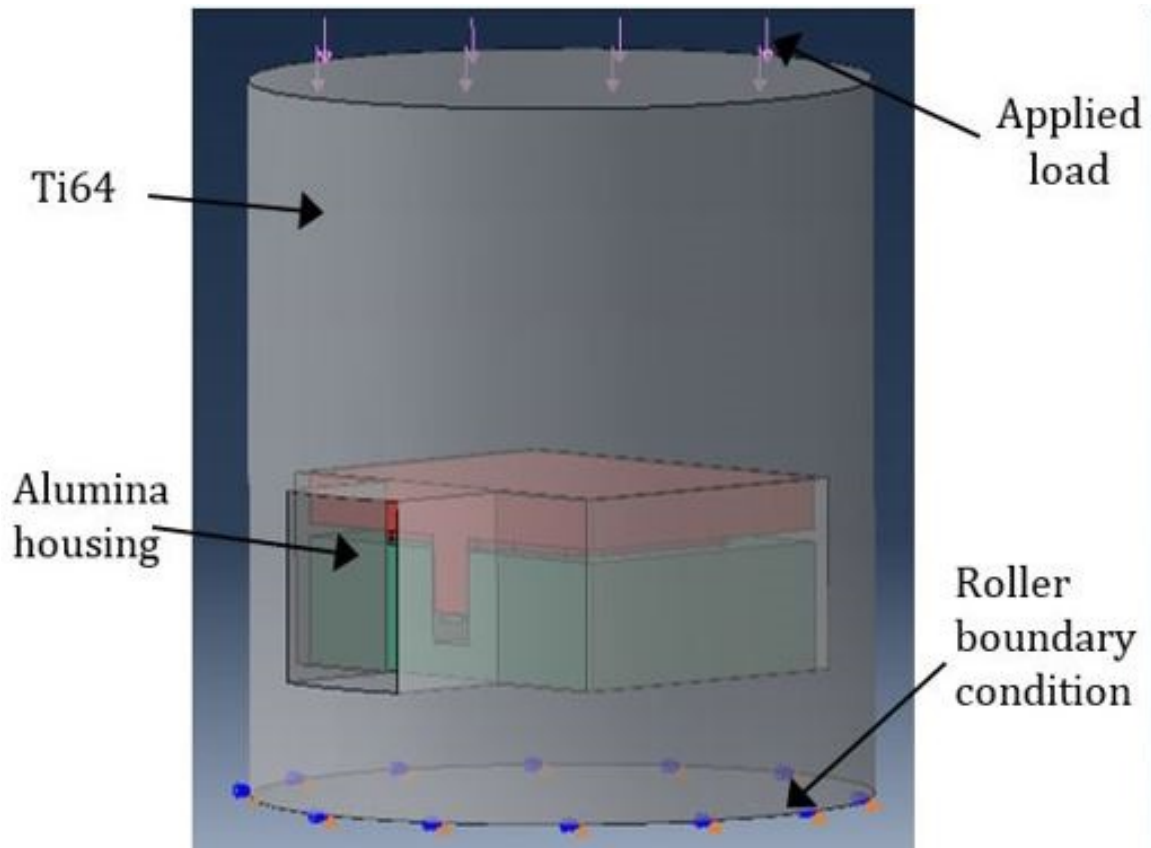


Figure 4.35: Schematic of cylinder modeling in ABAQUS for piezoelectric simulation response under different frequencies of sinusoidal loading. Alumina housing protects piezoelectric material (PZT-5A) and tungsten electrodes. Cylinder modeling simulation. Displacement contours. Generic across different contact conditions.

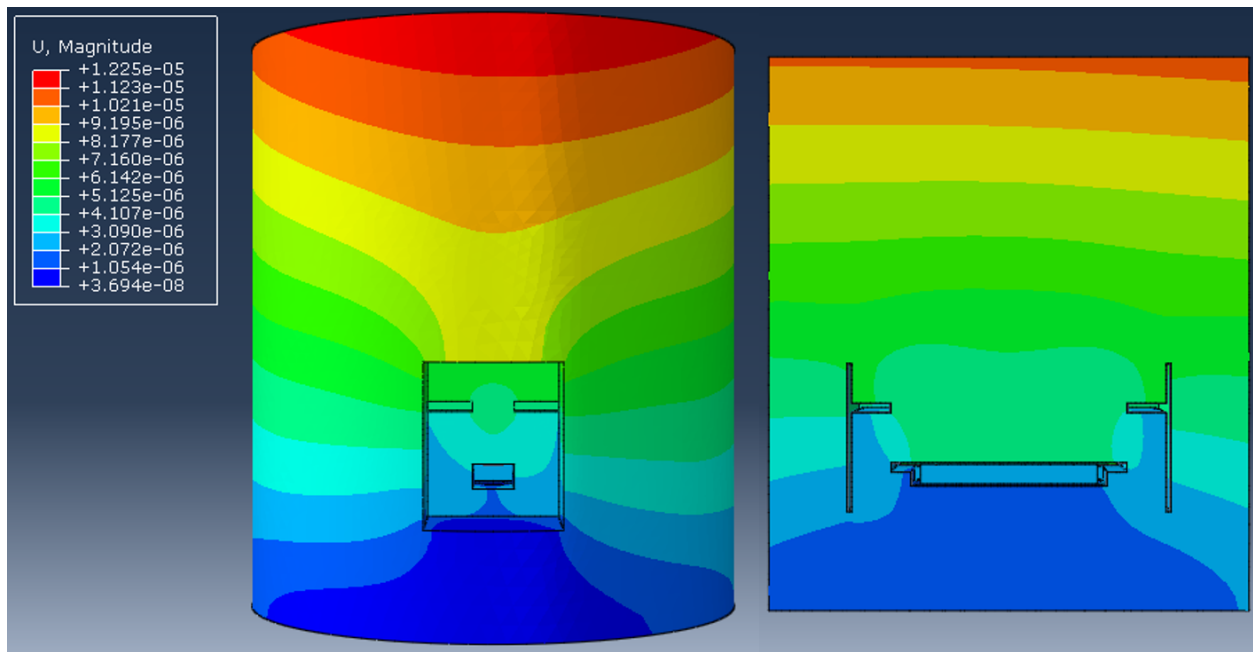


Figure 4.36: Displacement contours of cylinder modeling under compression in ABAQUS. Fabrication method: Electron Beam Melting. Metallic base of Ti-6Al-4V.

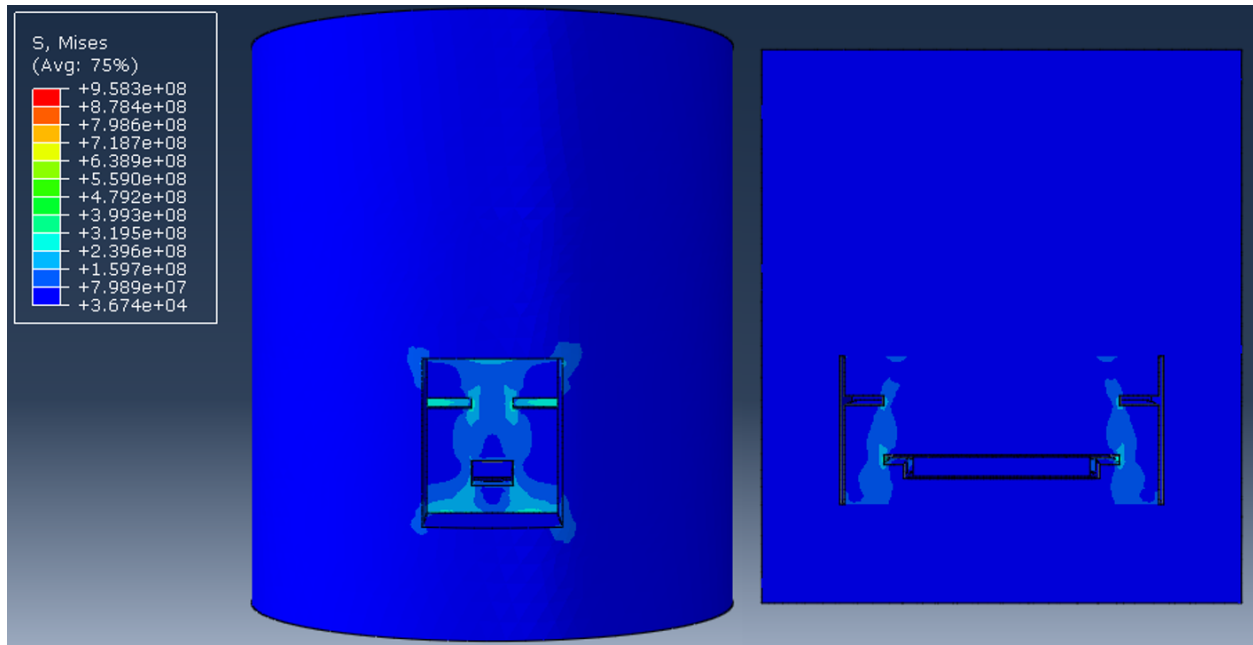


Figure 4.37: Stress contours of cylinder modeling under compression in ABAQUS. Fabrication method: Electron Beam Melting. Metallic base of Ti-6Al-4V.

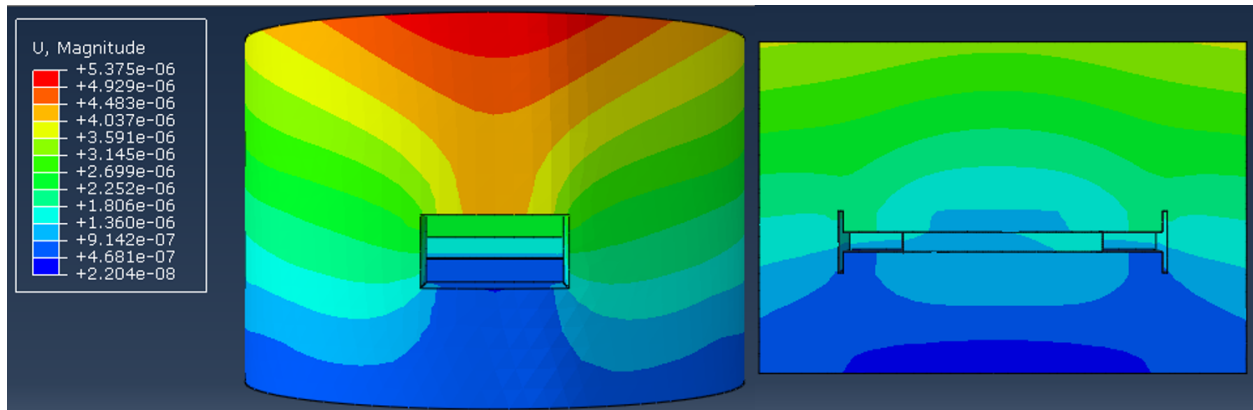


Figure 4.38: Displacement contours of cylinder modeling under compression in ABAQUS. Fabrication method: Selective Beam Melting. Metallic base of Inconel.

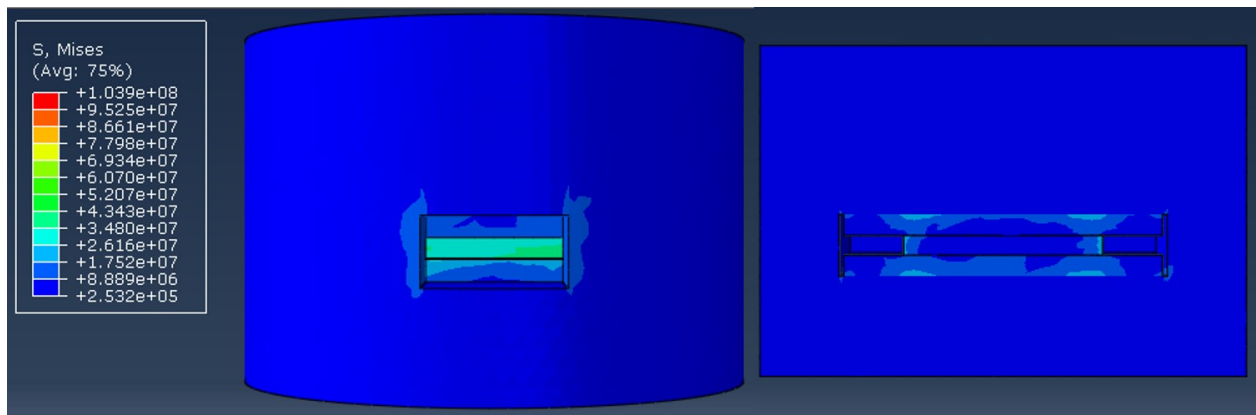


Figure 4.39: Stress contours of cylinder modeling under compression in ABAQUS.
Fabrication method: Selective Beam Melting. Metallic base of Inconel.

The simulation of the smart tube was also done under similar experimental conditions. The setup and deformation is shown in Figure 4.40. The effective piezoelectric for the test tube was 0.049 pC/N. This result exceed by 64%. Displacement and stress contours of the test tube simulation are shown in Figure 4.3.1 and Figure 4.42.

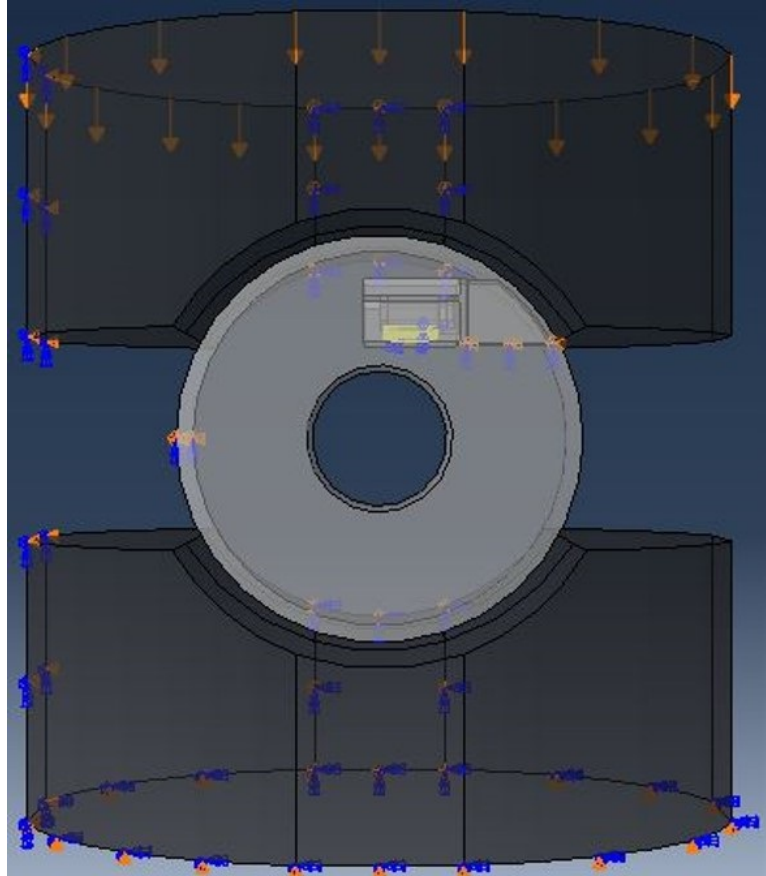


Figure 4.40: Schematic of test modeling in ABAQUS for piezoelectric simulation response under single displacement.

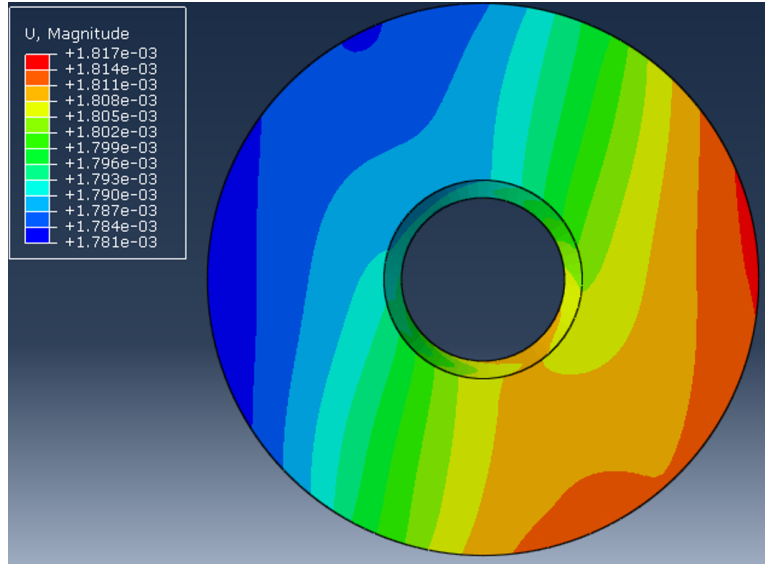


Figure 4.41: Displacement contours of tube modeling under compression in ABAQUS. Fabrication method: Selective Laser Melting. Metallic base of Inconel.

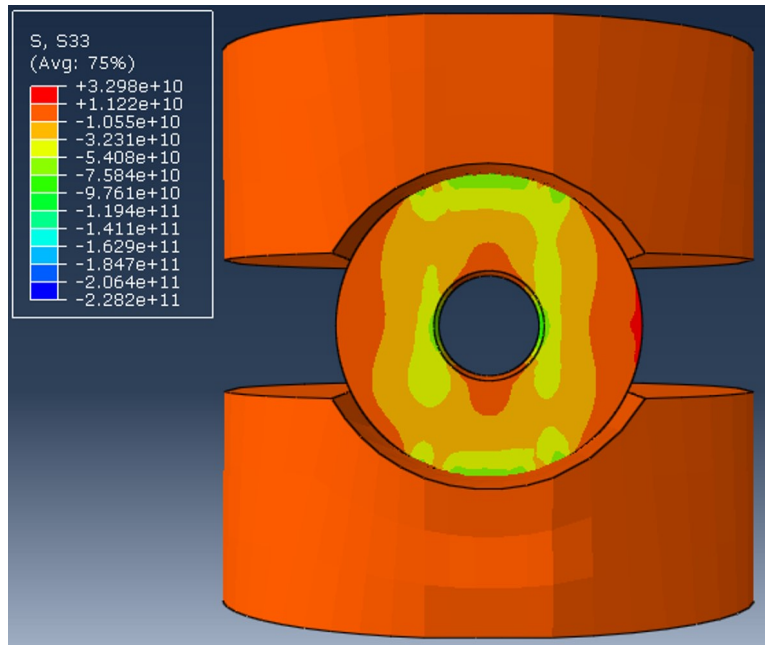


Figure 4.42: Stress contours of tube modeling under compression in ABAQUS. Fabrication method: Selective Laser Melting. Metallic base of Inconel.

4.3.2 Apparent piezoelectric constant

An analytical approximation using stiffness analysis [67], were used to estimate and validate the response with the simulation results. To understand the performance of the fabricated sensor, factors such as force transfer and effective d_{33} are considered. The model springs (see figure 4.43) have stiffness AE/L . A simplification of equivalent stiffness and overall deformation is traced back to find the acting force and deformation of each region of the model.

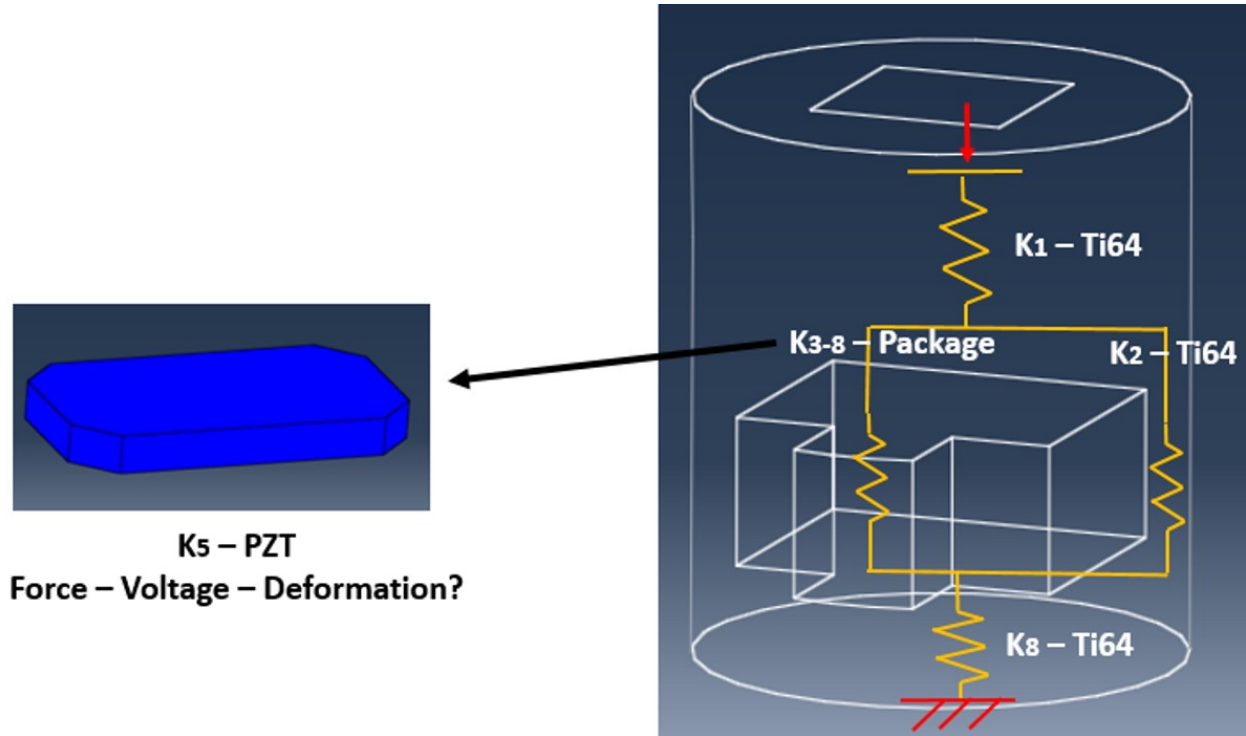


Figure 4.43: Approximation of cylinder piezoelectric constant.

The overall stiffness (K_T) was calculated using the following equation:

$$K_T = [(K_{3-8}^{series} || K_2) - K_1 - K_8]^{series} \quad (4.5)$$

The overall deflection (δ_T) is calculated using a total force F_T from two to six kilonewtons:

$$F_T = K_T \delta_T \quad (4.6)$$

Similarly, a frictionless simulation of the test cylinder was done to compare a theoretical piezoelectric constant for this design. Voltage is read from the simulation results. Figure 4.3.2 shows the voltage response from the PZT in the compression simulation of the cylinder. The results are summarized in Table 4.3.

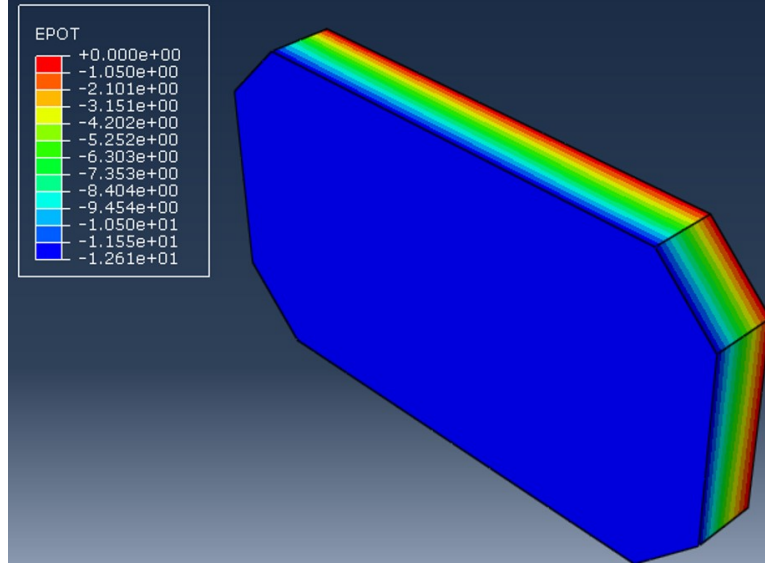


Figure 4.44: Voltage contours of PZT during compression of the cylinder in ABAQUS. Fabrication method: Electron Beam Melting. Metallic base of Ti-6Al-4V.

The piezoelectric equivalent from the theoretical approach is three times less than the reported value for the commercial PZT [60]. The results of the simulation are 13.5 times lower than the reported value. Reasons for this difference are accounted on the shell assumption of the K_2 stiffness. In reality, force is also divided by three sources: the wall interface, in particular from the friction on the vertical walls of the housing, the clearance left from imperfection during assembly and imperfections on the mating surfaces. Modifications of the analytical model and contact pressure have to be considered to approach the experimental response. Additionally, the voltage is affected by other piezoelectric coefficients, since the simulation shows that not only the stress in 3-direction acts on the material.

Table 4.3: Summary of the response on the PZT section following the model and experimental nominal properties. Force efficiency is the force transmitted to the PZT. Theoretical and simulation is presented.

<i>Approach</i>	Simulation Frictionless		Theoretical Approximation	
<i>Stress Mises (MPa)</i>	13.61	40.68	3.2	9.6
<i>Voltage (V)</i>	91.13	274.2	406.05	1218.1
<i>Force efficiency</i>	29.26%	29.15%	34%	34%
<i>Sensitivity (V/kN)</i>	45.77		203.01	
<i>d₃₃ (pC/N)</i>	26.14		115.93	

4.3.3 Consideration of defects during fabrication

The effective piezoelectric constant of the smart cylinder showed that under ideal assumptions on contact and frictionless sliding of the alumina package, exceeds the experimental effective piezoelectric. The deviations of the ideal and experimental case were justified by these sources of uncertainty:

1. Perfect contact inside the alumina package. Any deviation increases the clearance and the force needed to activate the piezoelectric material.
2. The machining of the alumina package considers a tight fit between male and female part. The friction in the mating faces divides the force that is transferred to the piezoelectric.
3. Any clearance that comes from fabrication defects. These defects include the unperfect surface of the inside face of the cavity where the sensor package rests. Unsintered powder in the corners or the faces of the bottom part creates inclined surfaces that affect the force transfer to the piezoelectric ceramic.

Friction on the faces was addressed by changing the friction in the mating surfaces. To study the influence of defects, one of the alumina surfaces was modified to have a defect of 100 μ , which is the average powder size of Ti-6Al-4V. The defects are:

1. Single slab. It models the uneven surface of the cavity.
2. Perimeter slab. It models the case where near on the corner unsintered powder creates a depression.
3. Array of slabs. It models uniform unsintered powder. This case is close to perfect contact since force is uniformly transfer to the alumina package.
4. Symmetric incline. It models the case where the alumina sanding to fit the cavity favored the center.
5. Single incline. It models the case where the alumina sanding to fit the cavity favored a side.

The defects can be seen in Figure 4.45. The simulation and the analysis of the effective

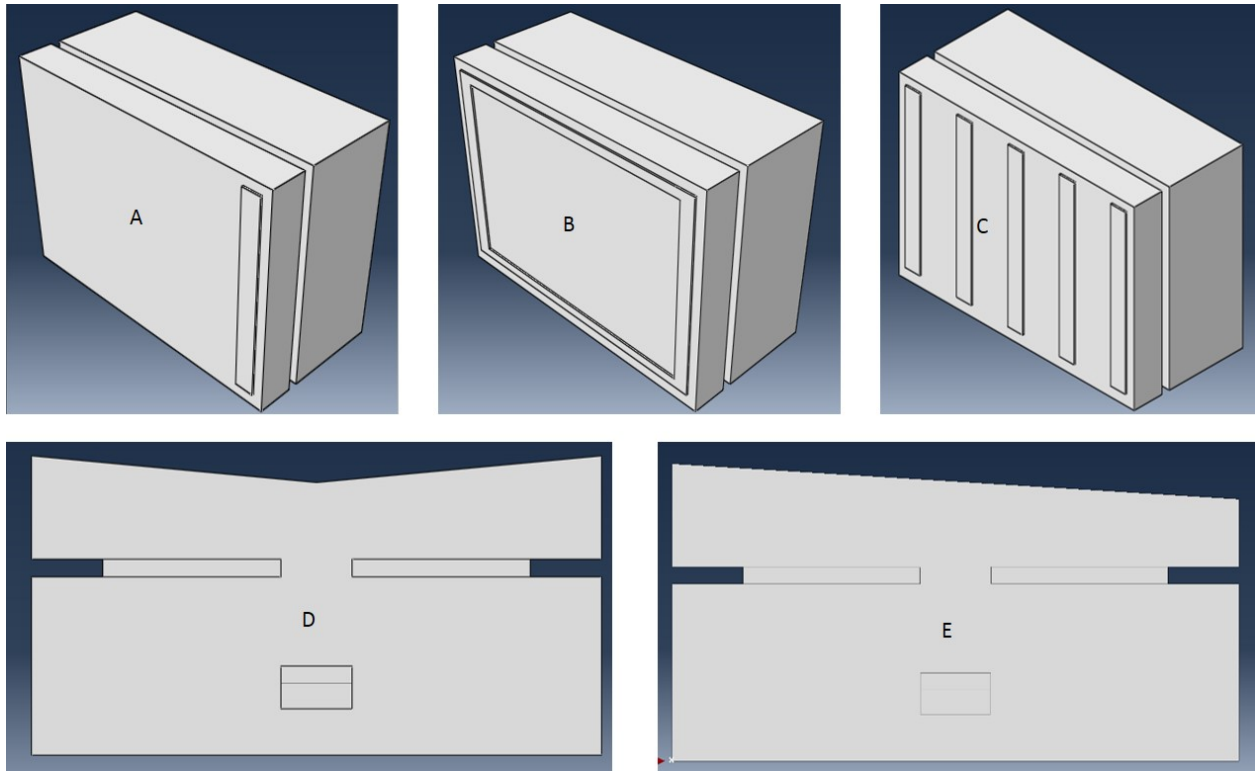


Figure 4.45: Defects modeling for the study of piezoelectric variation. A: Single slab, B: Perimeter Slab, C: Array slab, D: Symmetric incline, E: Single Side incline.

piezoelectric for the smart cylinders were calculated using Eq. 3.13. The results for the defects, no defect and experimental is compared in Figure 4.46. The figure shows that symmetric (double) incline, and perimeter slab tend to approach the no-defect condition. The experimental result falls in a zone where defects indicate they affect its response.

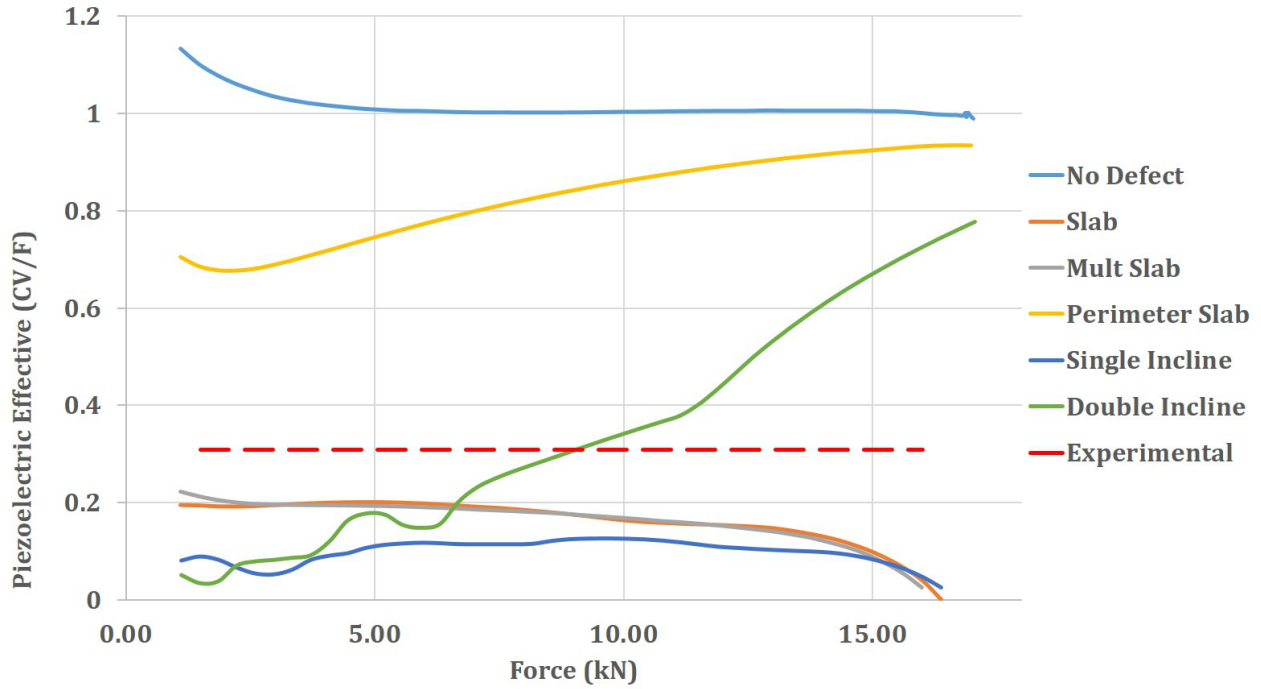


Figure 4.46: Effective piezoelectric from simulation and experiments.

Chapter 5

Plain Woven Fabric Composites with Piezoelectric Particle Enhancement

The enhancement of woven fabric composites with piezoelectric particles has been studied to achieve homogenized composites with capacity for ultimately improved sensing and structural monitoring [68, 69]. For this project, a modification of woven carbon composites was made to transform the structure in a capacitor using glass fiber and piezoelectric particles. This study adds the least amount of fiber glass to obtain a piezoelectric response from a woven carbon composite.

Carbon fabric exceeds by 2.8 times the stiffness, and by 2.2 times the strength of glass fabric composites. For this reason, the maximum mechanical strength comes from the least modification of the carbon woven composites. In the following section, fabrication and characterization are presented.

5.1 Fabrication

The fabrication process for the autoclave type vacuum bag molding commences with a complete manual hand layup. The preparation of 10"x10" squares for the size of the woven glass and carbon fibers are traced with a silver marker. During that marking process, the woven fibers are stretched out, so the intersections between threads are completely 90°, by using adequate measuring tools, the woven fibers end up with precise measurements. After the fibers are correctly marked they are hand cut by utilizing specialized scissors designed for carbon fiber fabrics. The cut samples are then visually inspected to verify that they are clear and free of any other material or objects. This is done to prevent any discrepancies during testing and data analysis, bearing us the most accurate results. Each laminate is created with nine (9) laminas (layers) with six (6) of the laminas being woven carbon fiber and three (3) woven glass fiber. Three laminas were proven to be necessary to successfully create electrical insulation between top and bottom surfaces. The total weight of these nine laminas is measured on the digital scale. The measured total weight is then utilized to find the quantity of lead Zirconate Titanate (PZT-5A). In this study, the weight percentage of

PZT was varied from zero (0) to twenty (20) in five (5) percent increments meaning 0%, 5%, 10%, 15% and 20%. The total weight is then multiplied by the percentage decided, this equals the amount of PZT that will be utilized on the composite. The PZT can be weighed as any regular powder; however, during this study, the PZT was weighed inside a glove box. The main reason for using the glove box is due to the wind and static effect upon the powder; it also prevents the inadvertent inhaling of the Lead Zirconate Titanate. As mentioned before the PZT can easily drift if exposed to air, therefore while inside the glove box and after measurement, it is mixed with the hardener then added to the resin to create the epoxy. The laminate matrix consists of epoxy system 2000 resin. This is utilized as the main component of the composite matrix; it contains medium viscosity that is lower compared to others. This light amber resin is used for fabricating high strength parts as well as demanding structural applications. It considered the highest ultimate strength epoxy for room temperature applications, recognized for the easy handle it has, and superior epoxy. It maximizes the physical properties of carbon fiber as well as glass fiber laminas. For the hardener, the size, complexity, and simplicity of the composite are taken into account, and 2020 hardener is used. This has a 20-minute curing time, and the ratio between the resin and the hardener is a four to one (4:1) by volume. This curing time must be taken into account while manually transferring/brushing the epoxy onto the laminas. The combined matrix epoxy is then stirred until thoroughly mixed, the temperature it rises to and the time must be taken into account. The mixture is then manually brushed on to each layer utilizing a regular paint brush. The complete composite is then placed between two aluminum plates to be compacted. This is then placed in a vacuum sealed bag to degas the epoxy and compress the composite. The vacuum compressing the plates forces the excess matrix to exit by all four sides, this visually ensures that the matrix has gone through the complete composite by all sides. Once the bag experiences vacuum the gage starts to indicate pressure, the sides and corners that seal the top and bottom bag must be pressured to increase and achieve 60 kPa (see Figure 5.1). After fabrication and curing time is done, the composites were marked for cutting. Figure 5.1 shows the different samples obtained for testing.

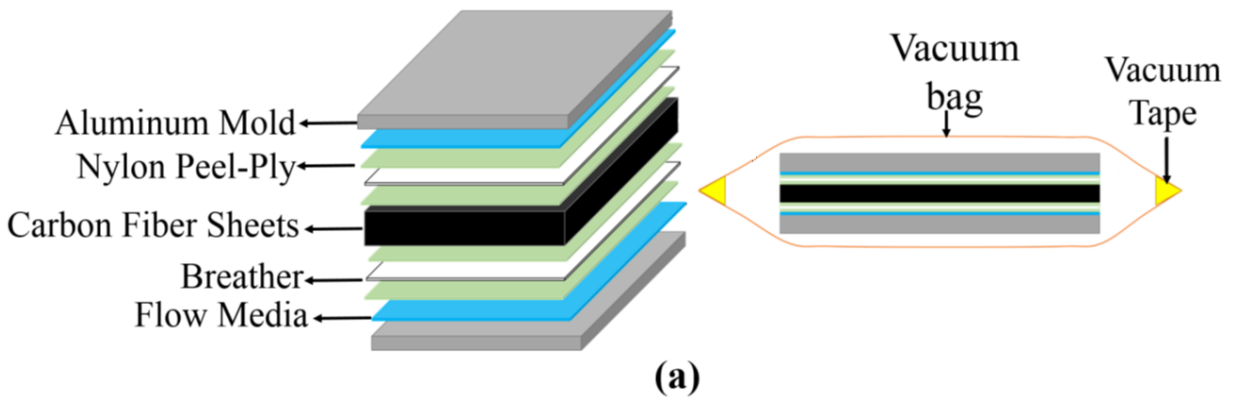


Figure 5.1: Vacuum bag fabrication composites.

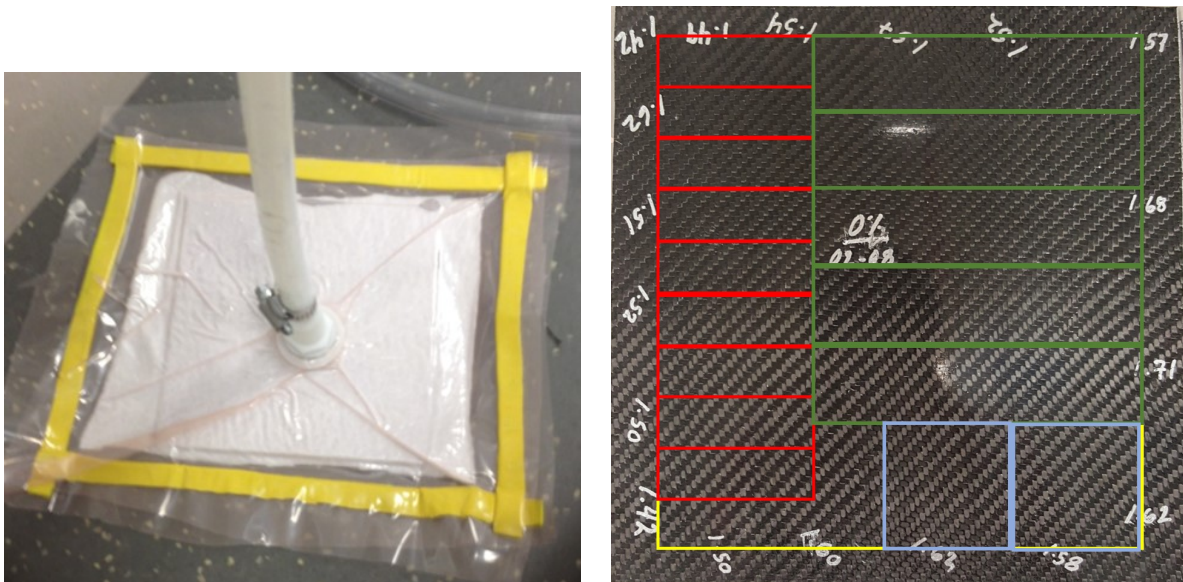


Figure 5.2: Modified autoclave fabrication of composites and cutting design.

5.2 Mechanical Characterization

The mechanical characterization includes density and volume fraction determination, dispersion analysis of the particles and flexural properties.

5.2.1 Density

The procedure was followed using the ASTM 792. The displaced volume is calculated in distilled water with known density of 0.9975 g/cm^3 . The results showed (see Figure 5.3) that the density after 0%, being the less dense, increases by the inclusions of the piezoelectric. However, a decreasing trend occurred after 10%. From empirical observations, the composites after 10% get thicker as the proportion increases. Besides, during the fabrication, the inclusion of PZT to the system decrease the working, having a catalyst effect during the curing process.

5.2.2 Volume fraction

The volume fraction was calculated following the gravimeter methodology. The results showed a decrease of fiber volume fraction as more PZT is added in the fabrication process. This is an indication of increasing voids in the final product. Figure 5.3 shows the values of the fiber volume fraction as PZT wt% is increased. It is important to distinguish the higher fiber volume fraction up to 5% which exceeds those reported from other methods of fabrication.

5.2.3 Dispersion analysis

The dispersion of the PZT was analyzed by optical method and calculation of Disperse Index outline in the methodology. As PZT is added to the composites, the surface becomes saturated. Segregation still occurs in the depressions resulted from the intersection of the warp and fill threads.

The optical dispersion can be observed in Figure 5.2.3.

The dispersion index was calculated by creating the algorithms in MATLAB. Results deviated from 1, indicate particulate segregation. As can be seen in Figure 5.2.3. The DI are **6.79**, **2.25**, **1.82**, and **1.62** for 5%, 10%, 15% and 20%. These results showed that 5%

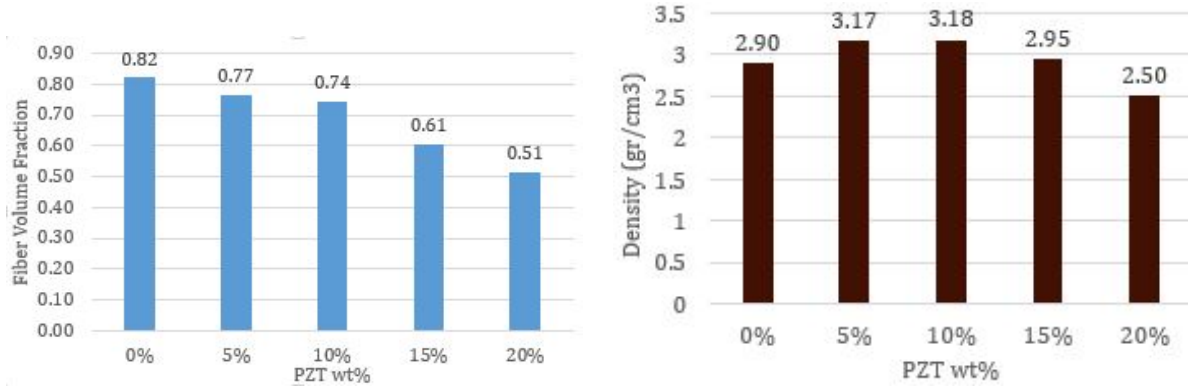


Figure 5.3: Density (left) of woven fabric composites reinforced with piezoelectric particles. Fiber volume fraction calculation using density measurements (right). Results show the average of three samples randomly selected.

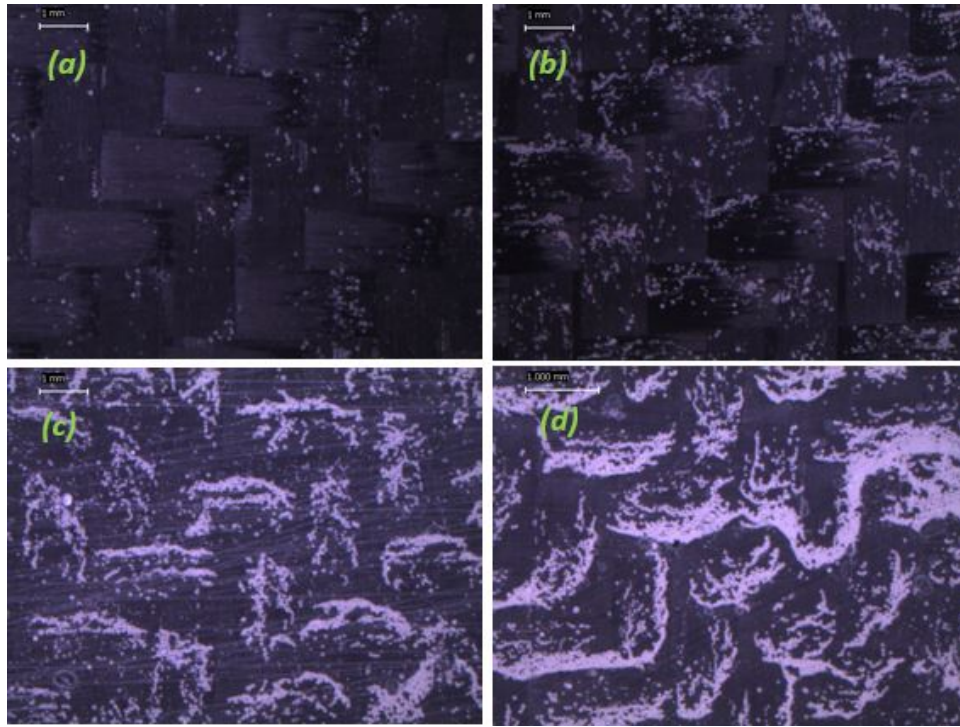


Figure 5.4: Optical images from the surfaces of woven fabric composites with PZT particle reinforcement: 5% (a), 10% (b), 15% (c) and 20% (d).

has higher separation and thus the particles tend to segregate. As concentration increases, the segregation is present, but the saturation makes the DI index approach to the unity.

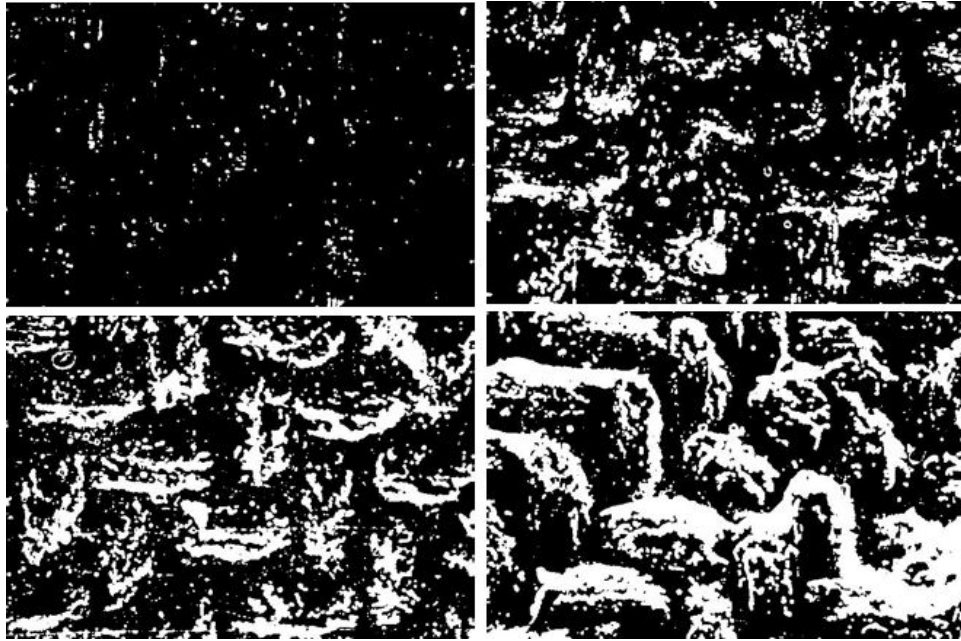


Figure 5.5: Binary images for index dispersion calculations and different concentrations of PZT: 5% (top-left), 10% (top-right), 15% (bottom-left) and 20% (bottom-right).

5.2.4 Three-point bend results

Experimental tests were design using ASTM D790-02 for flexural mechanical properties of composites (see Methodology). The flexural properties can differ with specimen depth, temperature and atmospheric conditions. The overall width of the samples was $12.49 \text{ mm} \pm 0.0233 \text{ mm}$ and the overall thickness was $2.2022 \pm 0.0205 \text{ mm}$. These deviations represent 0.1 % for the width and 0.95 % for the thickness. For every denomination, 18 experiments were done, and results were processed in MATLAB.

Samples of three-point bend experiment is shown in Figure 5.6. The maximum mechanical strength is found in the 0% of inclusions. The results showed that in the region between 10% and 15%, a decrease of mechanical properties could be observed. The Young's modulus follows the same trend and slightly increases by the 20%. Results indicate a relationship between the fiber volume fraction decrease and the mechanical properties.

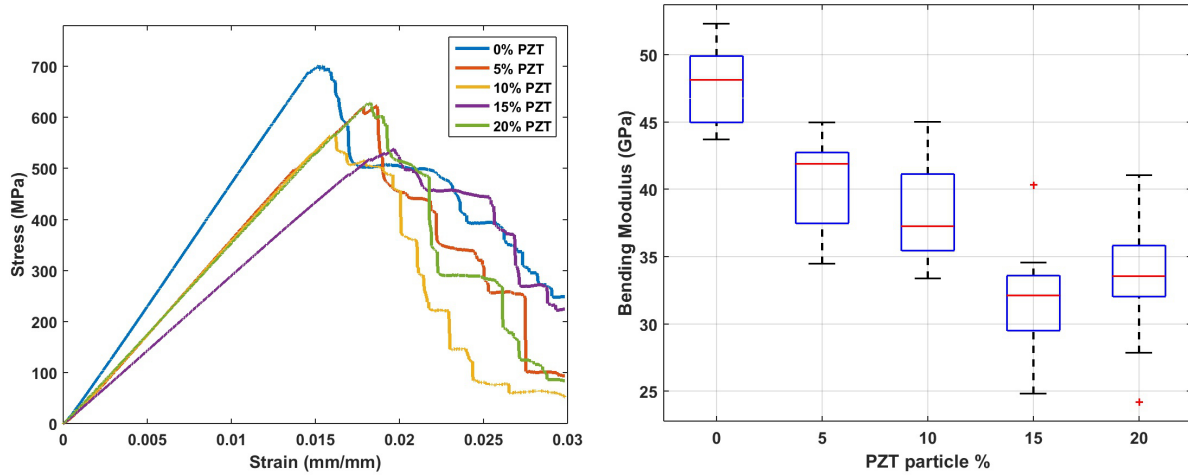


Figure 5.6: Three-point bend experiments and Young's Modulus stiffness.

Similarly, the strength and strain were calculated (see Figure 5.7. Strength has an overall decrease from 0% to 20% of 30% from 400 MPa to 250 MPa. The strain it seems to slightly improved as the PZT is added to the composite but not significantly to impact fracture toughness to first yield. Lastly, the energy absorbed by the composites is presented in Figure 5.8. The energy absorbed follows the same trend as the maximum strength. It decreases as PZT is added, and stabilizes after 10%. Crack propagation, voids, and interfacial interactions are responsible for the decrease on this property. Volume fraction and density

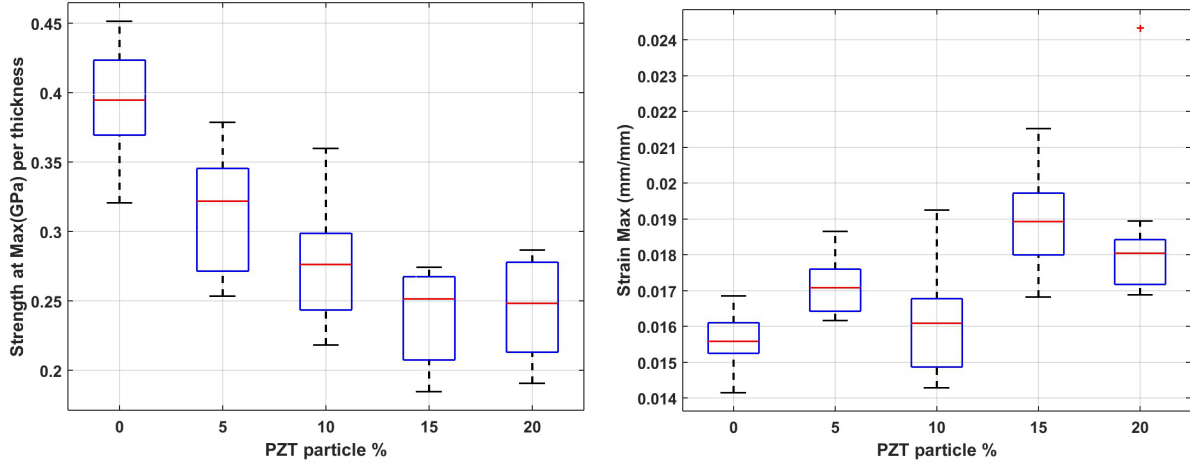


Figure 5.7: Composites maximum strength (left) and strain at this point (right).

support the behavior after 10% and the overall decrease from the fiber volume fraction.

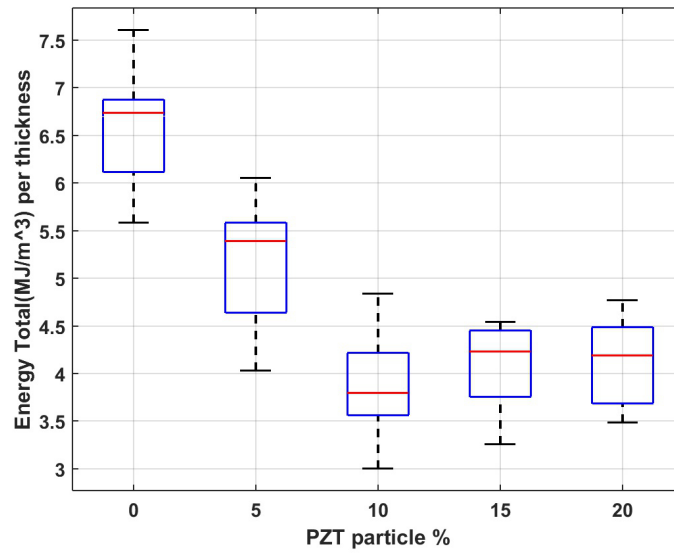


Figure 5.8: Three-point bend fracture toughness. Measured energy under the load-displacement curve.

5.3 Electrical Evaluation

Assessment of the electrical evaluation was performed in the fabricated composites. This powder has been studied by other researches in systems of PZT/matrix composites [69, 68] but not as reinforcement in the overall structure. Enhancement of piezoelectric, capacitive and impedance properties of woven carbon composites enhanced their already proven structural health monitoring applications. For this study determination of piezoelectric effective constant and charge generation using pyroelectric principle was calculated.

5.3.1 Piezoelectric analysis

For piezoelectric analysis, a compression-compression experiment (see Methodology) was performed in raw fabricated composites. Results showed that no response was generated in the range of 7-14 kN.

A poling procedure of 1.5 kV/mm for 4 hrs was needed to obtain sensing response from the composites. It is important to outline, that the PZT concentration that directly affects the piezoelectric and pyroelectric response is located at the glass fiber location. The PZT particulates are divided throughout the composites, and the actual volume fraction is ideally divided by a factor of 3.

For the compression-compression analysis, a 5 Hz loading frequency ranging from 7 kN to 14 kN was applied in different samples of poled composites. After experimentation, capacitance was calculated to obtain the effective piezoelectric coefficient. These are 0.4 fC/N, 0.47 fC/N, 0.51 fC/N and 0.58 fC/N for 5%, 10%, 15% and 20%, respectively.

5.3.2 Charge generation by pyroelectricity

To study the charge generation, the composites were subjected to heating and cooling cycles using a heat gun position at 10 cm from the larger face of the composite. The heat gun provides two settings: hot and ambient temperature. Five cycles of heating and cooling were recorded. The average charge generation per cycle was calculated by integrating the current recorded over time. The calculated charge ranged from 0.5 μC to 4.8 μC in samples of surface area of 6.45 cm^2 . The total time for cycle was 4 min. Summary of results are shown in Figure 5.9.

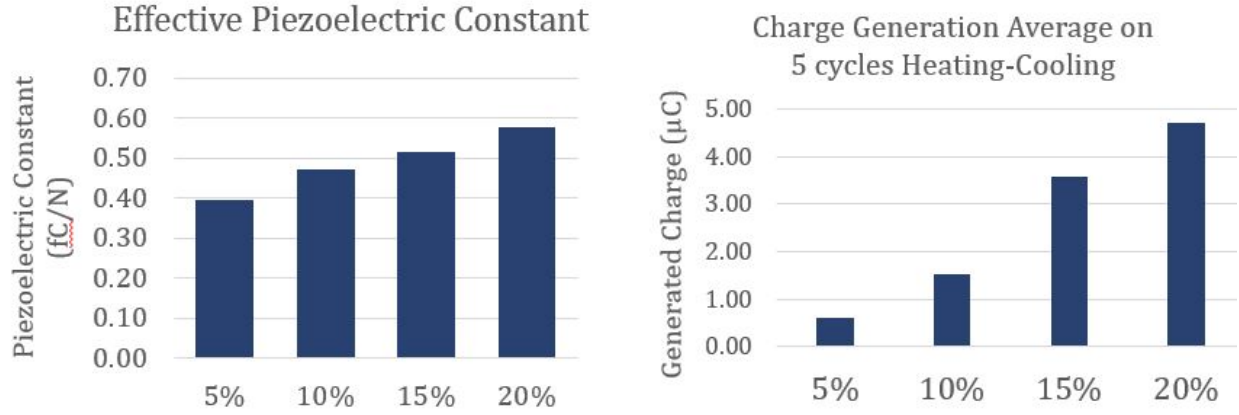


Figure 5.9: Piezoelectrical characterization of woven carbon composites with PZT particles. Piezoelectric effective constant (left) and charge generated under heating-cooling cycling (right). Two samples of each denomination randomly selected and averaged.

Improvements of the piezoelectric and pyroelectric response includes:

1. Optimization of fabrication process to decrease void fraction.
2. Poling procedures optimization under different temperature regimes.
3. Targeting of PZT particles in the glass fiber section.

Chapter 6

Conclusion and Future Work

In this work, multifunctional structures were developed by embedding piezoelectric ceramic material and using EBM and SLM fabrication processes. The method presented here enables the feasibility of fabricating energy system components with a non-intrusive sensor in a metallic body. At the same time, sensors can be placed at desired positions and inaccessible areas within part's volume. The embedded sensor can demonstrate the longevity of the sensors life. The microstructure analysis shows scopes of further improvements of the smart parts considering the interface bonding of the bottom and top part.

Two designs were implemented for the fabrication of the smart parts. A simplistic design with plate protections of the piezoelectric ceramic in the EBM lacked the protection against metal vapor and electrode shortage. Therefore, an alumina package was developed to stop the powder and vaporization of metals and ultimately protect the piezoelectric materials. This modified design was successful during the fabrication on the EBM, whereas the first design was successful for the SLM fabrication.

Effective piezoelectric coefficients for EBM fabricated cylinders were 0.3563 pC/N, 0.2858 pC/N, 0.2053 pC/N, and 0.2782 pC/N for 10 Hz, 15 Hz, 20 Hz, and 25 Hz. Similarly, the smart tube showed 0.03 pC/N, 0.0068 pC/N and 0.0043 pC/N for stress frequencies of 1 Hz, 10 Hz, and 15 Hz. Additionally, the stiffer inconel on the smart cylinders from SLM fabrication reached 0.0337 pC/N for 1 Hz.

Temperature sensing response was shown by dynamic pyroelectric effect and monitoring of dielectric constant via LabView. The test tube showed consistent results after proper calibration of the contact area for temperatures of 150°C, 178°C, and 198°C. The maximum current generation for the three scenarios was 0.281 pA, 0.237 pA, and 0.204 pA. The SLM smart cylinder was subjected to heating through a hot plate, and dielectric constant showed very good response with respect to temperature variation.

In the other hand, the simulation on ABAQUS allows the assessment and quality of the fabricated parts. The smart cylinder under ideal conditions of frictionless sliding and perfect mating contact exceeded 72 times the experimental response. It was shown that

influence of defects resulted from the fabrication and assembly process, reduces the signal to a level that is comparable to rough contact in the mating surfaces of the alumina package. Secondly, the simulation of the smart cylinder and smart tube allows the determination of the pressure range suitable for the characteristics of the geometry. The maximum pressure is restricted on the yield strength of the constituents, and the minimum pressure is restricted to the precision of the instrument.

The sensitivity response obtained from this experiment shows the feasibility of employing the smart part in practical applications. The work presented here showed that AM using EBM manufacturing can revolutionize the part's design by the embedding of sensors within part's critical areas that can be exposed to high temperature, and pressure. The method of embedding sensor presented here could be beneficial in smart parts for automotive, biomedical, aerospace industries, and other engineering aspects.

Additionally, a fabrication method of woven carbon fabric composites with piezoelectric particles was presented. The characterization of the composites showed that the PZT addition decreases steadily the fiber volume fraction. The three point bending results showed the mechanical decrease of modifying the constituents of these composites. The dispersion was analyzed optically and by measuring a scalar dispersion index (DI) which showed that as saturation increases, the segregation seems to decrease. Finally, a compression-compression testing was done in the poled composites. The responses showed maximum voltages of 1.5 V, but the effective piezoelectric coefficient ranged from 0.4 to 0.6 fC/N. These values can be improved by the targeting the capacitance area of the glass fiber. Modification of the fabrication process is needed to address the improvements of the particles. Additionally, charge generated from pyroelectric effects showed that composites can generate in average up to 0.74 $\mu\text{C}/\text{m}^2$.

6.1 Future work

Areas of future development for this the "smart parts" project involves:

1. Fabrication issues such as part's registration, and bonding strength of the interface of the "stop and go" process. Optimization is critical to minimize the weak interface resulted from the "stop-and-go" process.

2. Performance and durability of sensor under limits of oxidation and fatigue.
3. Development of software interface that allows the decoupling of the pressure and temperature combined response.
4. Use of simulation tools to derive a pyroelectric effective constant for different designs.
5. Implement wireless mechanism of the "smart structures" with embedding sensors during AM manufacturing.

Similarly, the composites can be explored by:

1. Optimize and modify fabrication method for maximum piezoelectric output without compromising structural stability.
2. Study practical applications of sensing and structural health monitoring.
3. Study elastic and fracture behavior of particulate reinforced woven fabric composites.

Bibliography

- [1] Xiaochun Li, Anastasios Golnas, and Fritz B Prinz. “Shape deposition manufacturing of smart metallic structures with embedded sensors”. In: *SPIE’s 7th Annual International Symposium on Smart Structures and Materials*. International Society for Optics and Photonics. 2000, pp. 160–171.
- [2] Asma Bakkali, Youssef Lagmich, and Abdelouahid Lyhyaoui. “Novel Autonomous Temperature Sensor based on Sensitive Material and Dielectric Resonator”. In: *International Journal of Emerging Trends & Technology in Computer Science (IJETICS)* 2.1 (2013), pp. 1–3.
- [3] Gael Sebald, Daniel Guyomar, and Amen Agbossou. “On thermoelectric and pyroelectric energy harvesting”. In: *Smart Materials and Structures* 18.12 (2009), p. 125006.
- [4] A Cuadras, M Gasulla, and Vittorio Ferrari. “Thermal energy harvesting through pyroelectricity”. In: *Sensors and Actuators A: Physical* 158.1 (2010), pp. 132–139.
- [5] Leo Christodoulou and John D Venables. “Multifunctional material systems: the first generation”. In: *JOM* 55.12 (2003), pp. 39–45.
- [6] Ronald F Gibson. “A review of recent research on mechanics of multifunctional composite materials and structures”. In: *Composite structures* 92.12 (2010), pp. 2793–2810.
- [7] Konstantinos Salonitis et al. “Multifunctional materials: engineering applications and processing challenges”. In: *The International Journal of Advanced Manufacturing Technology* 49.5 (2010), pp. 803–826. ISSN: 1433-3015. DOI: 10.1007/s00170-009-2428-6. URL: <http://dx.doi.org/10.1007/s00170-009-2428-6>.
- [8] Deborah DL Chung. “Composites get smart”. In: *Materials today* 5.1 (2002), pp. 30–35.
- [9] Edmon Chehura et al. “Strain development in curing epoxy resin and glass fibre/epoxy composites monitored by fibre Bragg grating sensors in birefringent optical fibre”. In: *Smart Materials and Structures* 14.2 (2005), p. 354.

- [10] Maurice P Whelan, Daniel Albrecht, and Antonio Capsoni. “Remote structural monitoring of the Cathedral of Como using an optical fiber Bragg sensor system”. In: *SPIE’s 9th Annual International Symposium on Smart Structures and Materials*. International Society for Optics and Photonics. 2002, pp. 242–252.
- [11] M Tietelbaum et al. *Multifunctional composites with integrated optical busses for data and sensing applications*. Tech. rep. DTIC Document, 2006.
- [12] Yonglai Yang et al. “Novel carbon nanotube-polystyrene foam composites for electromagnetic interference shielding”. In: *Nano letters* 5.11 (2005), pp. 2131–2134.
- [13] Biqin Dong and Zongjin Li. “Cement-based piezoelectric ceramic smart composites”. In: *Composites Science and Technology* 65.9 (2005), pp. 1363–1371.
- [14] Tao Yin et al. “Self-healing epoxy composites—preparation and effect of the healant consisting of microencapsulated epoxy and latent curing agent”. In: *Composites Science and Technology* 67.2 (2007), pp. 201–212.
- [15] MR Kessler, NR Sottos, and SR White. “Self-healing structural composite materials”. In: *Composites Part A: applied science and manufacturing* 34.8 (2003), pp. 743–753.
- [16] Dennis L Polla and Lorraine F Francis. “Processing and characterization of piezoelectric materials and integration into microelectromechanical systems”. In: *Annual review of materials science* 28.1 (1998), pp. 563–597.
- [17] Dip-Ing ETH Gustav Gautschi. *Piezoelectric Sensorics*. Springer, 2002, pp. 73–91.
- [18] Walter Heywang, Karl Lubitz, and Wolfram Wersing. *Piezoelectricity: evolution and future of a technology*. Vol. 114. Springer Science & Business Media, 2008.
- [19] Anderson D Prewitt. *Effects of the poling process on dielectric, piezoelectric, and ferroelectric properties of lead zirconate titanate*. 2012.
- [20] Charles L Thomas et al. “Rapid prototyping of large scale aerospace structures”. In: *Aerospace Applications Conference, 1996. Proceedings., 1996 IEEE*. Vol. 4. IEEE. 1996, pp. 219–230.

- [21] Yuhua Song et al. “Manufacture of the die of an automobile deck part based on rapid prototyping and rapid tooling technology”. In: *Journal of materials processing technology* 120.1 (2002), pp. 237–242.
- [22] J Giannatsis and V Dedoussis. “Additive fabrication technologies applied to medicine and health care: a review”. In: *The International Journal of Advanced Manufacturing Technology* 40.1-2 (2009), pp. 116–127.
- [23] *ASTM F279210 standard terminology for additive manufacturing technologies.*
- [24] Nannan Guo and Ming C Leu. “Additive manufacturing: technology, applications and research needs”. In: *Frontiers of Mechanical Engineering* 8.3 (2013), pp. 215–243.
- [25] Jean-Pierre Kruth et al. “Selective laser melting of iron-based powder”. In: *Journal of Materials Processing Technology* 149.1 (2004), pp. 616–622.
- [26] John G Webster and Halit Eren. *Measurement, Instrumentation, and Sensors Handbook: Spatial, Mechanical, Thermal, and Radiation Measurement*. Vol. 1. CRC press, 2014.
- [27] Xiao Chun Li, Fritz Prinz, and John Seim. “Thermal behavior of a metal embedded fiber Bragg grating sensor”. In: *Smart materials and structures* 10.4 (2001), p. 575.
- [28] Efrain Aguilera et al. “3D printing of electro mechanical systems”. In: *Proceedings of the Solid Freeform Fabrication Symposium*. 2013, pp. 950–961.
- [29] C Pille. “In-process-embedding of piezo sensors and RFID transponders into cast parts for autonomous manufacturing logistics”. In: *Smart systems integration* (2010), pp. 1–10.
- [30] Rahul Rai, Matthew Campbell, and Kristin Wood. “Extracting product performance by embedding sensors in SFF prototypes”. In: *Proceedings of International Solid Freeform Fabrication Symposium, Austin, Texas*. 2004.
- [31] Cesar A Terrazas et al. “Multi-material metallic structure fabrication using electron beam melting”. In: *The International Journal of Advanced Manufacturing Technology* 71.1-4 (2014), pp. 33–45.

- [32] Cesim Atas and Onur Sayman. “An overall view on impact response of woven fabric composite plates”. In: *Composite Structures* 82.3 (2008), pp. 336–345.
- [33] Zhi-Min Dang et al. “Fundamentals, processes and applications of high-permittivity polymer–matrix composites”. In: *Progress in Materials Science* 57.4 (2012), pp. 660–723.
- [34] Pal Bhaskar and Riyazuddin Haseebuddin Mohamed. “Analytical estimation of elastic properties of polypropylene fiber matrix composite by finite element analysis”. In: *Advances in Materials Physics and Chemistry* 2012 (2012).
- [35] NK Naik and PS Shembekar. “Elastic behavior of woven fabric composites: ILamina analysis”. In: *Journal of composite materials* 26.15 (1992), pp. 2196–2225.
- [36] T Ishikawa and T-W Chou. “Stiffness and strength behaviour of woven fabric composites”. In: *Journal of Materials Science* 17.11 (1982), pp. 3211–3220.
- [37] A Dasgupta, RK Agarwal, and SM Bhandarkar. “Three-dimensional modeling of woven-fabric composites for effective thermo-mechanical and thermal properties”. In: *Composites science and technology* 56.3 (1996), pp. 209–223.
- [38] T-W Chou and T Ishikawa. “One-dimensional micromechanical analysis of woven fabric composites”. In: *AIAA journal* 21.12 (1983), pp. 1714–1721.
- [39] Isaac M Daniel and Ori Ishai. *Engineering mechanics of composites*. 1994.
- [40] Jaehyon Choi and Kumar K Tamma. “Woven fabric compositespart I: Predictions of homogenized elastic properties and micromechanical damage analysis”. In: *International Journal for Numerical Methods in Engineering* 50.10 (2001), pp. 2285–2298.
- [41] Robert M Jones. *Mechanics of composite materials*. Vol. 193. Scripta Book Company Washington, DC, 1975.
- [42] James Martin Whitney and Arthur W Leissa. “Analysis of heterogeneous anisotropic plates”. In: *Journal of Applied Mechanics* 36.2 (1969), pp. 261–266.
- [43] C Soutis. “Fibre reinforced composites in aircraft construction”. In: *Progress in Aerospace Sciences* 41.2 (2005), pp. 143–151.

- [44] Nicholas S Argyres. “The impact of information technology on coordination: Evidence from the B-2 Stealth bomber”. In: *Organization Science* 10.2 (1999), pp. 162–180.
- [45] Chris Alexander and Ozden O Ochoa. “Extending onshore pipeline repair to offshore steel risers with carbon–fiber reinforced composites”. In: *Composite Structures* 92.2 (2010), pp. 499–507.
- [46] Xinlin P Qing et al. “Built-in sensor network for structural health monitoring of composite structure”. In: *Journal of Intelligent Material Systems and Structures* 18.1 (2007), pp. 39–49.
- [47] Jeong-Beom Ihn and Fu-Kuo Chang. “Pitch-catch active sensing methods in structural health monitoring for aircraft structures”. In: *Structural Health Monitoring* 7.1 (2008), pp. 5–19.
- [48] Mostafa Yourdkhani and Pascal Hubert. “Quantitative dispersion analysis of inclusions in polymer composites”. In: *ACS applied materials & interfaces* 5.1 (2012), pp. 35–41.
- [49] *Standard Test Method for Flexural Properties of Polymer Matrix Composite Materials*. Standard. 2015.
- [50] *Standard Test Methods for Density and Specific Gravity (Relative Density) of Plastics by Displacement*. Standard. 2013.
- [51] *Standard Test Method for Ignition Loss of Cured Reinforced Resins*. Standard. 2011.
- [52] Md Rashedul H Sarker et al. “Temperature measurements using a lithium niobate (LiNbO₃) pyroelectric ceramic”. In: *Measurement* 75 (2015), pp. 104–110.
- [53] Andrzej Lozinski et al. “PLZT thick films for pyroelectric sensors”. In: *Measurement Science and Technology* 8.1 (1997), p. 33.
- [54] Stanley E Woodard, Chuantong Wang, and Bryant D Taylor. “Wireless temperature sensing using temperature-sensitive dielectrics within responding electric fields of open-circuit sensors having no electrical connections”. In: *Measurement Science and Technology* 21.7 (2010), p. 075201.

- [55] Hasanul Kairm et al. “Concept and model of a metamaterial-based passive wireless temperature sensor for harsh environment applications”. In: *IEEE Sensors Journal* 15.3 (2015), pp. 1445–1452.
- [56] Warren Carl Oliver and George Mathews Pharr. “An improved technique for determining hardness and elastic modulus using load and displacement sensing indentation experiments”. In: *Journal of materials research* 7.06 (1992), pp. 1564–1583.
- [57] LE Murr et al. “Microstructures and mechanical properties of electron beam-rapid manufactured Ti–6Al–4V biomedical prototypes compared to wrought Ti–6Al–4V”. In: *Materials characterization* 60.2 (2009), pp. 96–105.
- [58] S Dadbakhsh and L Hao. “Effect of Al alloys on selective laser melting behaviour and microstructure of in situ formed particle reinforced composites”. In: *Journal of alloys and compounds* 541 (2012), pp. 328–334.
- [59] Xiaoqing Wang and Kevin Chou. “Residual stress in metal parts produced by powder-bed additive manufacturing processes”. In: *proceedings of the 26th International solid freeform fabrication symposium*, pp. 1463–1474.
- [60] *PSI-5A4E Piezoceramic, Sheets, and Plates*. URL: [http : / / piezo . com / prodsheet1sq5A.html](http://piezo.com/prodsheet1sq5A.html) (visited on 11/02/2016).
- [61] Min Ha Lee et al. “Effects of HIPping on high-cycle fatigue properties of investment cast A356 aluminum alloys”. In: *Materials Science and Engineering: A* 340.1 (2003), pp. 123–129.
- [62] *About Hot Isostatic Pressing (HIP)*. URL: <http://www.pressuretechnology.com/about-hip.php> (visited on 11/02/2016).
- [63] Ribal Georges Sabat et al. “Temperature dependence of the complete material coefficients matrix of soft and hard doped piezoelectric lead zirconate titanate ceramics”. In: *Journal of Applied Physics* 101.6 (2007), p. 064111.
- [64] ABAQUS. *ABAQUS Analysis Users Manual. Analysis Procedures, Solution, and Control. Electromagnetic analysis. Piezoelectric analysis*. 2014.
- [65] *Material Property Data*. 2014. URL: <http://www.matweb.com>.

- [66] *Rescor 960 Alumina*. 2015. URL: www.cotronics.com..
- [67] Singiresu S Rao and Yap Fook Fah. *Mechanical vibrations; 5th ed. in SI units*. Singapore: Prentice Hall, 2011.
- [68] B Satish, K Sridevi, and MS Vijaya. “Study of piezoelectric and dielectric properties of ferroelectric PZT-polymer composites prepared by hot-press technique”. In: *Journal of Physics D: Applied Physics* 35.16 (2002), p. 2048.
- [69] E Venkatragavaraj et al. “Piezoelectric properties of ferroelectric PZT-polymer composites”. In: *Journal of Physics D: Applied Physics* 34.4 (2001), p. 487.

Curriculum Vitae

Ricardo Martinez Hernandez was born on May 6, 1989. He was born in Hermosillo, Sonora, Mexico and raised in Cd. Delicias, Chihuahua, Mexico. He started college at the University of Texas at El Paso in the fall of 2007. There he began working as a mathematical tutor in the Library, eventually becoming supervisor tutor and helping in engineering fields. He graduated in the autumn 2010 as the top ten mechanical engineering students with Magna Cum Laude. He started Master's Degree as Research Assistant working on the characterization of composite materials using nanoindentation techniques under the supervision of Dr. Louyu Xu and Dr. Jack Chessa.

In fall 2013, he joined Dr. Yirong Lin's research group. Under his supervision, he obtained experience in manufacturing multifunctional materials by physical and chemical processes, experimental characterization of multifunctional materials, and design aided with FEA procedures. The research under his supervision has resulted in seven research journal papers and several presentations in conferences.

Permanent address: Calle 5ta. Sur No. 1303

Delicias Residencial, 33077

Delicias, Chihuahua, Mexico